NTNU
Norwegian University of
Science and Technology

# Vernier enhanced Mach Zehnder interferometer for dissolved methane detection

Magnus Mariero

Master of Science in Electronics
Submission date: July 2016
Supervisor: Astrid Aksnes, IET
Co-supervisor: Jens Høvik, IET
Kay Gastinger, IET

Norwegian University of Science and Technology
Department of Electronics and Telecommunications

# Problem description

The purpose of this master thesis is to determine the feasibility of a photonic sensor, capable of measuring dissolved methane gas in an aqueous environment. To prove the concept, a model of the sensor will be built and simulated in COMSOL multiphysics. The simulations are extensive and will be done in collaboration with PhD students. If a method to effectively simulate the frequency response for optical components consisting of features ranging from the nano-meter scale to centimeter-scale is developed, it would also prove useful for future master and PhD students. In addition the sensor components will be fabricated in Nanolab on an silicon-on-insulator (SOI) platform. The fabrication process requires plasma enhanced chemical vapour deposition (PECVD), electron beam lithography (EBL) and inductivley coupled plasama reactive ion etch (ICP RIE). The characterisation will be done using a scanning tunneling electron microscope S(T)EM. Extensive work on fabricating photonic components in Si has been done in previous master and project thesis. Some of this experience is used as a basis of the fabrication process. The main goal of the thesis is to determine the overall sensitivity of a sensor capable of detecting small concentrations of dissolved methane in water, couple light into fabricated Si waveguides and fabricate the individual sensor components according to specifications.

# Abstract

In this thesis the theory describing a vernier enhanced Mach Zehnder interferometer for detecting dissolved methane is discussed. A method for effectively simulating photonic components, with features ranging from centimeter to nanometer scale using COMSOL is demonstrated. The method is then used to simulate the behaviour of a vernier enhanced sensor. Based on the simulations, a methane sensitive sensor using the vernier concept is presented. The proposed sensor has a limit of detection as low as $9.34 \cdot 10^{-6}$ RIU and overall sensitivity of $326\ \mu m$/RIU, and should detect concentrations of dissolved methane less than 50 nM .

The feasibility of producing a prototype in NTNU Nanolab have also been investigated. Both straight waveguides, ring resonators and five MZI's with Y-bends has been fabricated on an silicon-on-insulator (SOI) platform. The processes used includes plasma enhanced chemical vapor deposition (PECVD), electron beam lithography (EBL), inductively coupled plasma reactive ion etch (ICP-RIE) and a scanning tunneling electron microscope (S(T)EM) for characterization. Some of the fabricated components are also tested in an optics lab. Based on characterisation using S(T)EM, the SOI platform with a thermally grown oxide layer is concluded to be the favourable choice for fabricating a prototype sensor in the future.

# Sammendrag

I denne oppgaven beskrives teorien rundt et vernier forbedret Mach Zehnder interferometer til deteksjon av oppløst metan. En metode for å effektivt simulere fotoniske komponenter, som spenner fra centimeter til nanometer skalaen, ved hjelp av COMSOL er demonstrert. Metoden er så brukt for å simulere frekvensresponsen til en vernier forbedret sensor. Basert på simuleringene blir en metan-sensitiv sensor presentert. Denne sensoren har en deteksjonsgrense så lav som $9.34 \cdot 10^{-6}$ RIU og en total sensitivitet lik $326\ \mu m$/RIU. Sensoren bør detektere metan-konsentrasjoner mindre enn 50 nM.

Det er også undersøkt om det er gjennomførbart og produsere en prototype i NTNU Nanolab. For å avgjøre dette er rette bølgeledere, ring resonatorer og fem Mach Zehnder interferometer med Y-split fabrikert på en silisium-på-insulator (SOI) platform. Prosessene som er brukt inkluderer plasma enhanced chemical vapor deposition (PECVD), electron beam lithography (EBL), inductively coupled plasma reactive ion etch (ICP-RIE) og et scanning tunneling electron microscope (S(T)EM) for karakterisering. Noen av de fabrikerte prøvene er også testet i en optikk lab. Basert på karakterisering i S(T)EM, er det konkludert med at en SOI platform med termisk oksid er det mest gunstige valget for å fabrikere en prototype i fremtiden.

# Preface

This thesis is submitted in partial fulfilment for the degree of Master of Science in Electronics at the Department of Electronics and Telecommunications at the Norwegian University of Science and Technology, NTNU. This thesis builds upon the work done in a precursory project thesis written last semester, and parts of the fundamental theory has been revised for this master thesis. The text in the thesis is entirely the work of the author.

# Acknowledgements

First and foremost I would like to thank my supervisor, professor Astrid Aksnes. Her eye for details, extensive knowledge on photonics and time management has proven invaluable during the thesis work. She has probably gone through some red pens while reading my earlier drafts, and this thoroughness is greatly appreciated. Her future students should consider themselves lucky.
I would also like to give a special thanks to my co-supervisor Jens Høvik for all his help, both with the practical lab work and sharing healthy frustration over COMSOL. His insight and experience has often saved me from banging my head against the wall too much.
My second co-supervisor Kay Gastinger has also been a great help in facilitating the work done in Nanolab. His critical thinking and experience have been very helpful, and he always has a backup solution in case something goes wrong.
A big thank you to the staff at Nanolab, who goes above and beyond to make sure everything goes as smooth as possible. And also a thank you to Tore Landsem at the tele engineering workshop at IET.
Finally I would thank my fellow students Morten Hage, Lars G. Holmen and Idunn Knain for a good final semester at NTNU and both the serious and not so serious discussions.

# Contents

# List of Figures

# List of abbreviations

| | |
|---|---|
| ΔFSR | Difference between two free spectral ranges. |
| AFM | Atomic force microscopy. |
| CTG | Cyclotriguaiacylene. |
| EBL | Electron beam lithography. |
| FEM | Finite element method. |
| FSR | Free spectral range. |
| FWHM | Full width half maximum. |
| ICP - RIE | Inductively coupled plasma reactive ion etch. |
| KOH | Potassium hydroxide. |
| LOD | Limit of detection. |
| MZI | Mach Zhender interferometer. |
| OSA | Optical spectrum analyzer. |
| PDE | Partial differential equation. |
| PDMS | Polydimethylsiloxane. |
| PECVD | Plasma enhanced chemical vapor deposition. |
| RMS | Root mean square. |
| RR | Ring resonator. |
| S(T)EM | Scanning (tunneling) electron microscope. |
| SAN | Styrene-acrylonitrile. |
| SOI | Silicon-on-Insulator. |
| TE | Transverse electric. |

TM Transverse magnetic.

# 1 Introduction

In this master thesis a photonic sensor for detecting dissolved methane gas in an aqueous environment will be presented. Photonics is a wide field which governs the use of photons in everything from sensors, communication systems and lasers. There are several advantages using a photonic sensor, some of them are the high sensitivity, selectivity and immunity from electromagnetic interference [6]. Today there is both commercial sensors utilizing the technology as well as ongoing research to improve and discover new concepts. A lot of integrated photonics are built on an silicon-on-insulator (SOI) platform, this is especially interesting as it makes it possible to integrate photonics and electronics on the same chip. It also takes advantage of the experience in fabrication and material science from the semiconductor industry. In the design presented an SOI platform is chosen as the basis for the device. The light source is an IR laser, as Si has a minimum absorption in wavelengths close to the industry standard 1550 nm [7, 8, 9].

The different sections will explain the workings of the individual components that together would theoretically be able to measure minute changes in the concentration of dissolved methane. Sensor simulations are performed using COMSOL Multiphysics®, which is a FEM software. Some additional calculations and plots are performed in MATLAB®. The electromagnetic problems are described mathematically by Maxwell's equations, which is the basis of how COMSOL solves such problems. These equations will be analyzed in the theory chapter along with coupled mode theory and the effective index method. The complete sensor is simulated and analysed. In addition the individual components of the sensor are fabricated and characterized in NTNU Nanolab. The thesis is built up in the following way:

- Background and motivation
- Theory and concept
- COMSOL analysis
- Fabrication
- Discussion, conclusion and future work

# 2 Background and Motivation

Methane ($CH_4$) is the simplest alkane, and the main component in natural gas. It exists naturally both below ground and in large reservoirs under the sea floor. The gas is primarily used as fuel for turbines, generators, different industrial processes and commercial heating. Methane also plays an important part in some of the chemical reactions occurring in the troposphere, a less fortunate role of $CH_4$ is as a potent green house gas. There are several sources to the increased methane concentration in the atmosphere, the ocean is one of these sources, but compared to the other sources in the global methane emission budget it is insignificant. This has been puzzling scientists, especially when we consider the enormous reservoirs of methane on both the continental shelf, in gas pockets and seeping out from cracks and volcanoes on the ocean floor. It is estimated that as much as 80% of the methane that sieves up does not reach the surface. Studies on the subject have been conducted since the 60's and anaerobe oxidation by microbes have been proposed as a main cause. Closer to the surface, where the water has more oxygen and increased temperature, $CH_4$ dissolves as separate molecules. Surface concentrations vary geographically, but are typically in the low nano molar range.

Other potential sources that have gained more interest recently, are methane clathrates. Methane complexes directly with water and can form clathrate hydrates at sufficient depths, temperatures and pressures. The clathrates are crystalline like solids which traps $CH_4$ molecules in a lattice formed by the host molecules [10]. These can form in different environments, but there are large concentrations in arctic waters. This have recently raised some concerns if the global temperature keeps rising. Other sources which are important to monitor are potential leakage from off-shore related activities.

At these low concentrations the need for highly sensitive measuring techniques are necessary. Optical devices and sensors have in theory the ability to detect these minute changes in concentration, and are able to do it without extensive sample preparation [10]. A sensor capable of continuously measuring these changes autonomously could be used both for environmental reasons and for monitoring petroleum production in e.g the North Sea or the Mexican Gulf.

# 3 Theory

In this section the necessary theory needed to understand the operating principle of the sensor is described.

## 3.1 Maxwell's equations

The fundamental theory describing light - matter interaction on a quantum level is quantum electrodynamics. But for many purposes we can consider light as a macroscopic field instead of consisting of single photons. When this field propagates in a medium or vacuum, an approximate description can be used, the macroscopic set of Maxwell's equations (1) - (4) [11].

$$\nabla \times \mathbf{E} = -\frac{\partial \mathbf{B}}{\partial t} \tag{1}$$

$$\nabla \times \mathbf{H} = \mathbf{J} + \frac{\partial \mathbf{D}}{\partial t} \tag{2}$$

$$\nabla \cdot \mathbf{D} = \rho \tag{3}$$

$$\nabla \cdot \mathbf{B} = 0 \tag{4}$$

The complex amplitudes in (1)-(4) are defined as; **E** is the electric field intensity, **H** the magnetic field intensity, **D** the electric displacement field and **B** is the magnetic flux density. **J** is the current density and $\rho$ is charge density. In a non dispersive isotropic media **D** has a relation to **E** according to equations (5) - (7) [11]

$$\mathbf{D} = \epsilon_0 \mathbf{E} + \mathbf{P} \tag{5}$$

$$\mathbf{P} = \epsilon_0 \chi \mathbf{E} \tag{6}$$

$$\mathbf{D} = \epsilon \mathbf{E} \tag{7}$$

Where **P** is the polarization density, $\chi$ is the susceptibility, $\epsilon$ the relative permittivity in the medium and $\epsilon_0$ the permittivity in vacuum.

## 3.2 Boundary conditions

To solve the equations some boundary conditions needs to be satisfied for the field vectors **E**, **D**, **H** and **B**. These can be derived using the integral form and assuming the equations hold for discontinuous media. The boundary conditions are shown in equations (8) - (11) [11].

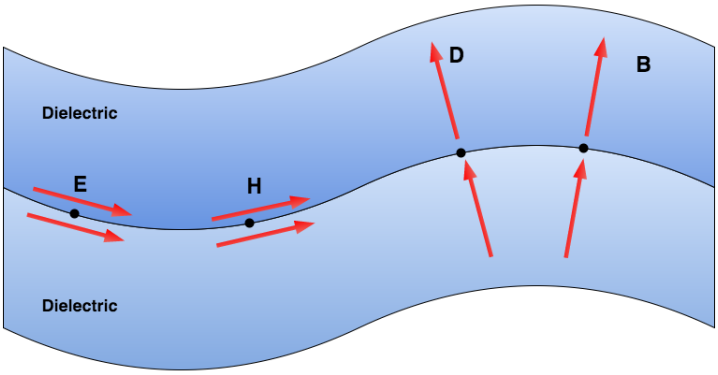


**Figure 1:** Illustration of the boundary conditions between two different media [7]

$$E_{1t} = E_{2t} \tag{8}$$
$$\hat{n}_2 \times (\mathbf{H}_1 - \mathbf{H}_2) = \mathbf{J}_s \tag{9}$$
$$\hat{n}_2 \cdot (\mathbf{D}_1 - \mathbf{D}_2) = \rho_s \tag{10}$$
$$B_{1n} = B_{2n} \tag{11}$$

### 3.2.1 Solutions to Maxwells equations

When studying the propagation of EM waves in different media, the origin of the wave is not so important, we are more interested in the propagation itself. This allows a simplification of the equations and boundary conditions by setting $J = 0$ and $\rho = 0$. If we consider time harmonic fields with only spatial dependence we can represent the fields as vector phasors. These are in general complex and on the form shown in equation (12) [11]

$$\mathbf{E}(x, y, z, t) = Re\{\mathbf{E}(x, y, z)e^{j\omega t}\} \tag{12}$$

Both these relations give Maxwell's equations in a new form, assuming we are in a non magnetic, isotropic and homogeneous medium.

$$\nabla \times \mathbf{E} = -j\omega\mu\mathbf{H} \tag{13}$$
$$\nabla \times \mathbf{H} = j\omega\epsilon\mathbf{E} \tag{14}$$
$$\nabla \cdot \mathbf{E} = 0 \tag{15}$$
$$\nabla \cdot \mathbf{H} = 0 \tag{16}$$

Where $\omega$ is frequency and $\mu$ is the relative permeability.

Through vector relations these can be combined to two second order PDE's in $\mathbf{E}$ and $\mathbf{H}$. These are the homogeneous Helmholtz's equations, (17) and (18).

$$\nabla^2\mathbf{E} + k^2\mathbf{E} = 0 \tag{17}$$
$$\nabla^2\mathbf{H} + k^2\mathbf{H} = 0 \tag{18}$$

The boundary conditions described earlier imply that the electric field is continuous at the boundary between two media. When the surrounding media is not a perfect conductor, there still exist field components outside the guide. These are called evanescent waves, which decay exponentially in the surrounding media [11, 7].

## 3.3 Coupled mode theory

The mechanism of power transfer between two spatially separated waveguides is called coupling. It can be viewed as a scattering effect, where the light in waveguide 1 scatters from waveguide 2, which then acts as a source in waveguide 2. This new field that is generated affects the field in waveguide 1. This can be described and analyzed mathematically by applying Maxwell's equations, and boundary conditions in the different regions to find the true modes for the system as a whole [7]. This analysis is complex and time consuming, but there are some approximations and assumptions that can be made to simplify the analysis.

Coupled-mode theory is based on the assumption that the coupling between waveguides is weak. Figure 2 illustrates two waveguides separated by a distance $2a$.

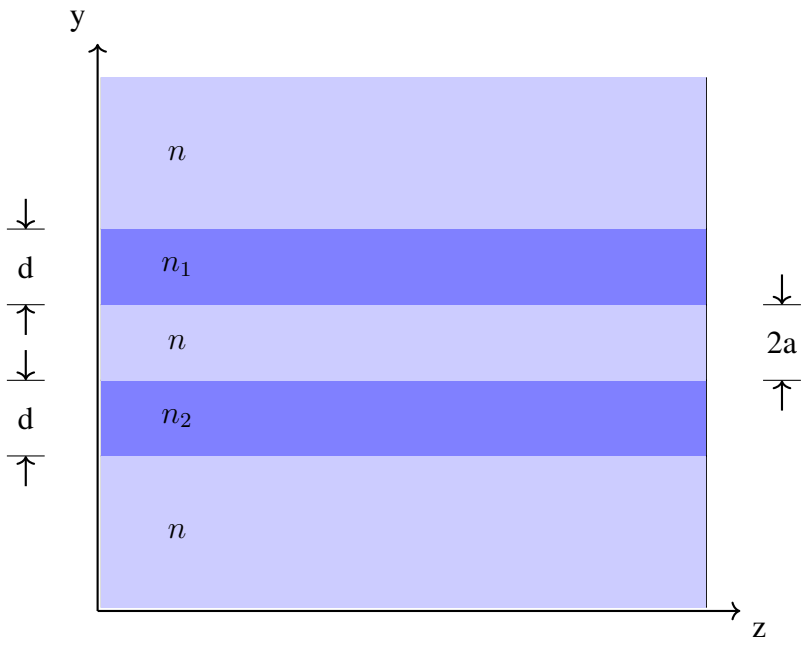


**Figure 2:** Two waveguides with thickness $d$, separated a distance $2a$ and with refractive indexes $n_1$ and $n_2$

We can express the modes in each waveguide independently in the form; $u_1 exp(-j\beta_1 z)$ and $u_2 exp(-j\beta_2 z)$. Other assumptions made are that the coupling does not alter the spatial distribution of the fields, nor its propagation constants. So the only thing the coupling modifies is the amplitude of the modes, $a(z)$ which can be assumed to vary slowly compared to $1/\beta$. We can now express the modes as $a_1 u_1(y) exp(-j\beta_1 z)$ and $a_2 u_2(y) exp(-j\beta_2 z)$. If waveguide 2 is regarded as a perturbation of the media surrounding waveguide 1, we can apply the Helmholtz equation in the presence of a source, $\mathfrak{S}_i$, that is due to an excess polarization density $P$ [7].

$$\mathfrak{S}_i = -\mu_0 \frac{\partial^2 P}{\partial t^2} \tag{19}$$

It can be shown that we end up with two coupled first order PDE's describing $a_1(z)$ and $a_2(z)$ [7].

$$\frac{da_1}{dz} = -j\mathcal{C}_{21} exp(j\Delta\beta z) a_2(z) \tag{20}$$

$$\frac{da_2}{dz} = -j\mathcal{C}_{12} exp(j\Delta\beta z) a_1(z) \tag{21}$$

where

$$\Delta\beta = \beta_1 - \beta_2 \tag{22}$$

and

$$\mathcal{C}_{21} = \frac{1}{2}(n_2^2 - n^2)\frac{k_0^2}{\beta_1}\int_a^{a+d} u_1(y)u_2(y)\,\mathrm{d}y \tag{23}$$

$$\mathcal{C}_{12} = \frac{1}{2}(n_1^2 - n^2)\frac{k_0^2}{\beta_2}\int_{-a-d}^{-a} u_2(y)u_1(y)\,\mathrm{d}y \tag{24}$$

Equation 22 describes the phase mismatch per unit length and equation (23) - (24) are the coupling coefficients. If the waveguides are of identical materials so $n_1 = n_2$ and $\beta_1 = \beta_2$ the guides are said to be phase matched and $\mathcal{C}_{21} = \mathcal{C}_{12} = \mathcal{C}$. The optical power in the waveguides are proportional to mode amplitudes, $P_1(z) \propto |a_1(z)|^2$ and $P_2(z) \propto |a_2(z)|$. If there is no light entering waveguide 2, i.e. $a_2(0)$, the transmission of power between the guides can be described by

$$P_1(z) = P_1(0)\cos^2 \mathcal{C}z \tag{25}$$

$$P_2(z) = P_2(0)\sin^2 \mathcal{C}z \tag{26}$$

Under these conditions there can be complete power transfer, this happens at a distance $z = L_0 = \frac{\pi}{2\mathcal{C}}$, called the coupling length. At $\frac{L_0}{2}$ it acts as a 50/50 beamsplitter [7].

## 3.4 Waveguides

Optical waveguides can be designed in different ways depending on the intended use. The different designs have the same basic function, confinement of light in a structure and forcing the propagation in a specific direction. The easiest example is the planar waveguide, which confines in one dimension, while channel waveguides and fibers confine the light in two dimensions [7, 12].

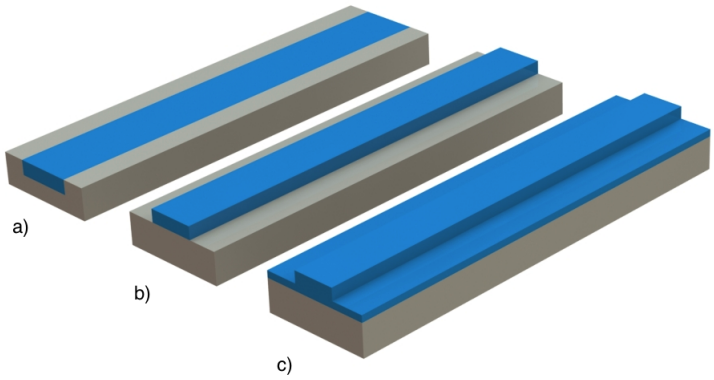


**Figure 3:** a) Channel waveguide b) Strip waveguide c) Rib waveguide

Waveguide structures are the building blocks of integrated optical circuits. Confinement in the waveguide is dependent on the difference in refractive index between the core and cladding, explained by total internal reflection, the core needs to have a higher index than the cladding. In figure 3 the beige areas indicate the lower index medium, whereas the blue areas indicate a higher index medium. The confinement factor ($\Gamma$) in the waveguide can be defined as the power in the core to the total power in the waveguide [7].

$$\Gamma = \frac{\iint_{core} |E(x,y)|^2 \mathrm{d}x\mathrm{d}y}{\iint_{tot} |E(x,y)|^2 \mathrm{d}x\mathrm{d}y} \tag{27}$$

Different mechanisms contribute to losses in optical waveguides. Radiation losses are dependent on the geometry of the circuit design. Avoiding sharp bends, and having sufficient spacing between components minimize the losses due to bending and unwanted coupling. The other sources of loss come from scattering and absorption. Volume scattering is due to crystalline imperfections and impurities in the material, in most waveguides these losses are negligible. Surface scattering has a larger effect even for smooth surfaces, the confined wave will interact strongly with the surface and scattering occurs with each interaction. Absorption is both material and wavelength dependent, in Si the minimum absorption is around 1550nm, which is one of the reasons this wavelength has been extensively used in optical communication systems [7, 8, 9].

Fabricating waveguides on silicon-on-insulator (SOI) is promising for realizing integrated photonic circuits. The manufacturing processes are well known from advances in the semiconductor industry, and it is possible to integrate CMOS technology on the same chip as the optical circuit. One of the challenges is to build an integrated light source in Si, as it does not have a direct band gap it is not suited for this purpose. This need for external light sources leads to additional coupling losses [13].

## 3.5 Effective index method

The effective index method gives an approximation of the propagation constant in an arbitrary 2D structure, with a refractive index in the form $n = n(x, y)$. To find the propagation constant, the problem is divided into separate 1D problems [12].

Consider the wave equation for a 2D waveguide

$$\frac{\partial^2 E(x,y)}{\partial x^2} + \frac{\partial^2 E(x,y)}{\partial y^2} + [k_0^2 n^2(x,y) - \beta^2]E(x,y) = 0 \tag{28}$$

The propagation constant $\beta$ is related to the effective index $n_{eff}$ by $\beta = k_0 n_{eff}$, where $k_0$ is the vacuum wave number. Further one assumes that the optical field can be written on the form

$$E(x,y) = \Theta(x,y)\Phi(y) \tag{29}$$

Where $\Theta(x, y)$ is the part of the field dependent on the $x$ and $y$ component, whereas $\Phi(y)$ is solely dependent on $y$. Inserting (29) into (28) leads to a system of two coupled differential equations

$$\frac{\partial^2 \Theta(x,y)}{\partial x^2} + [k_0 n^2(x,y) - k_0^2 n_{eff}^2(y)]\Theta(x,y) = 0 \tag{30}$$

$$\frac{\partial^2 \Phi}{\partial y^2} - (\frac{2}{\Theta}\frac{\partial \Theta}{\partial y} + (k_0^2 n_{eff}^2(y) + \frac{1}{\Theta}\frac{\partial^2 \Theta}{\partial y^2} - \beta))\Phi = 0 \tag{31}$$

(30) is first solved using the y coordinate as a parameter. The eigenvalue solution gives an effective index profile $n_{eff}(y)$, which depends explicitly on y. This function is introduced in (31), which is the second step to resolving the problem [12]. Assuming $\Theta(x, y)$ is slowly varying with respect to the y coordinate leads to (31) in the form

$$\frac{\partial^2 \Phi}{\partial y^2} + [k^2 n_{eff}^2(y) - \beta]\Phi = 0 \tag{32}$$

We have obtained a decoupled differential equation, which is very similar to the wave equation of a planar waveguide. Solving (32) gives the effective index of the propagating mode in the 2D waveguide we started with [12].

## 3.6 Ring resonator

As mentioned in the beginning of this chapter, the RR and MZI are the main components of a vernier enhanced sensor. In this section there will be a thorough analysis of the RR and how it can be utilized in a sensor. The RR is a circular or racetrack shaped resonator, which can be manufactured with known lithographic techniques. In figure 4 the blue areas represent the guiding high index medium and the beige, a lower index medium. In both illustrations there is no cladding medium except air.

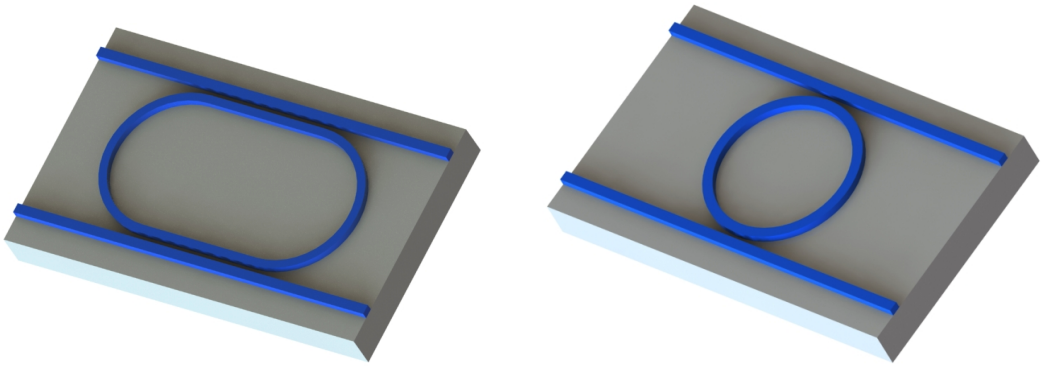

**(a)** **(b)**

**Figure 4:** Illustration of different ring configurations. (a) Racetrack shaped resonator, (b) Circular shaped resonator. The blue area is the higher index guiding material, beige represents the substrate.

To see how a RR can act as a filter or sensor we need to analyze and determine some of the parameters that alters the resonance and behaviour of the RR. As other optical resonators, RR's are based on interference. When light travels in a resonator, only certain wavelengths will propagate depending on the geometry and material properties of the resonator. The resonating condition for wavelengths in a RR are

$$\lambda_m = \frac{n_{eff} L}{m} \tag{33}$$

In the above equation $\lambda_m$ is a resonance peak, $n_{eff}$ the effective refractive index, $L$ is the total length of the ring and $m$ is an integer.

If we first consider a simple RR and one waveguide, see figure 5, the coupling between the ring and the waveguide can be analyzed as two port system.
As a reciprocal system where the coupling itself is lossless, it can be expressed on matrix form. The transfer matrix must then be unitary and in the form shown in below: [14]

$$\begin{pmatrix} U_1^- \\ U_2^+ \end{pmatrix} = \begin{pmatrix} t & \kappa \\ -\kappa^* & t^* \end{pmatrix} \begin{pmatrix} U_1^+ \\ U_2^- \end{pmatrix} \tag{34}$$

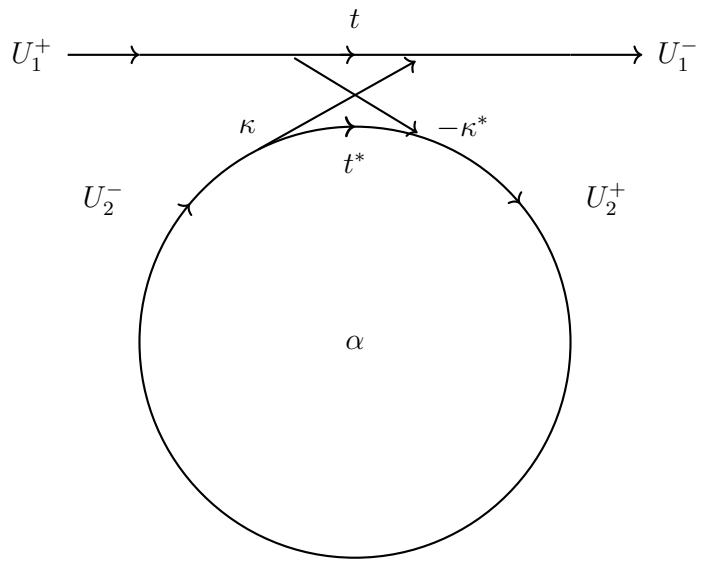


**Figure 5:** RR configuration with a single waveguide, also called a notch filter [14].

where

$$|\kappa^2| + |t^2| = 1 \tag{35}$$

$\kappa$ and $t$ are the coupling and transmission coefficients respectively. Furthermore the ring itself introduces some loss $\alpha$ and phase $\phi$, accumulated after one round trip.

$$U_2^- = \alpha e^{-j\phi} U_2^+ \tag{36}$$

From these relations we get the following [14]

$$U_1^- = \frac{|t| - \alpha e^{-j(\phi-\phi_t)}}{1 - |t|\alpha e^{-j(\phi-\phi_t)}} U_1^+ e^{-j\phi_t} \tag{37}$$

In equation (38) the transmission coefficient is separated into transmission loss $|t|$ and a phase $\phi_t$.

$$t = |t| e^{-j\phi_t} \tag{38}$$

From these relations we can get an expression for the power exiting the waveguide at resonance [14]

$$P_1^- = |U_1^-|^2 = \frac{|t|^2 + \alpha^2 - 2|t|\alpha\cos(\phi - \phi_t)}{1 + \alpha^2|t|^2 - 2|t|\alpha\cos(\phi - \phi_t)} |U_1^+|^2 \tag{39}$$

On resonance: $\phi - \phi_t = 2\pi m$. It is clear that when $\alpha = |t|$ there is no power exiting the waveguide, this is called critical coupling. So under the right conditions this acts as a filter.

If a second waveguide is added on the opposite side of the ring, as shown in figure 6, we end up with an add-drop configuration.

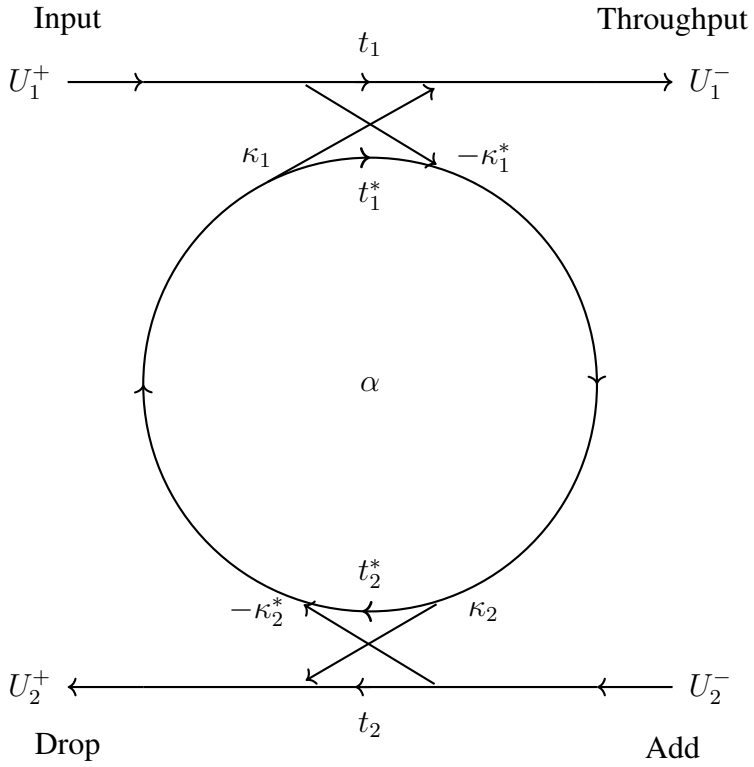


**Figure 6:** Add-drop configuration consisting of a ring and two waveguides separated an equal distance from the ring [14]

Using the same approach as in the previous example, and for simplification setting $U_1^+ = 1$, the drop port power at resonance can be shown to be [14]

$$P_2^+ = |U_2^+|^2 = \frac{(1 - |t_1|^2)(1 - |t_2|^2)\alpha}{(1 - \alpha|t_1 t_2|)^2} \tag{40}$$

If the two ports are symmetrical, $t_1 = t_2$, and for this example we let the ring be lossless, $\alpha = 1$, then it is clear from equation (40) that all the power exits through the drop port at resonance.

In figure 7 the transmittance of an example ring with a length of $148\mu m$, $\kappa^2 = 0.5$, $n_{eff} = 1$ and $\alpha = 1$ is plotted in matlab over an interval from $1.54\mu m$ to $1.56\mu m$.

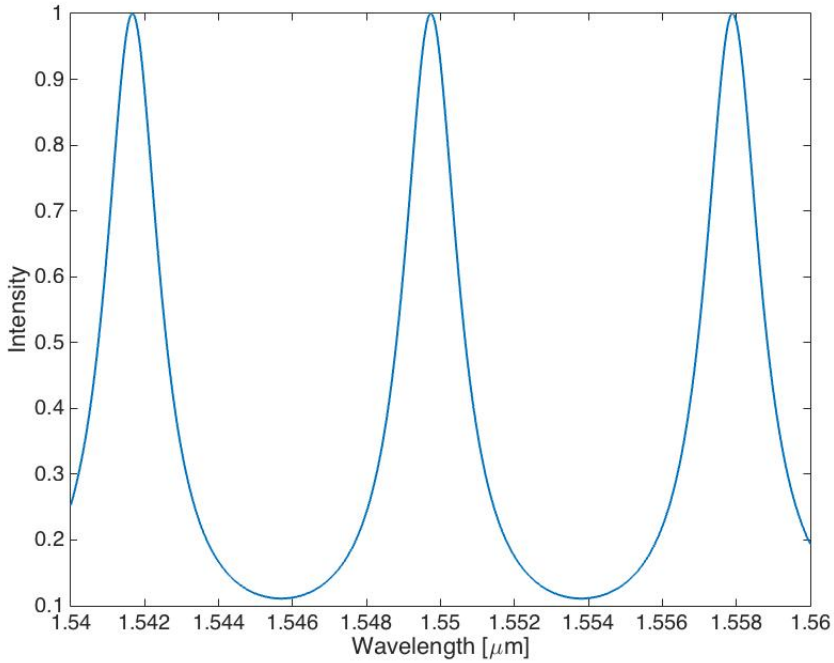


**Figure 7:** Drop port power $P_2^+(\lambda)$ in a example ring with radius $148\mu m$, $\kappa^2 = 0.5$, $n_{eff} = 1$ and $\alpha = 1$

As for most components there are some figures of merit describing the properties of the RR. The free spectral range (FSR) is the distance between the resonant peaks, and a simple approximation is shown below:

$$\text{FSR} = \frac{\lambda^2}{n_{eff}L} \tag{41}$$

If the effective index, $n_{eff}$, is strongly wavelength dependent, the group refractive index $n_g$ can be used instead of $n_{eff}$ [14].

$$n_g = n_{eff} - \lambda\frac{\partial n_{eff}}{\partial\lambda} \tag{42}$$

Another important parameter is the full width half maximum (FWHM), which is the width of the resonance lineshape, $\delta\lambda$, at 3dB, by assuming weak coupling and $\lambda >> \delta\lambda$ the following expression can be obtained [14].

$$\text{FWHM} = \frac{\kappa^2\lambda^2}{\pi L n_{eff}} \tag{43}$$

From this we can deduce the finesse, $\mathcal{F}$ which is closely related to the Q factor of the device.

$$\mathcal{F} = \frac{\text{FSR}}{\text{FWHM}} = \frac{\pi}{\kappa^2} \tag{44}$$

$$Q = \frac{\lambda}{\text{FWHM}} = \frac{n_{eff}L}{\lambda}\mathcal{F} \tag{45}$$

The Q factor is a ratio of how much power is stored in the ring to how much is lost per cycle. When the light travels in the resonator the intensity builds up, and can exceed the intensity in the waveguides. For a lossless resonator with $\kappa_1 = \kappa_2 = \kappa << 1$ the build up factor, B is: [14]

$$\text{B} = \frac{\mathcal{F}}{\pi} \tag{46}$$

From theses relations it is clear that the RR has the potential to act both as filter or sensor. There are other ways to analyze the spectral response of the RR, some readers could find this more intuitive and are referred to look at the Z-transform and Masons rule [14].

We now consider the RR configuration in figure 6 acting as a sensor, where a change in resonance is the observable. From equation (33) there are two parameters that affect $\lambda$, either $L$ or $n_{eff}$. When detecting the presence of specific molecules it is intuitive to consider changes in $n_{eff}$ rather than $L$. The cladding covering either parts or the whole ring, can be manufactured in such a way that it is sensitive to environmental changes. How it should interact with its surroundings is dependent on the environment and which compounds to detect. Some examples are either absorption of a compound in the cladding material itself, or a window etched in an inert cladding and left open to the surroundings. When the cladding index $n_c$ changes, it alters $n_{eff}$ to some degree, this is called homogeneous sensing. An analytical expression for the wavelength shift, $\Delta\lambda$ can be deduced from equation (33).

$$\Delta\lambda = \frac{\lambda}{n_g} S_w \Delta n_c \tag{47}$$

where $S_w$ is the waveguide sensitivity, and $\Delta n_c$ is the change in refractive index due to a environmental change. $S_w$ is defined as [15, 16].

$$S_w = \frac{\partial n_{eff}}{\partial n_c} \tag{48}$$

## 3.7 Mach Zehnder interferometer

A basic Mach-Zehnder interferometer can be explained, and also realized by a system of mirrors and beam splitters [7]. Another possibility is using waveguides to construct it, which is what the focus will be in this section.

The waveguide MZI consists of an input, output and two arms, one sensing arm and a reference. In figure 8 the waveguide structure is blue, beige is the lower index medium and the cladding is air.

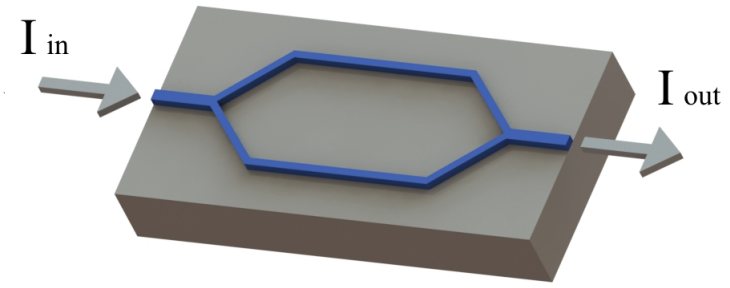


**Figure 8:** An illustration of a MZI consisting of a input waveguide, output waveguide and two straight waveguides which are called the arms of the MZI.

We consider a monochromatic light source as the input, and a symmetric waveguide structure that is designed such that it supports a single TE mode. The light will propagate in the two arms and recombine at the output. If there is difference in the refractive index in the arms, $\Delta n$, there will be a phase difference between the light in the two arms. At the output, the two fields either interfere constructively or destructively. Assuming the waveguides are lossless we can set up an expression for $I_{out}$ out referenced to $I_{in}$:

$$\frac{I_{out}}{I_{in}} = \frac{1}{2}(1 + \cos(2\pi \frac{\Delta n L}{\lambda})) \tag{49}$$

There are some issues with a monochromatic design, mainly because of the periodic output signal. If some change in the sensing arm leads to a phase shift, which is an integer multiple of $2\pi$, these values can not be separated. Because of this periodicity, the sensitivity is not constant either, and the sensor needs to be biased properly and away from extremal points [17].

There is a different technique that can avoid some of these issues, and potentially increase the sensitivity and resolution. This comes at the expense of requiring a broadband light

source, and an optical spectrum analyzer (OSA) to read out the transmission spectrum. If we consider such a device where the initial difference $\Delta n = 0$, the transmission spectrum of the MZI would be equal to the spectrum of the light source.
As the device should be used as a sensor, the sensing arms cladding would typically not have the same effective index as the reference arm. This leads to an intrinsic difference in $\Delta n$, which is similar to the bias point in the monochromatic design. This could further be compared to the FSR of the RR, so a $\text{FSR}_{MZI}$ can be defined as the frequency difference of two adjacent maxima in the transmission spectrum at rest [15].

$$FSR_{MZI} = \frac{\lambda^2}{L\Delta n_{g,MZI}} \tag{50}$$

Here $L$ is the length of the arms, assuming they are the same length, and $\Delta n_g$ is the difference in group index between the reference and sensing arm. What we observe in a MZI is a phase change, unlike a RR, where the observable is a shift in resonance. Because of this, the sensitivity of a MZI is proportional to the length of the device, or more accurately, the length of the arms. We can still deduce an expression for the wavelength shift of the resonant peaks, $\Delta\lambda_{MZI}$, when there is an environmental change on the sensing arm, this is very similar to expression (47) in the previous section.

$$\Delta\lambda_{MZI} = \frac{\lambda}{\Delta n_{g,MZI}} S_w \Delta n_c \tag{51}$$

As mentioned in earlier chapters, the waveguides should be constructed so it supports only one fundamental mode, either a TE-like or TM-like mode. The bends in the two junctions also have an impact on the performance. Two common designs are either Y-bends as depicted in figure 8, or more S-shaped bends. The main criteria should be a structure with minimum loss.

## 3.8 Vernier effect

In the two sensor principles described in the previous section the wavelength shift needs to be larger than the resolution of the OSA. To improve the detection limit so it can detect minute changes in the index, some kind of enhancement is needed. Introducing the vernier effect, which is commonly utilized in vernier calipers. To achieve the vernier effect, two different scales are needed, where one of the scales slides over a stationary one. The measurement is made when the two scales overlap. This same concept can be used in photonic sensors [18]. The theory has been applied mainly to cascaded RR's, but has shown to be applicable to a RR cascaded with a MZI [15]. The concept will first be introduced by using two RR's, followed by a theoretical description of a RR and MZI setup.

The transmission spectrum of the two cascaded rings is the product of their individual spectrum. Consider two rings of different length, from equation (41) it is evident that they exhibit different FSR's. The cascaded system will thus have transmission peaks where the two spectrum's overlap. When working as a sensor, one ring would be kept as the stationary part of the scale with FSR $=$ FSR$_{filter}$. The other is exposed to the sensing environment, with FSR $=$ FSR$_{sensor}$. When the sensor rings transmission peaks are slightly shifted due to an environmental change, the point of overlap changes. This can be designed such that the systems overall resonance shift is larger than the shift in the individual sensor ring [18].

There are two different regimes this configuration could operate in. The first regime occurs when $|\text{FSR}_{filter} - \text{FSR}_{sensor}|$ ($\Delta$FSR) is large compared to the FWHM of the individual transmission peaks. When there is a change in the index, the more isolated transmission peaks will shift, see figure 9.

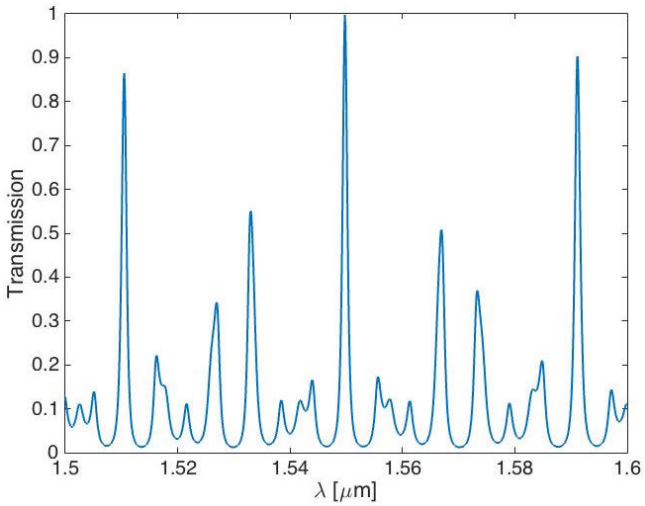


**Figure 9:** Transmission spectrum when $\Delta$FSR $>$ FWHM

This is in general not suitable for sensing applications, since it is harder to relate the spectral shift to a concentration change in the sensing arm material [16, 18].

In the second regime, where $\Delta$FSR $<$ FWHM, the transmission will form a periodic envelope superimposed on the transmission spectrum, see figure 10.

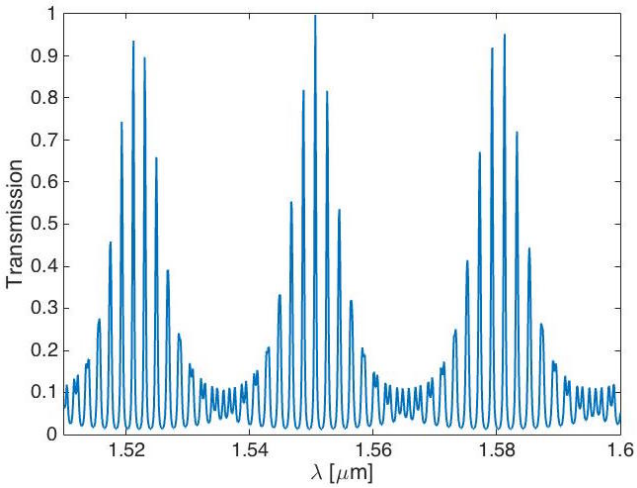


**Figure 10:** Transmission spectrum when $\Delta FSR < FWHM$

Not taking dispersion into account, it can be shown that the period of the envelope can be written as [18]:

$$\frac{FSR_{sensor} \cdot FSR_{filter}}{\Delta FSR} \tag{52}$$

Consider figure 11, both rings have a resonance at $\lambda_0$ when the system is at rest, and $\text{FSR}_{filter} < \text{FSR}_{sensor}$. If there is an upward shift in the resonances of the sensor, equal to the spectral distance $\Delta$FSR, the peak resonance of the envelope would also shift upwards a distance $\text{FSR}_{filter}$, and overlap at $\lambda_1$.
When $\text{FSR}_{filter} > \text{FSR}_{sensor}$, figure 11 looks slightly different, in this case the peak resonance of the envelope would shift downwards. In both cases it is clear that the resonance shift of the sensor is multiplied by a factor $G_v$: [18]

$$G_v = \frac{\text{FSR}_{filter}}{\Delta\text{FSR}} \tag{53}$$

In section 3.6 we deduced equation (47) which is an expression for the wavelength shift due to an environmental change. We can now set up an expression for the total shift for the vernier enhanced sensor, $\Delta\lambda_{tot}$

$$\Delta\lambda_{tot} = G_v \cdot \Delta\lambda \tag{54}$$

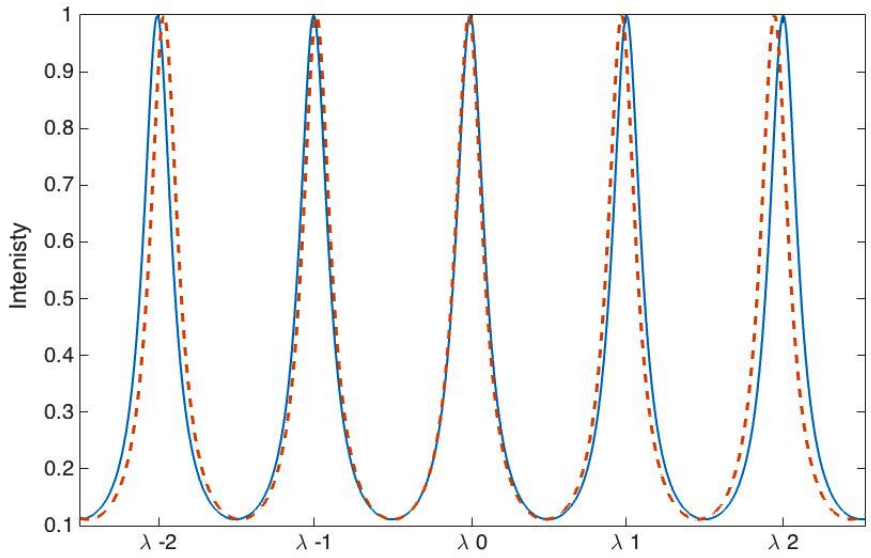


**Figure 11:** Transmission of filter (solid line), and sensor (stippled line)

The configuration with a MZI instead of a ring acting as the sensor, is based on the same concept. In section 3.7 we defined the FSR$_{MZI}$ and the shift in resonance $\Delta\lambda_{MZI}$. Assume this vernier enhanced MZI is made in the same materials, same waveguide geometry and a resonance at $\lambda_0$, just as the previous vernier enhanced RR sensor. From this it is viable to make an comparison of the two configurations. From equations (51) and (47) we get a relation between the overall resonance shift [15]:

$$\frac{\Delta\lambda_{MZI}}{\Delta\lambda_{RR}} = \frac{n_{g,RR}}{\Delta n_{g,MZI}} = \frac{1}{1 - \frac{n_{g,2}}{n_{g,1}}} = G_s \tag{55}$$

Where $n_{g,2}$ is the group index in the cladding covering everything except the sensor window, and $n_{g,1}$ is the group index in the sensing arm. From equation (55) a small $\Delta n_g$ will increase $G_s$, resulting in a larger shift compared to a RR. As the sensor should operate in the second regime, the criteria $\Delta\text{FSR} < FWHM$ imposes different requirements to the length of the MZI arms. From equation (50), which gives the relationship between FSR$_{MZI}$, $\Delta n_g$ and the length implies that when $\Delta n_g$ decreases, the length has to increase. Extremely long arms are undesirable both in terms of loss and footprint. There is thus a trade off between the length and sensitivity [15]. An expression to minimize $\Delta$FSR and increasing $G_v$, with a given ring length is seen in equation 56 [15].

$$L_{MZI} = L_f \frac{n_{g,2}}{n_{g,2} - n_{g,1}} \tag{56}$$

We can now define the overall wavelength shift of the vernier enhanced MZI as

$$\Delta\lambda_{tot} = G_v \frac{\lambda_0}{\Delta n_g} S_w \Delta n_c \tag{57}$$

Overall sensitivity

$$S_{overall} = \frac{\Delta\lambda_{tot}}{\Delta n_c} = G_v \cdot \frac{\lambda_0 S_w}{\Delta n_g} \tag{58}$$

and limit of detection (LOD)

$$LOD = \frac{\Delta\text{FSR}\ \Delta n_g}{\lambda_0 S_w} \tag{59}$$

## 3.9 Methane sensitive layer

Part of the sensor needs to be sensitive to environmental changes, this means that we need a material that not only suits the application, but that is also possible to bond to the optical chip. One group of materials that meet these criteria are polymers. Polymers are chains of repeated monomers, a molecule that can chemically bind to other molecules of the same type, forming a polymer. In general polymers are amorphous solids with a varying degree of order, but there are also crystalline polymers, which have a more ordered arrangement of the chains. These are in general stronger and stiffer than their amorphous counterpart [19].

How the polymer act as a bulk material is controlled mainly during synthesis. By controlling temperature, the polymer goes through different regimes. The glass transition is one of the most common when describing how the polymer acts in bulk. Below the the glass transition temperature ($T_g$) a polymer is solid and more brittle, called the glassy state. Above it is in a liquid state, and behaves as a rubber. The mechanical properties does not only change with temperature, but also with applied loads over time. This is because the bonds in the bulk can easily be broken by external forces [19].

Polydimethylsiloxanes (PDMS) are one family of polymers which have very useful properties, they are inherently hydrophobic, have low solubility, a low glass transition temperature ($T_g \approx -125°\text{C}$) and are stable against ozone, atomic oxygen and oxygen plasmas [20].

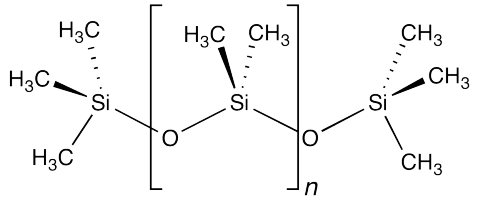


**Figure 12:** PDMS structure, the monomer is in between the square brackets and denoted n, from [21]

PDMS has a lot of applications, it has been used extensively to produce prototypes of microfluidic devices, mechanical interconnections between Si layers and for producing membranes [22]. Silicone polymers can be synthesized in a three step process. First methylchloride flows over a silicon metal powder, the intended reaction occurs at temperatures between 250 and 350 °C, and a pressure of 1 - 5 bars. During this reaction different silanes are created, where dimethyldichlorosilane, $Me_2SiCl_2$ has the highest yield. After $Me_2SiCl_2$ is separated from the other silanes, it becomes the monomer for hydrolysis of PDMS. [20] The chains obtained in the hydrolysis are too short for most applications, so they need an additional process of further polymerisation. This process and the chain length are dependent on the interaction with a substance capable of giving the chain ends. Potassium hydroxide (KOH) could be used in polymerisation of $Me_2SiO$, the chain length

can be manipulated since it is dependent on the KOH concentration [20].

The binding between PDMS and $Si/SiO_2$ is often enhanced to withstand higher pressures, strain and stress. Epoxys that are UV curable are often used as a bonding agent between the surface and PDMS. Other common techniques are anodic bonding and fusion bonding, both requiring either external pressure or high curing temperatures [23].

To make the PDMS layer methane sensitive it needs an additional component, this is where Cryptophanes comes into the picture. Cryptophanes are a group of supramolecular systems that can reversibly encapsulate neutral target molecules [24, 25]. The cryptophanes exhibit high selectivity towards different species depending on the specific cryptophane. Both cryptophane-A and cryptophane-111 have shown high affinity towards Xe, but also towards $CH_4$ [26, 24]. The target molecules diffuse into the cavity, and once inside they are held in place by weak van-der-Waals forces. The molecules are made up of two cyclotriguaiacylene (CTG) units, connected by three alkane linkers [26]. The CTG's are the bowl like structures, see figure 13. The cavities formed in Cryptophane are lipophilic, which enable them to capture neutral molecules dissolved in an aqueous solution [24].

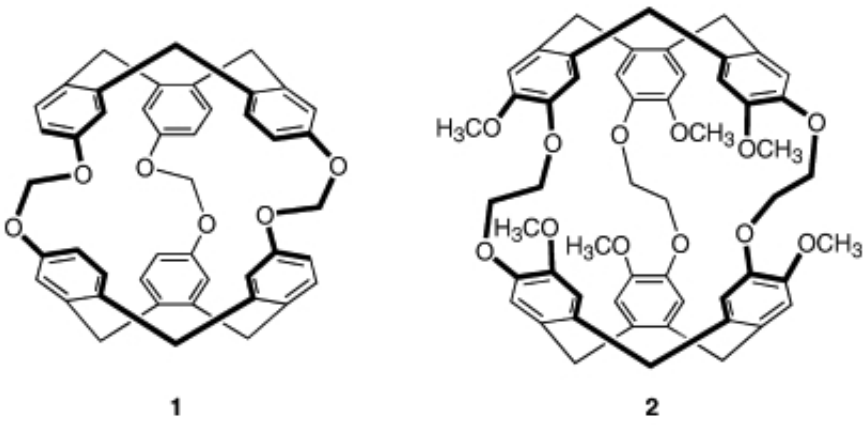


**Figure 13:** 1) Cryptophane-111, 2) Cryptophane-A

The synthesis of Cryptophane-A requires multiple steps, different ways have been proposed, all with different yields and number of steps. The preparation of the CTG's and connecting links are time consuming, partially because it is important to control the process to avoid the creation of unwanted side products [26]. In the procedure described in [26] the synthesis starts with vanillyl alcohol, dibromoethane, and dihydroxybenzaldehyde, where after a series of steps they managed a final yield of 5.8%. The process is complex and outside the scope of this paper, an illustration of the process can be seen

in figure 14. When separated after synthesis, Cryptophane-A comes in powder form and needs a supporting structure, two polymers, PDMS and SAN have already been proved to work well as a host [27, 28]. When $CH_4$ enters the cavity it has been shown that it behaves as part of the cryptophane, and increases the refractive index of the bulk polymer proportional to the amount of encapsulated $CH_4$ [25].

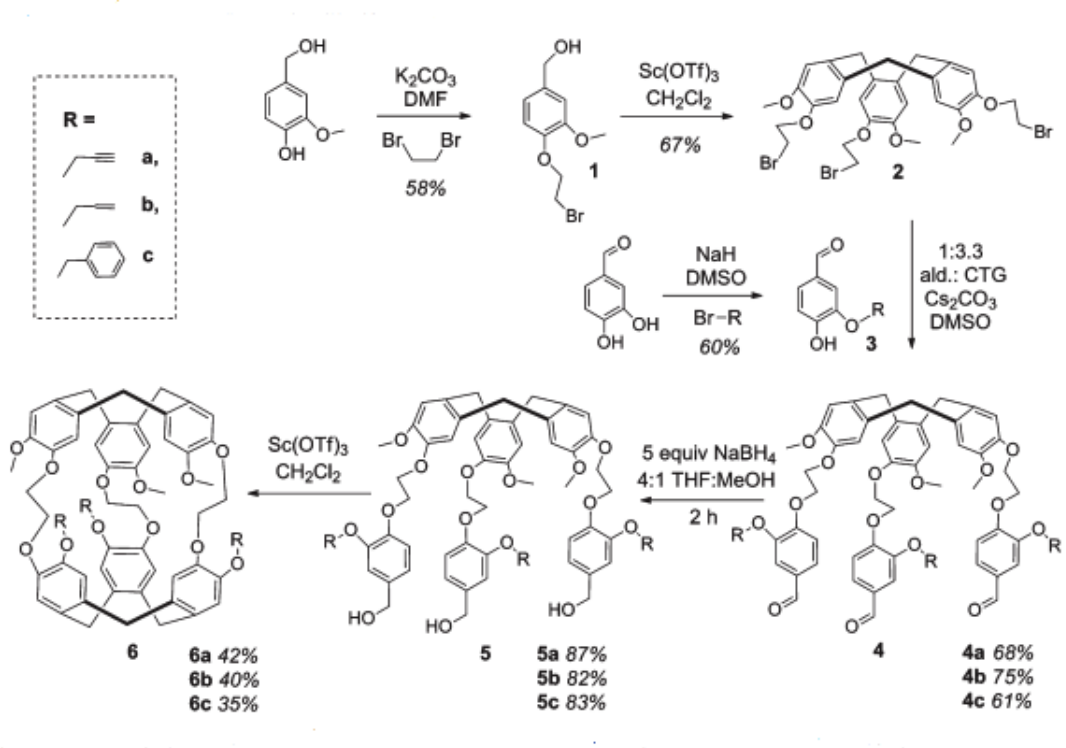


**Figure 14:** Synthesis of Trisubstituted Derivatives of Cryptophane-A [26]

# 4 Sensor Design

In the project thesis the concept and initial design was researched thoroughly. The starting point was based on the work in [15, 16, 18, 28, 29] and further developed to meet the requirements in both the project- and master thesis. The theoretical design proposed consists of a RR cascaded with a MZI exploiting the vernier effect, which theoretically increases the sensitivity compared to the MZI or RR acting as the sensor by themselves. In figure 15 a illustration of the device can be seen. The etched window over one of the arms will be filled with PDMS loaded with Cryptophane, this polymer acts as the methane sensitive layer.

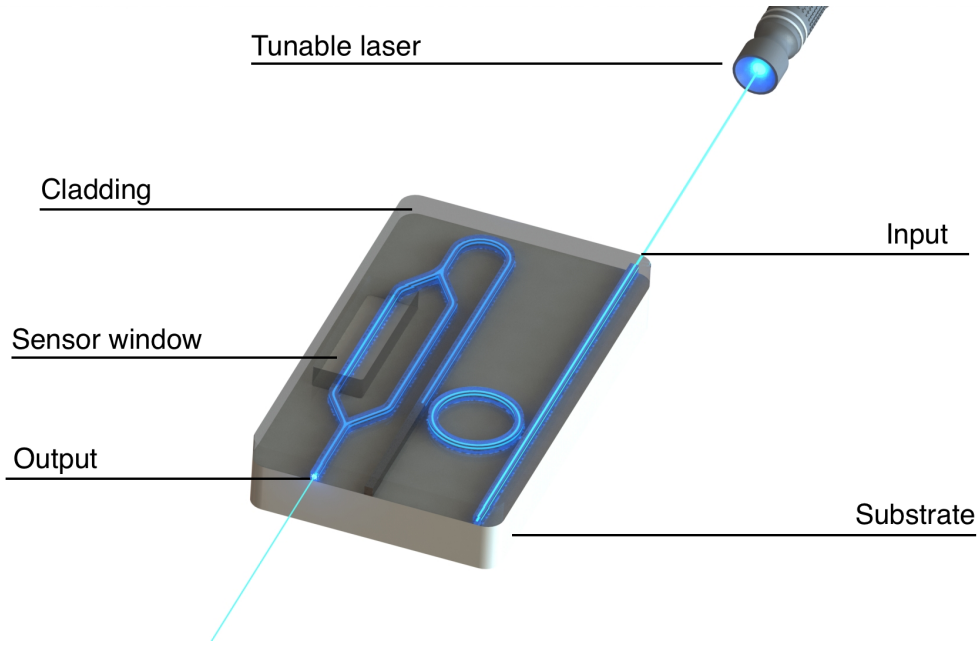


**Figure 15:** Illustration of sensor design, waveguide structure is marked blue

The strip waveguides are 500 nm x 220nm, fabricated on a SOI platform. The light source is a tunable laser capable of tuning over a range of 70 - 100 nm around a center wavelength close to 1550 nm. The read out is performed using an optical spectrum analyzer.

The sensor is first modeled and fabricated with the window left open to the environment, effectively filling the window with air. The reason for using air instead of PDMS, is to observe the output spectra using a shorter MZI. The reduction in length is due to a larger intrinsic difference in the refractive index. $SiO_2$ has an refractive index $n = 1.45$ and PDMS/cryptophane has $n = 1.42$. Air is considered to have a refractive index $n \approx 1$, at standard ambient temperature and pressure. Modeling this shorter version would greatly increase the effectiveness of the simulations. Regarding the fabrication process, both producing the PDMS/Cryptophane polymer and filling the sensor window is complex. The ratio of PDMS and Cryptophane has to be correct, and the PDMS layer needs to be bonded to the $Si/SiO_2$ surface. In this thesis the results from the work with a open sensor window are used to argument for the behaviour of the sensor with a PDMS/Cryptophane filled sensor window.

The initial design parameters are a filter with a FSR $\approx 3$ nm, this value was used in the theoretical sensor proposed in the project thesis and based on the work done on similar sensors.

# 5 COMSOL Analysis

This section will describe how to build the optical models in COMSOL Multiphysics®. The results from the simulations are both used to verify the theory, and also predict the behaviour of the physical sensor. All models are made in 2D because of the intensive memory requirements performing 3D simulations of similar size.

In the project thesis the complete sensor had to be divided into its components, and the actual resonance shift was not simulated. After the characteristics of each part where determined, this was used to validate the theoretical model. The results where inconsistent with theory, which made it challenging to accurately calculate other essential values. The most essential values from the simulations are the FSR of both the ring and MZI, the effective index, sensitivity and finally a estimation of the group index ($n_g$). The difference in the $n_g$ is one of the deciding factors on the length restrictions of the MZI arms according to equation 50. The refractive index of the PDMS/Cryptophane layer was taken from [28] and have not been measured in the experimental part. The method on how to build the models and estimate values has changed since the project thesis, to both improve computation time and get more accurate results. All models was completely rebuilt, and every parameter re-calculated. The method will be covered in detail in this chapter along with the results from the analysis.

## 5.1 Mesh configuration

As COMSOL is a finite element software (FEM) it solves PDE's numerically by dividing the problem into smaller domains and then give an approximation of the exact solution. The mesh is the collection of these domains, and it is important to define this properly. There are several different types of mesh one can apply to the models, but one common factor applies; the more domains solved for, the closer the approximate solution comes to the accurate solution.

The standard physics controlled mesh used in COMSOL is the free triangular mesh, and in figure 16 the other most common mesh components are illustrated. To resolve a wave properly, it is necessary to use about 10 linear (or five 2nd order) elements per wavelength [30]

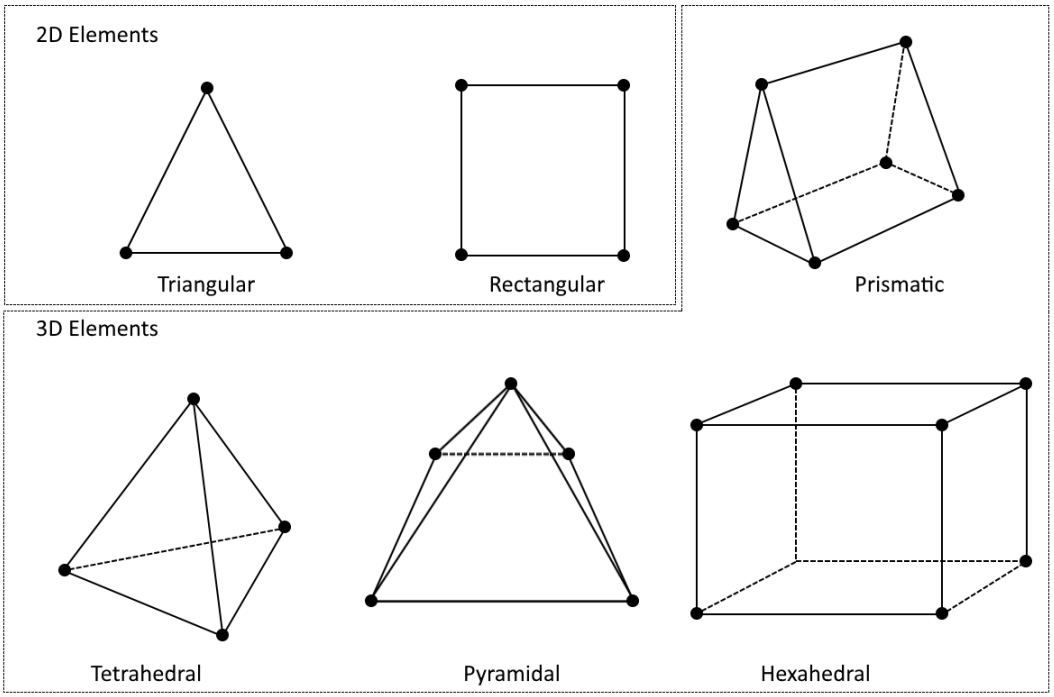


**Figure 16:** An overview of linear mesh elements from [1]

## 5.2 Boundaries and S-parameter

The boundary conditions are an important factor in all models, the boundary conditions (BC) between dielectric media were discussed in section 3.2, and the same theory is applied in COMSOL. There are different boundary conditions which can be applied to the model edges. In the wave-optics module, ports are one type of BC, it defines the input and output for the excited EM wave. After the ports are defined a boundary mode analysis is conducted on each individual port, this determines the propagation constant for the wave. Another parameter which is determined from the port boundary mode analysis is the S-parameter. And for a single mode waveguide structure, the S-parameter is used to describe the power flow on the different ports [30]. The S-parameters are used extensively to interpret the behaviour of the different components, as it is a complex number the power is described by $|S_{ij}|^2$, where $ij$ represents port numbers, e.g. $|S_{21}|^2$ describes the power flow from port 1 to port 2.

Besides the port boundary condition the remaining boundaries are set as a scattering boundary condition. This BC effectively makes the boundary transparent for any scattered waves, i.e. they are not reflected at the boundary [30]. There is an additional method to achieve the same result, this is called a perfectly matched layer (PML). This acts as a domain that absorbs most of the incoming radiation. Mathematically speaking, the PML is a domain that has an anisotropic and complex-valued permittivity and permeability [31]. The PML was used in the project thesis and worked well with the frequency domain. The scattering boundary condition also proved to give good results when compared to the models with a PML. It was chosen over the PML, as this increases the total amount of domains to solve for.

## 5.3 Determination of effective index

When simulating wave optics in 2D, one of the most significant difficulties is the loss of one dimension. This leads to a different mode distribution than in the physical strip waveguide. The models are built from a perspective looking down on the structure, as shown in figure 17.

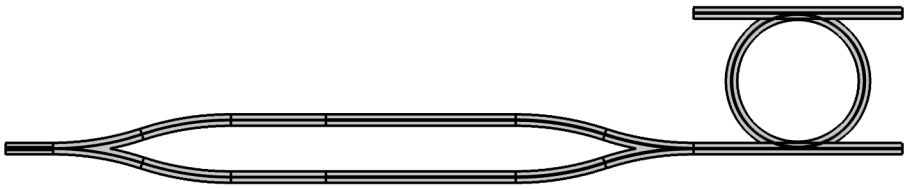

**Figure 17:** COMSOL model representing a ring resonator cascaded with a Mach Zehnder, seen from the top down perspective.

As the strip waveguide is 500 nm wide and 220 nm high, it is intuitive to assume that the most accurate results are obtained when the waveguide width in 2D is 500 nm. To account for the loss of the height dimension, a modal analysis is first conducted over the cross section of the waveguide, see figure 18. From this analysis an approximation of the effective index can be deduced.

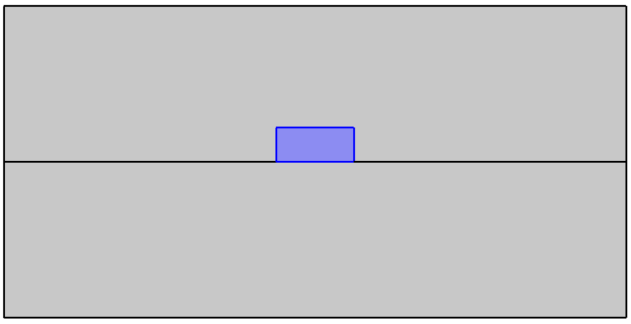

**Figure 18:** Cross section of a 500nm x 220nm strip waveguide, the Si core is marked in blue with a surrounding $SiO_2$ cladding.

The results from the modal analysis can be seen in figure 19.

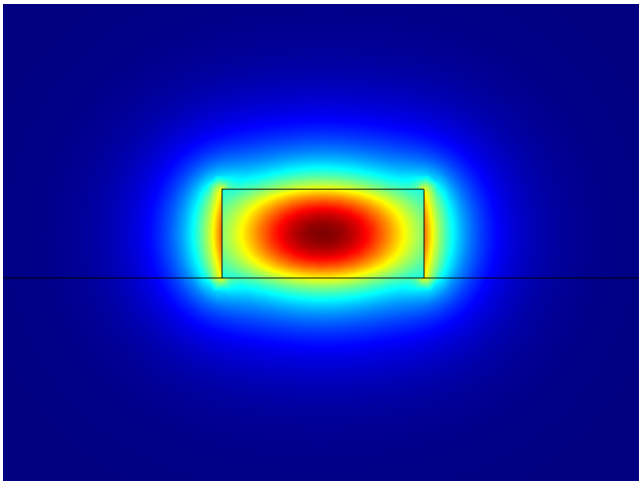

**Figure 19:** Electric field distribution for the strip waveguide in figure 18

This analysis gives a value for the effective index in 3D, but when the model is built from the top down perspective, a more accurate index can be obtained. First the structure is divided into three sections. These sections represent the different domains in the 2D waveguide model, as seen in figure 20.

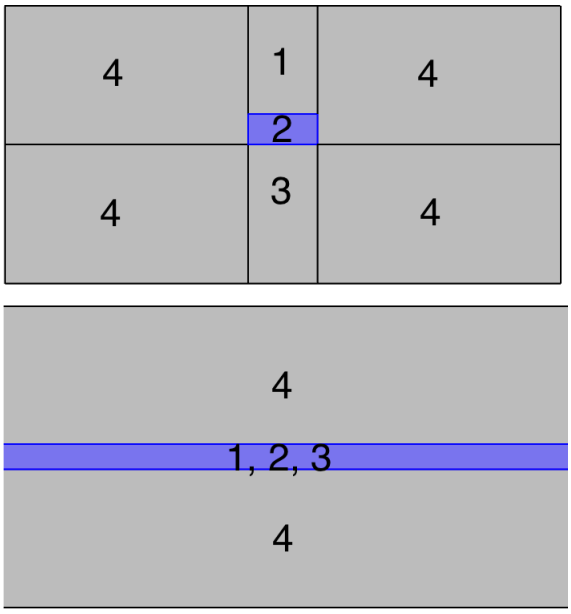


**Figure 20:** Area representation, waveguide core marked in blue.

To determine the index we first integrate over the individual surfaces 1,2 and 3 to determine the total field $|\mathrm{E}|^2$. The percentage of the total field in section 2 is then multiplied with that sections refractive index. This is now set as the effective index of the core in the 2D model. The index of the cladding (section 4 in figure 20) is set to the index of the cladding material.

## 5.4 Beam envelope

In the project thesis the physics model called frequency domain was used. However there is another approach when analysing devices that are large compared to the wavelength, called the beam envelope method. In this method the electric field is expressed as the product of a slowly varying envelope function and a rapidly varying exponential phase function [30]. The main reason to use beam envelope is the ability to use a coarser mesh, thus making the simulation less memory intensive while still getting reasonable results.

Results from the initial test-runs on basic geometries gave inconsistent results, and deemed for a more structured in-depth method. First a boundary mode analysis was conducted on a input port of a straight waveguide, see figure 21, where the port is marked in blue. The model represents a straight waveguide with Si core and $SiO_2$ cladding. The index of the core is set to the effective index found by using the method described in the previous section.

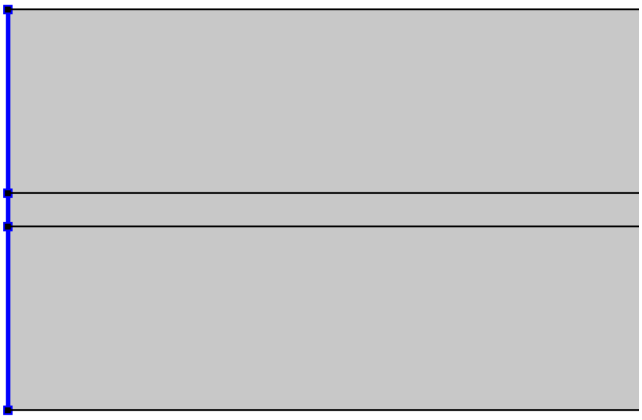

**Figure 21:** 500nm wide waveguide surrounded by a cladding seen from the top down perspective, input port is marked in blue.

The analysis is set to search for 10 modes close to the effective index to check which ones are supported by the structure. From the analysis it is clear that both the fundamental and second order TE mode is supported in 2D, and it seems COMSOL is treating it as a slab waveguide, which is reasonable. The tangential field for the two TE modes on the input port of the 500 nm wide waveguide can be seen in figure 22.

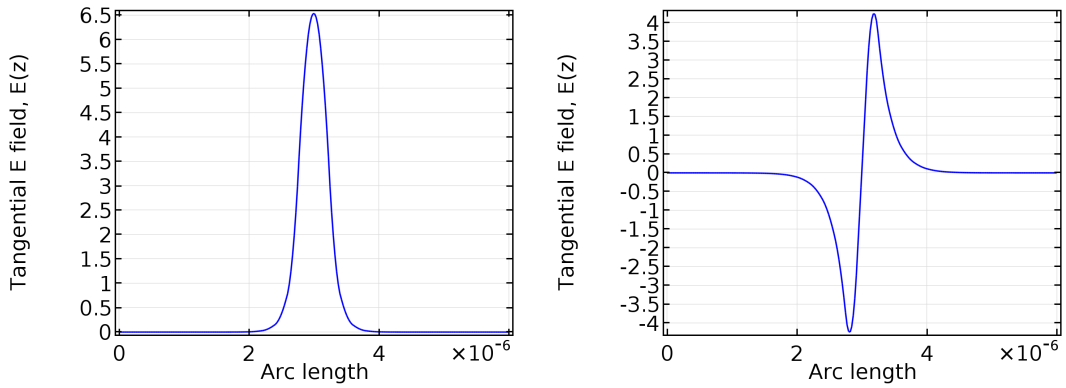


**Figure 22:** Plotted tangential E field on the input port in figure 21 (a) Fundamental TE mode, (b) Second order TE mode.

If one models a similar, only narrower waveguide. It would only support the fundamental TE mode, and the mesh can be extremely coarse. An example is the model of a notch filter seen in figure 23, this model is one of COMSOLs own example models.

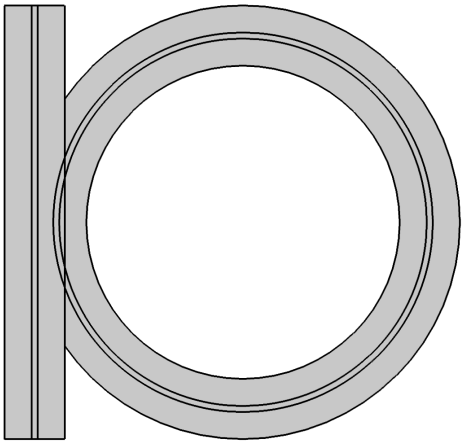

**Figure 23:** COMSOL model of a notch filter

In figure 24 one can see the coarse mesh and the S parameter on the output port.

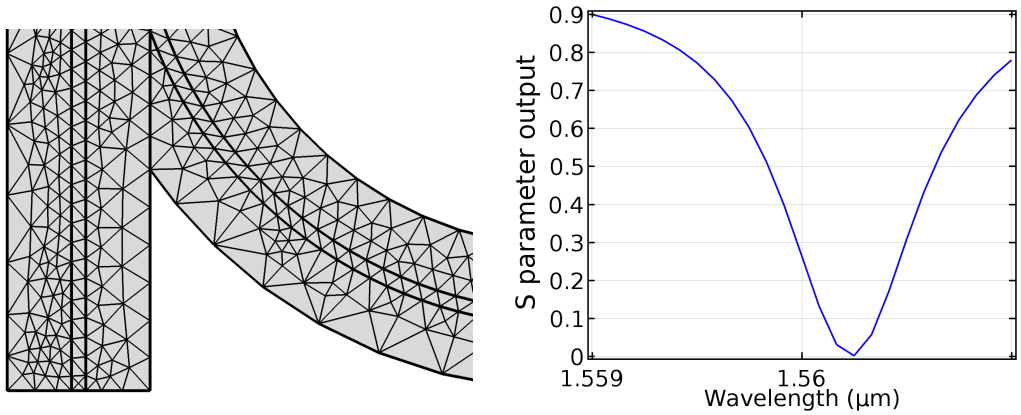


**(a)** **(b)**

**Figure 24:** (a) The mesh on the model in figure 23 with 200 nm wide waveguide, (b) S parameter on output port.

The same model was then rebuilt, only with a 500 nm wide waveguide and a similar coarse mesh, the S parameter on the output from the same sweep can be seen in figure 25.

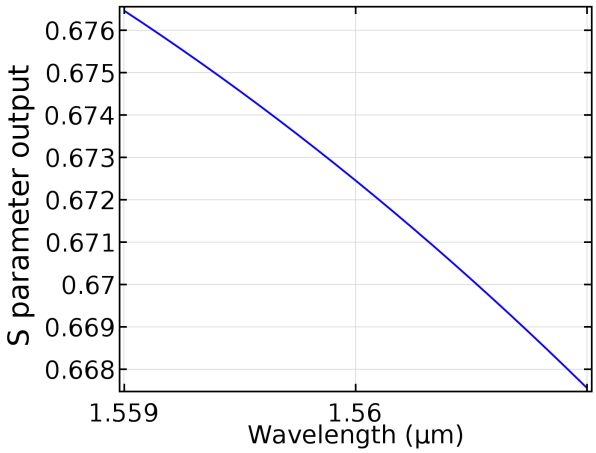


**Figure 25:** S parameter on the output of a notch filter with a 500 nm wide waveguide and coarse mesh.

After refining the mesh significantly the result is resembling 24 (b), only with a slightly lower transmission at the peak, see figure 26. This is due to a slightly different coupling distance and field distribution.

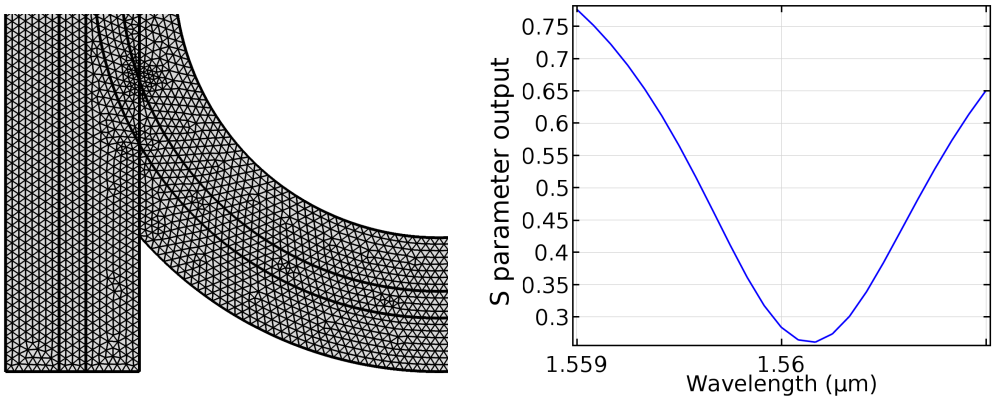


**(a)** **(b)**

**Figure 26:** (a) Refined mesh on the notch filter with a 500 nm wide waveguide, (b) S parameter at the output of the filter.

The solution when simulating 500 nm wide waveguides is to refine the mesh significantly. This is undesirable as using a coarser mesh was one of the reasons for choosing beam envelope. The problem seems to be more significant in bends and curved sections, so the mesh in these sections are set as a fine free triangular mesh. It is still the straight sections in the MZI arms that are by far the largest parts of the model. In these sections an edge can be used along with the mapped mesh, see figure 27, which lower the total domains to solve for, compared to the triangular, while still giving accurate results.

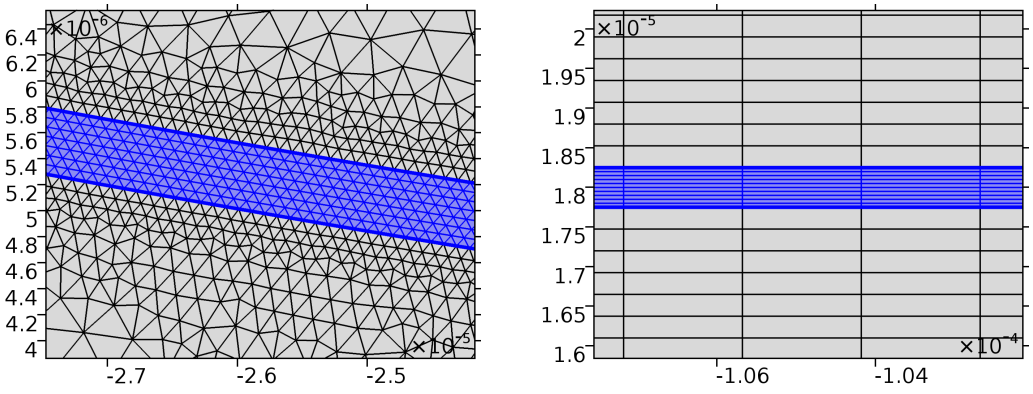


**(a)** **(b)**

**Figure 27:** (a) Triangular mesh, core is marked in blue. (b) Edge with mapped mesh, core is marked in blue.

There are additional ways to reduce the computation time. In all models in this thesis the interesting part is the out-of-plane vector, which corresponds to the TE mode. Some test runs where done solving for all three components. The results showed that the other field components where insignificant with a factor of $10^{-11}$ - $10^{-16}$. Based on this the rest of simulations where only solved for the out-of-plane vector. In figure 28 $E_x$, $E_y$, $E_z$ and the electric field norm is plotted for a straight 500 nm wide waveguide.

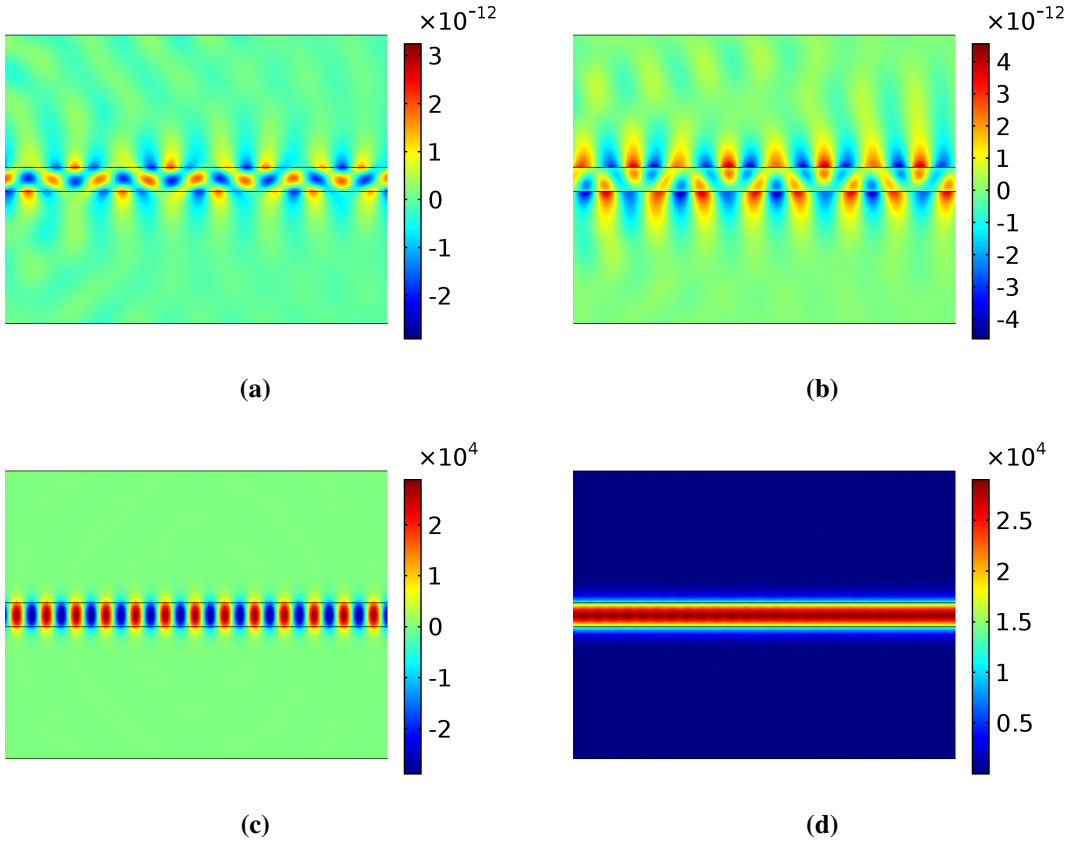


**Figure 28:** Plot of electric field components in a 500 nm wide waveguide. (a) $E_x$, (b) $E_y$, (c) $E_z$, (d) Electric field norm.

## 5.5 Ring resonator

The first model of a ring resonator has a radius of $35\mu m$, the core is Si with a surrounding cladding of $SiO_2$. The separation between ring and waveguide is 150 nm, and the model can be seen in figure 29.

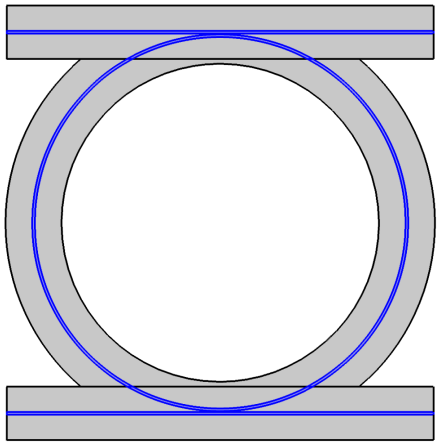

**Figure 29:** COMSOL model of ring resonator with radius of $35\mu m$. The separation between ring and waveguide is 150 nm, which is not clearly visible in the image.

The effective index of the core is determined using the method described in the previous section. To determine the FSR a parametric sweep was done from 1550 nm to 1556 nm. The FSR of this example ring was compared to the theoretical value ($FSR^*$), which was estimated from equation 41 using $n_{eff} = 2.72$. The same ring was also simulated using the frequency domain as this interface has previously given good results. This would also provide additional result to compare with the beam envelope method.

**Table 1:** Comparsion of theoretical and simulated FSR for a ring with $35\mu m$ radius

| | |
|---|---|
| $FSR^*$ | 4.02 nm |
| $FSR_{beam}$ | 4.00 nm |
| $FSR_{freq}$ | 3.93 nm |

The results from both theory, beam envelope and frequency domain differ only by less than an angstrom. The only discrepancy between the two physics interfaces is a minor difference in the resonance, and slightly lower transmittance at the peak. See figure 30.

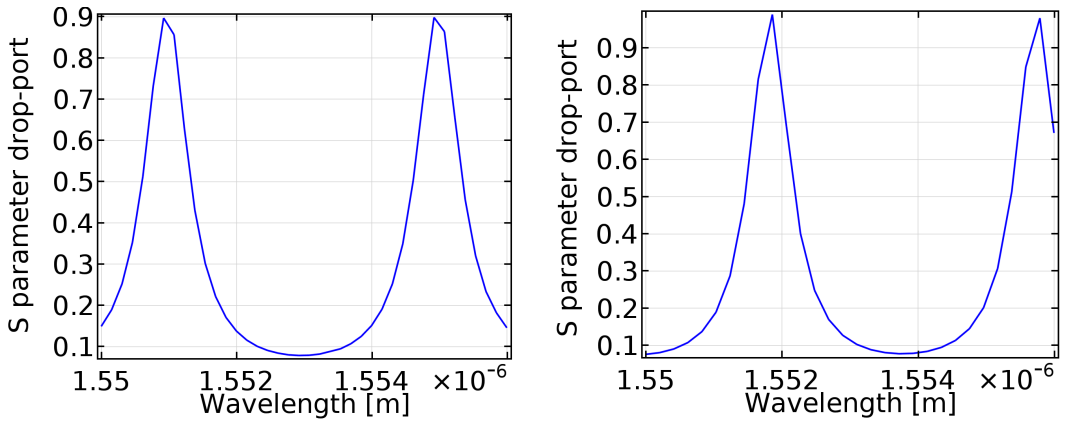


**Figure 30:** Transmittance on drop port of a resonator with a radius of $35\mu m$, (a) Using beam envelope method, (b) Using frequency domain.

The second resonator has a radius of $46.58\mu m$, which theoretically gives an FSR of 3.000 nm. The result from the simulation can be seen in table 2, and a plot of the S-parameter on the drop port can be seen in figure 31.

**Table 2:** Ring resonator critical values

| | |
|---|---|
| Radius | $46.85\mu m$ |
| FSR | 3.0508 nm |
| FWHM | 0.508 nm |

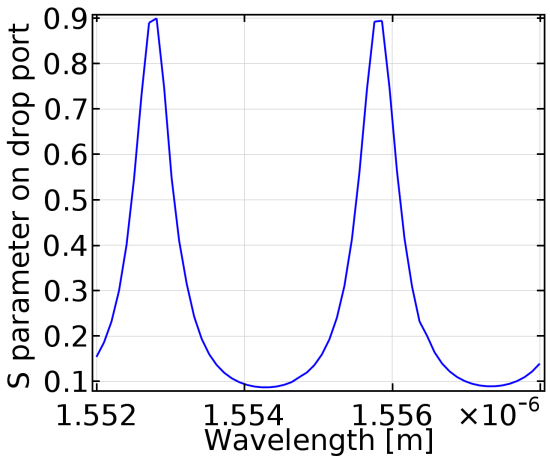


**Figure 31:** S parameter on drop port of a ring resonator with radius of $46.58\mu m$

## 5.6 Mach Zehnder

The MZI was only modeled using beam envelope as the previous models seem to be consistent both with theory and across physics interfaces. An illustration model with shorter arms can be seen in figure 32.

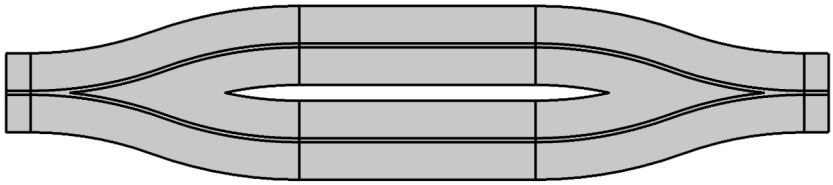

**Figure 32:** Shorter MZI model for illustration purposes.

The phase difference in the two arms is the observable. Physically this is induced by a change in refractive index in the cladding, which then alters the effective index of the core. To simulate this behaviour different cross sectional analysis are performed with different cladding materials. The first MZI models were made with arms of different lengths, and initially the length was set in the range of 3-5 mm. This is somewhat short for a MZI, but during basic functional testing it was favourable to reduce computation time. In the first models it was clear that there is some mode interference in both the splitting and the recombination sections, see figure 33.

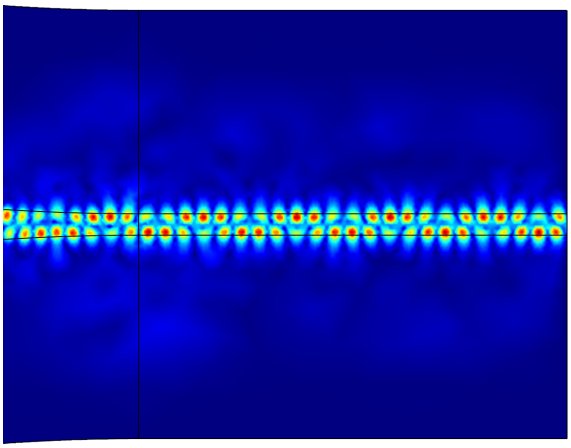

**Figure 33:** Electric field at the output waveguide after recombination in a MZI with multimode behaviour.

To rule out the the effect of the transition in mesh, the same model was built only with a 200 nm wide waveguide, which is known from previous tests to be truly singlemode. In

figure 34 one can see the S parameter on the output port as the index in the sensing arm is slowly increased with 0.004 RIU.

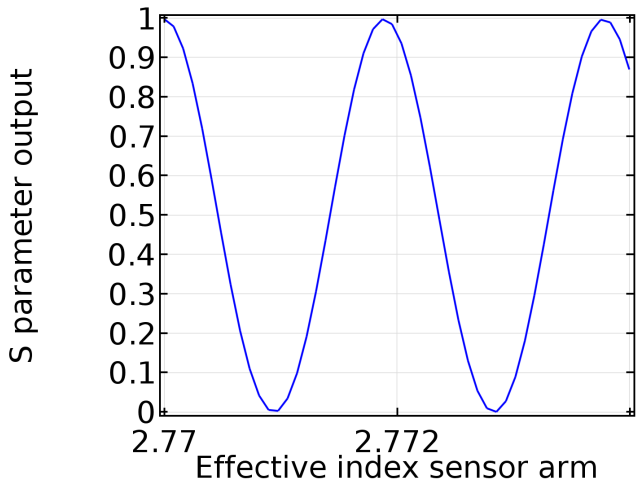


**Figure 34:** S-parameter of the output of a MZI with 200 nm wide waveguide, index in sensing arm is slowly increased with 0.004 RIU.

The smooth sinusoidal response consists well with theory and the field distribution in the core looks similar to example models supplied by COMSOL. In figure 35 the S parameter on the output port of the same MZI only with a 500 nm wide waveguide.

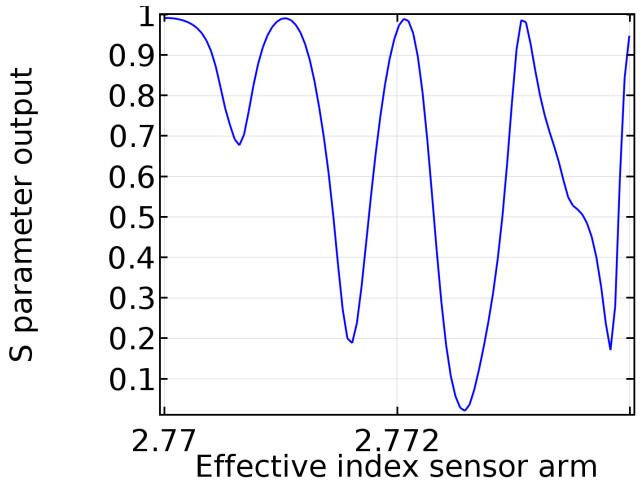


**Figure 35:** S-parameter of the output of a MZI with 500 nm wide waveguide, index in sensing arm is slowly increased with 0.004 RIU.

There is clearly some interference, which most likely comes from a multimode behaviour. The multimode field is correct from the 2D standpoint, and the solutions exists, but the only the single mode operation is interesting, as the physical waveguide has restrictions in the z plane. To overcome this, two solutions were tested. First a taper was made on the output, from 500 nm to 200 nm, the tapering occurs over $30\mu m$. This did improve the

output spectrum somewhat, but there are still some interference from higher order modes. The second attempt was to taper both MZI arms at the end, before the recombination, see figure 36.

**Figure 36:** Tapering from 500 nm to 200 nm on the arms of MZI before recombination and output.

After the mesh was refined in the area surrounding the core and towards the boundary and also defining the output port over a smaller area the MZI functioned properly. The S-parameter on the output of an example MZI with 5 mm long arms, and an index variation of 0.0005 RIU can be seen in figure 37.

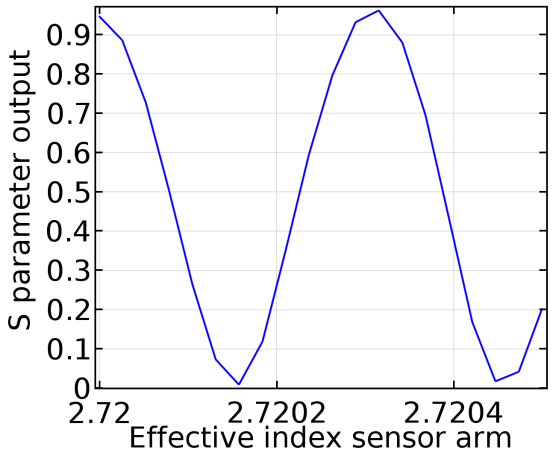


**Figure 37:** Sinusoidal response at the output of a 5 mm long MZI, effective index of sensing arm slowly increased with 0.0005 RIU.

The next step is to determine the $\text{FSR}_{MZI}$ of the sensor at rest. Both $\text{FSR}_{MZI}$ and the unknown parameter $\Delta n_g$ needs to be determined. In table 3 the values from the two simulation runs can be seen.

**Table 3:** Simulated values of two example MZI for determining $\text{FSR}_{MZI}$ and $\Delta n_g$

| | MZI I | MZI II |
|---|---|---|
| Length | 2.125 cm | 2.150 cm |
| FSR | 3.1795 nm | 2.9703 nm |
| $\Delta n_g$ | 0.0355 | 0.0376 |

There is a small difference in $\Delta n_g$ for the two sensors, and two other test runs with different length where done. Both of these produced values between 0.035 and 0.037. This is not critical as the $\text{FSR}_{MZI}$ was within acceptable values after two runs. It still was expected to have smaller variations, which would make it easier to estimate the length of the sensor with PDMS/Cryptophane. In figure 38 the periodic response of the two different MZI can be seen, both sensors have air as cladding on the sensor arm.

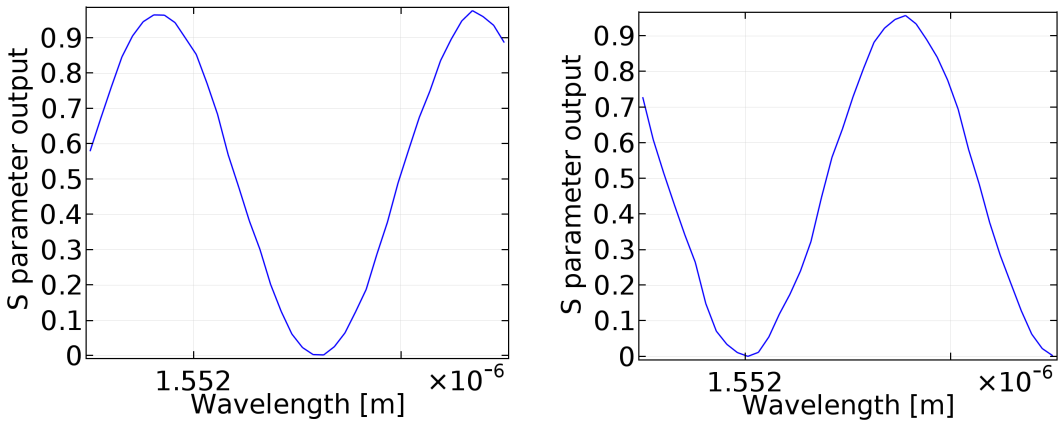


**Figure 38:** S parameter on output of two MZI with different length. Both sensors represent a MZI with air as cladding on the sensing arm, (a) Length of 2.125 cm, (b) Length of 2.15 cm.

## 5.7 Complete model

The parameters for the complete model can be seen in table 4. This model represents a ring resonator cascaded with a Mach Zehnder interferometer, and looks similar to the one shown in figure 17. The core is Si and the cladding covers everything except the sensor arm is $SiO_2$, in the sensor window the cladding is set as air.

**Table 4:** COMSOL model parameters.

| | |
|---|---|
| Ring length | $294.3\mu m$ |
| MZI arm length | 2.15 cm |
| Ring separation | 165 nm |
| $n_{eff}$ ring and reference arm | 2.72 |
| $n_{eff}$ sensor arm at rest | 2.74 |

The mesh was set as triangular in the curved sections, and a mapped mesh in the straight arms of the MZI. At the tapered sections and the output area the mesh was refined, as this is a critical area. The parametric sweep was initially set to iterate from 1500 nm to 1650 nm with the sensor at rest. In figure 39 one can see the output spectrum where one of the peak resonances is close to 1550 nm.

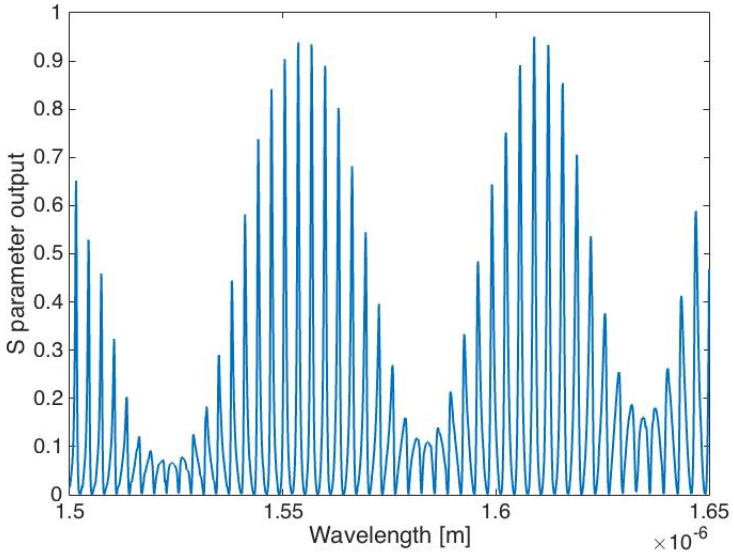


**Figure 39:** S parameter on output of complete model from a parametric sweep from 1500 nm to 1650 nm.

To determine the effective index change in the the complete model, a new modal analysis where performed. Two simulations where performed on the cross section and the index of the cladding was increased with $10^{-4}$ RIU on the second run. This resulted resulted in a change in effective index in the core of $1.132 \cdot 10^{-5}$ RIU. This value corresponds to the product $S_w \Delta n_c$ in equation 57. The resulting spectrum on the output with both $\Delta n_c = 10^{-4}$ and $\Delta n_c = 0$ can be seen in figure 40.

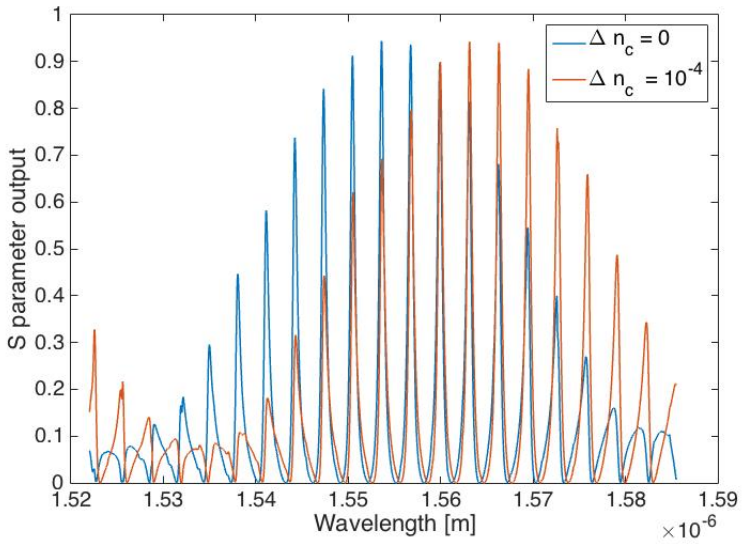


**Figure 40:** S parameter on output of complete model from a parametric sweep from 1520 nm to 1590 nm. Blue graph represents the response at $\Delta n_c = 0$, and orange represents $\Delta n_c = 10^{-4}$.

The shift in resonance is clearly visible, and calculated to be 9.495 nm using MATLAB. The sweep was done over a shorter interval, which improves the accuracy of the results as the approximations would not hold over a too wide range. The theoretical shift was calculated using equation 57 and the simulated values of $\text{FSR}_{MZI}$, $\text{FSR}_{filter}$, $n_g$ and the product $S_w \Delta n_c$. A comparison of the theoretical and simulated resonance shift can be seen in table 5.

**Table 5:** Comparison of theoretical and simulated resonance shift.

| | Theoretical | Simulated |
|---|---|---|
| $\Delta\lambda$ @ $n_c = 10^{-4}$ | 11.062 nm | 9.495 nm |

The simulated value is relatively close to the theoretical value, and deviates only by 1.567 nm. It is important to note that the simulations themselves are approximations, and the exported data from the simulations has a limited amount of data points.

In table 6 the limit of detection, waveguide sensitivity and overall sensitivity can be seen.

**Table 6:** Calculated figures of merit for a vernier enhanced MZI with air as cladding on the sensor arm.

| | |
|---|---|
| $S_w$ | 0.1132 |
| LOD | $2.75 \cdot 10^{-5}$ RIU |
| $S_{overall}$ | 110 $\mu m$/RIU |

When comparing these numbers to the theoretical work in [32, 15, 16, 18], this sensor is not as sensitive as some of the suggested designs. In this thesis considerable time has been put in to build functioning models in COMSOL, which provides results consistently, but it seems there is still some work of optimizing the sensor. One example is the gain factor dependency on ΔFSR, which can be seen in figure 41.

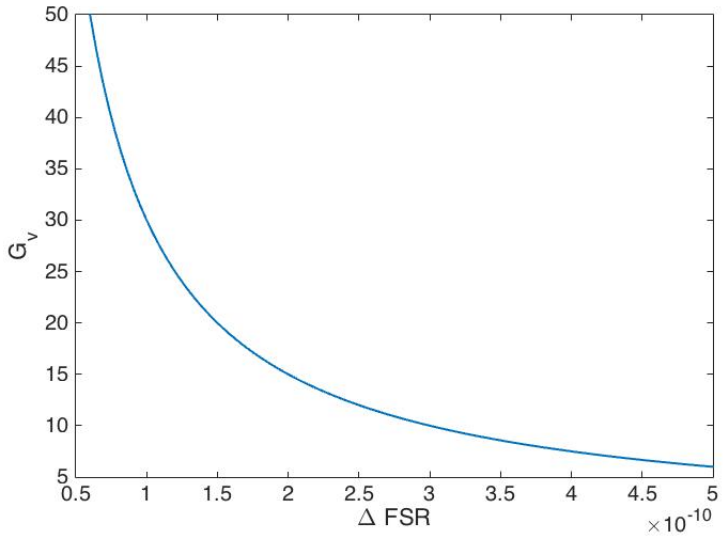


**Figure 41:** $G_v$ plotted with respect to ΔFSR.

The curve is exponentially decaying, and $G_v$ is extremely sensitive to small changes in ΔFSR. So this parameter needs to be optimized further to increase gain and decrease LOD. The waveguide sensitivity is lower than estimated previously, and could partly be due the simulations are performed in 2D. Other waveguide geometries should also be considered to improve the overall performance.

## 5.8 Sensor with PDMS cladding

After the results presented this far match the theory, the next step is to estimate the length of a MZI using a PDMS cladding on the sensing arm. This model, as the previous represents a sensor with a Si core and $SiO_2$ cladding. The effective index of the sensor arm was calculated as before, using the refractive index for PDMS w/cryptophane as cladding material, $n = 1.412$ from [28]. The MZI was set to 2 cm to first estimate $\Delta n_g$ from $\text{FSR}_{MZI}$, see figure 42 for a plot of the S parameter on the output.

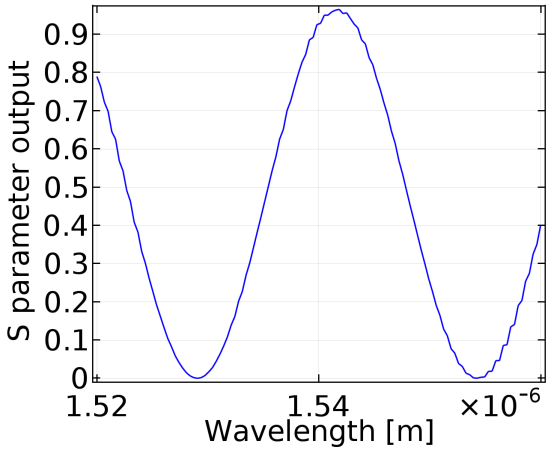


**Figure 42:** S parameter on output of MZI with PDMS/cryptophane on the sensing arm, result from a parametric sweep from 1520 nm to 1560 nm.

Simulated and estimated values resulting from the simulation can be seen in table 7.

**Table 7:** Simulated and estimated values for a 2 cm long MZI with PDMS cladding on the sensing arm.

| | |
|---|---|
| $\text{FSR}_{MZI}$ | 25.21 nm |
| $\Delta n_g$ | 0.0048 |

When calculating the length of a MZI with $\text{FSR}_{MZI} \approx 3$ nm using equation 50 and the estimated $\Delta n_g = 0.0048$, it results in an arm length of 16.8 cm. This is extremely long and even when considering a low loss photonic structure, it would still accumulate losses around 15 - 20 dB [33]. To decrease the length of the arms a larger difference in the refractive index between the cladding and polymer is needed. This will be discussed further in section 9.

If we now consider a suitable polymer and cladding producing the same refractive index contrast, as in the case of air and $SiO_2$, the specifications of a theoretical sensor can be derived. The sensor parameters can be seen in table 8. In these calculations the waveguide sensitivity in table 6 has been used. This value is lower than what has been reported in literature, and the sensor presented could potentially perform even better.

**Table 8:** Design parameters for the sensor with a methane sensitive polymer covering the sensor arm.

| | |
|---|---|
| Ring length | $294.3\mu m$ |
| MZI arm length | 2.13 cm |
| $\Delta n_g$ | 0.0376 |
| $\text{FSR}_{MZI}$ | 3.007 nm |
| $\text{FSR}_{ring}$ | 3.050 nm |
| $\Delta$FSR | $4.35 \cdot 10^{-11}$ |
| $S_w$ | 0.113 |
| $\Delta\lambda$ @ $n_c = 10^{-4}$ | 32.66 nm |
| LOD | $9.34 \cdot 10^{-6}$ RIU |
| $S_{overall}$ | 326 $\mu m$/RIU |

From [28] the change in refractive index of PDMS due to a 50 nM concentration of methane resulted in $\Delta n_c = 1.6 \cdot 10^{-4}$ RIU. If a suitable polymer would behave similarly with the right ratio of cryptophane, the sensor should detect changes in concentration of methane less than 50 nM.

# 6 Fabrication Method and Equipment

The manufacturing of the proposed sensor components was carried out in NTNU Nanolab. The goal is to fabricate the individual components to correct dimensions, and also couple light into the fabricated structures. This would hopefully substantiate the feasibility of producing a potential prototype at NTNU in the future. There are several process steps involved, and for each instrument there is some training required. In the following section the general method and steps will be described along with an introduction to the equipment. This section can be used as reference in section 8 which describes the processes on the individual samples in more detail. The general process flow can be seen in figure 43.

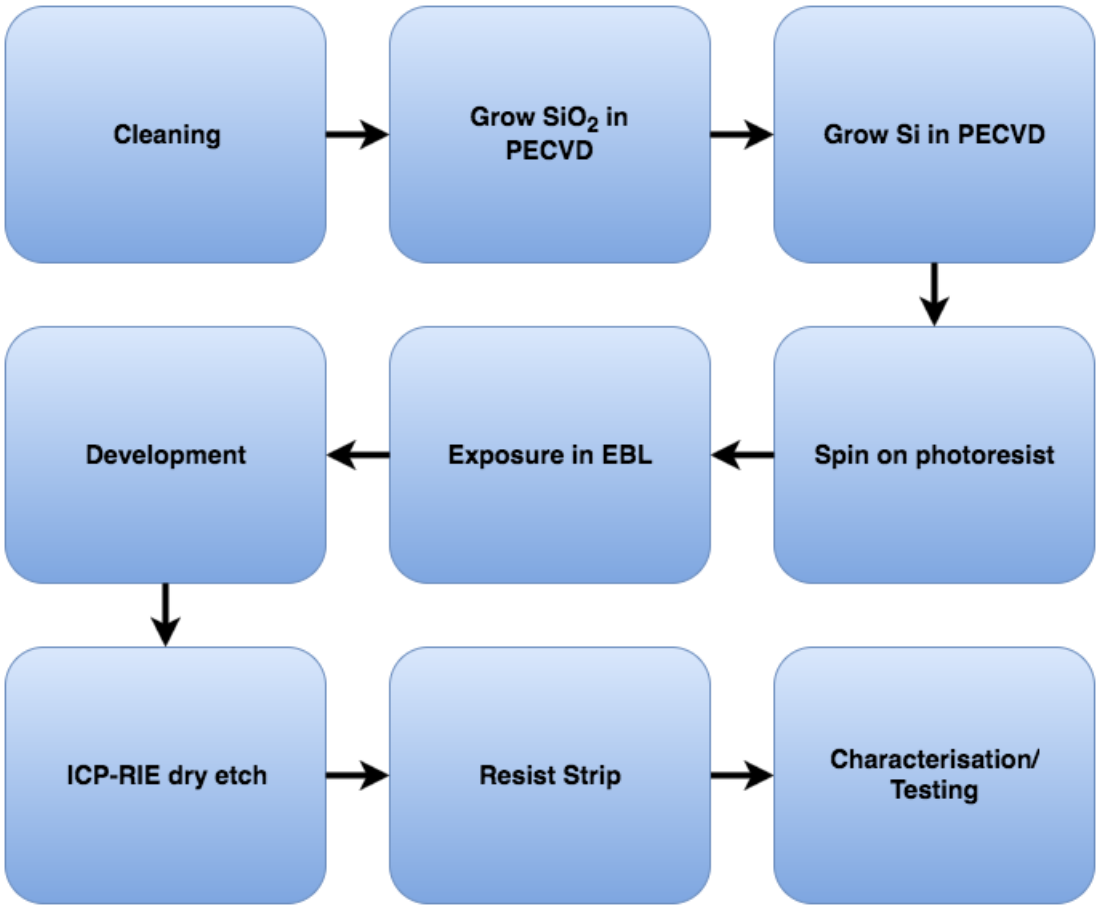


**Figure 43:** General process flow in Nanolab

The first full run through was done to be familiarized with the equipment. After this run-through a process-flow template was created, and used both as a guide and to note dose, process time etc. during processing.

## 6.1 Scriber

The scriber tool is used to cut smaller samples from wafers. It is a automated cut and break tool that uses a diamond tip to make a grove about 5 um thick. The wafer or smaller sample is put on an adhesive tape which is held in place by a pair of interlocking rings. These rings are placed on a holder in the scriber, where it is held in place by a vacuum. After the scribe line is made, an anvil applies a force which breaks the wafer along the sribe line. Figure 44 illustrates the set up.

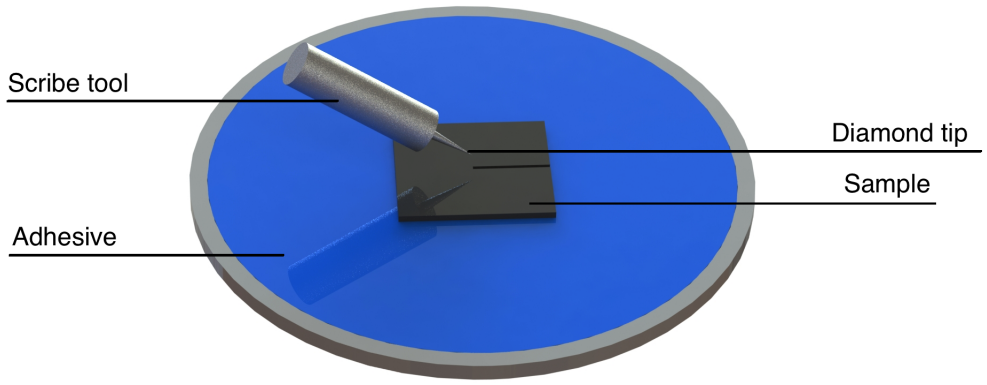


**Figure 44:** Illustration of the scriber tool, the blue adhesive tape holds the sample in place as the scribe tip moves across the sample.

There are two settings, automated scribe and break which is used to cut smaller dies from a wafer. While the other setting is called interactive mode, this is used when cutting smaller samples for analysis in the scanning electron microscope (SEM), or preparing the sample for testing in the optics lab.

There are some difficulties when using the scriber, especially when cutting and breaking samples with waveguide structures. The scriber tip roughens up the area where it is in contact with the sample, effectively ruining the structure for both analysis in the SEM, and making it near impossible to couple light into it without polishing. This is why the samples containing structures are only scribed a short distance, then the anvil is used to break the sample along the crystal axis, effectively using the short scribe line as a "guide". There is a possibility that this break line will not be perfectly straight, which can potentially ruin the sample for testing in the optics lab.

In both the scribing and breaking process there will be a lot of Si dust which adheres to the sample surface. To avoid this, the scribing is done before the final resist layer is removed. The dust is caught in this layer which is sacrificial and removed before testing.

## 6.2 PECVD

PEVCD is the abbreviation for plasma enhanced chemical vapor deposition, and is a technique used to deposit thin uniform films. The advantage of PECVD is the ability to do deposition at lower operating temperatures compared to a conventional CVD reactor. The thin-films has good adhesion, high film density and a high deposition rate [3]. The reactor in nanolab is from Oxford Instruments and is operating at a pressure around 0.5-2 Torr with a selectable temperature range. In figure 45 and illustration of the reaction chamber can be seen.

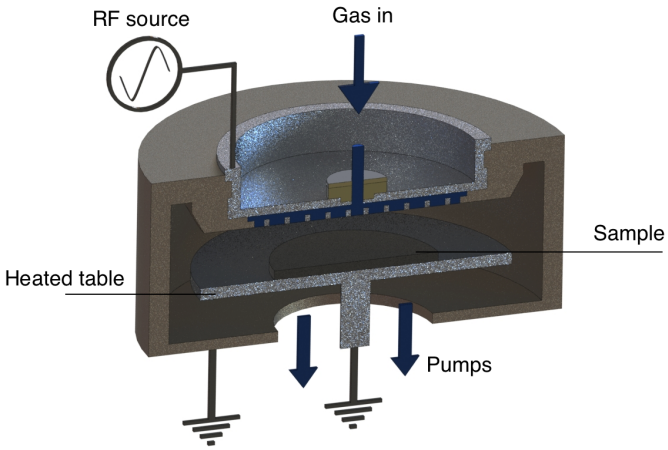


**Figure 45:** Illustration of the Oxford PECVD reactor, based on schematic from Oxford Instruments

After the reactants are introduced through the gas inlet, the RF source generates the plasma. The frequency of the RF source in this reactor is 13.56MHz which is one of the industry standards. After the plasma is lit, the dissociate molecules move to the sample surface where they are absorbed and form the thin uniform layer. The byproducts of the reaction is then removed by the pumping system. The reactions that take place at the surface are complex and dependent on factors as the composition of reaction gases, temperature and pressure.

In the process of growing $SiO_2$ the silane gas is diluted in nitrogen and reacts with nitrous oxide on the surface to form the oxide layer. The reaction can be described by [3] :

$$\mathrm{SiH_4\,(gas)} \;+\; 2\,\mathrm{N_2O\,(gas)} \;\rightarrow\; \mathrm{SiO_2\,(solid)} \;+ 2\,\mathrm{N_2\,(gas)} \;+\; 2\,\mathrm{H_2\,(gas)} \qquad (60)$$

The $SiO_2$ film is not necessary stoichiometric and can contain traces of both hydrogen and nitrogen [3]. As the main role of this oxide layer is to act as an insulating layer between

the top and bottom Si layers this is not seen problematic. Still it should be taken into consideration that the bulk refractive index of the oxide is affected by the hydrogen and nitrogen content. The same oxide layer is also used as cladding material, event though it mainly act as a protection layer, it could have an impact on the effective refractive index.

The amorphous Si (a−Si) layer is also grown in the PECVD. The optical properties of a−Si has been researched since the start of micro electronics, photonics and photovoltaics [34]. Loss in optical waveguides are as mentioned in previous sections due to scattering and absorption. As a−Si is disordered compared to crystalline Si, it can be described as a continuous random network (CRN). In such cases there is a short range order similar to the crystalline form, typically in the order of 2 nm. In the a−Si CRN there is a high degree of defects in the form of dangling bonds, where the Si has too few bonds to fill its outer shell. These dangling bonds degrade the optical conductivity. When hydrogen is introduced in the process it passivate defects, thus lowering the optical losses [34, 35].

When operating the reactor, the process starts by placing the sample in the loadlock chamber. This chamber is under vacuum and needs to be pumped to atmospheric pressure before it is opened. After the sample is placed on a suitable carrier wafer inside the the chamber, the loadlock is evacuated. The next step is to load a recipe, which decides the different gas flows and process temperatures. The sample is then transported to the reaction chamber by a rail system. It is crucial to include several pump and purge steps with nitrogen in all recipes. These steps should come after the deposition process to ensure that none of the process gases are left in the chamber and carried back to the loadlock. Silane gas can auto-ignite in contact with air or form explosive mixtures. Several of the other process gases used are also toxic. In addition this step also minimizes chamber contamination between different runs where different gases and sample materials are used. The recipe used for growing $SiO_2$ and Si is shown in table 9 and 10.

**Table 9:** PECVD $SiO_2$ recipe

| | |
|---|---|
| RF Power | 20W @ 13.56MHz |
| Pressure | 1000mTorr |
| Table Heater | 300°C |
| Chiller | 20°C |
| $SiH_4$ | 8.5 sccm |
| $N_2O$ | 708 sccm |
| $N_2$ | 161 sccm |

**Table 10:** PECVD amorphous Si recipe

| | |
|---|---|
| LF Power | 200 W |
| Pressure | 500 mTorr |
| Table Heater | 300°C |
| Chiller | 20°C |
| $SiH_4$ | 50 sccm |
| Ar | 150 sccm |

## 6.3 Reflectometer

The reflectometer in Nanolab is a Filmetrics F20 and is used to measure the thickness of thin-films. It is an easy to use instrument which uses light to determine the thickness, roughness and optical constants of a thin-film [2].


**Figure 46:** Filmetrics F20 for measuring thickness of thin-films [2].

The reflectance from the background, a reference and the sample are measured, and from these measurements the film thickness is approximated. A goodness of fit parameter (g) is a number between 0 and 1 which describes how good the result matches the mathematical model. Films with multiple layers like the SOI platforms made in this thesis have been hard to measure exactly. It still gives a good approximation and for single films on crystalline Si the goodness of fit has been between 0.98-0.99. The range of the F20 is from 1 nm to 10 mm thick films, with a typical accuracy of a few angstroms [2].

## 6.4 Spin coater

Spin coating is a technique used to evenly distribute e.g polymer solutions like photoresist on a surface. An illustration of a spin coater can be seen in figure 47. The vacuum chuck holds the sample in place, and the resist is dispensed on the sample using a pipette or dispenser. A protective lid is closed and the rotation starts.

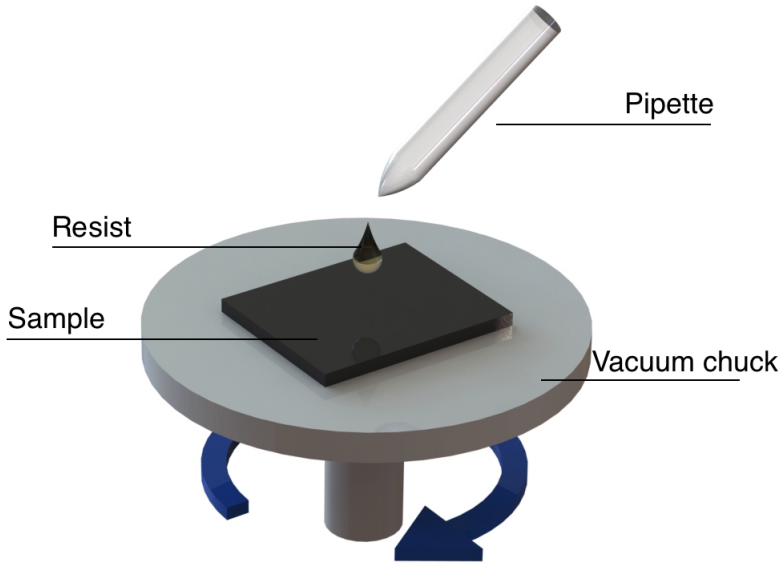


**Figure 47:** Illustration of a spin coating system, vacuum chuck in white with a sample and pipette.

The thickness of the film is highly dependent on the spin speed, and the thickness is typically exponentially decaying with increasing spin speed. The spin curve for the CSAR 62 (AR-P 6200.13) positive photoresist can be seen in figure 48. The spinner table in Nanolab has three settings; spin speed, acceleration and spin time. After the resist is spun on the sample is put on a hot plate to soft bake it. This process removes most of the solvents from the resist, it improves the adhesion and also hardens it before the exposure sequence [30]. The temperature and time for the soft bake depends on the individual resist and should be found in the datasheet.

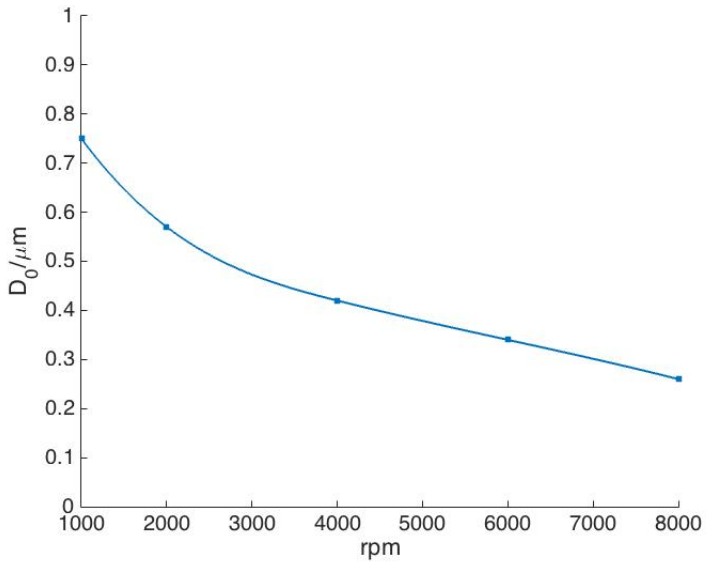


**Figure 48:** Relation between thickness and spin speed for AR-P 6200.13

## 6.5 Electron beam lithography

Electron beam lithography (EBL) is the continuation of conventional UV lithography. As resolution is proportional to wavelength, and electrons have considerably shorter wavelength than UV radiation, the EBL system is capable of producing much finer structures. The main issue with EBL is that compared to UV lithography it is extremely slow. In commercial production it is mainly used to produce the masks for the UV systems. The EBL system used in this master thesis is a Elionix ELS-G100, and was installed and operational february 2016. At 100kV and 100pA the beam diameter is 1.8 nm.


**Figure 49:** Elionix ELS-G100 system

Before loading the sample into the EBL, the beam current should be set according to the desired beam spot. The system has some hysteresis and the needs some time to stabilize if the current is altered. The next step is to load the sample, as the EBL system is somewhat fragile this process has to be done with care. After the sample has been loaded and the beam current has stabilized, the system is ready for calibration. The exact current is measured using a Faraday cup and taken note of, this is necessary when calculating an accurate dosage. The beam is then focused and adjusted for astigmatism. This can be done manually or by assistance of the auto focus/astigmatism function in the Elionix software. When this is satisfactory it is wise to put on the beam blanker while doing the rest of the pre-exposure sequence to avoid damaging the reference plate.

The EBL masks can be drawn in several different software, in this thesis CleWin has been used. In figure 50 an example mask of a notch filter drawn in CleWin can be seen. There are some limitations using CleWin, especially when drawing circular shapes and saving to GDSII format, as it converts all shapes to polygons.

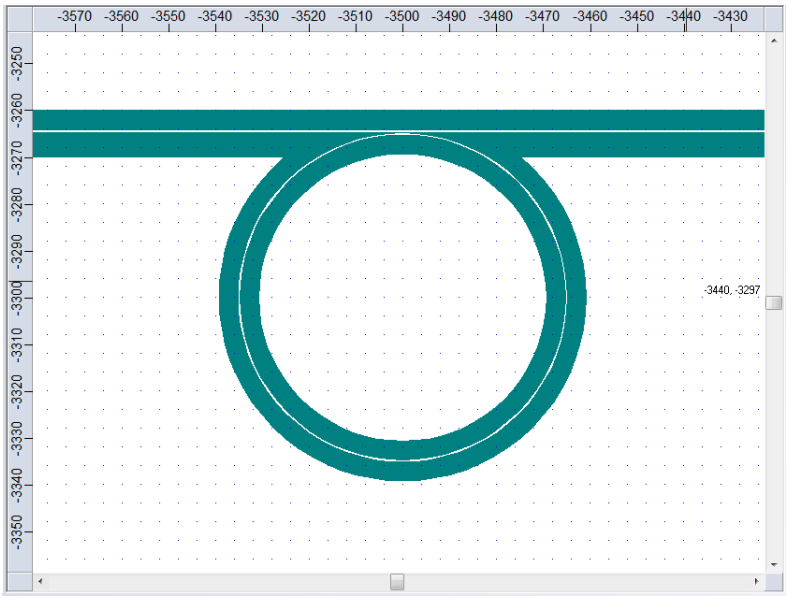


**Figure 50:** Notch filter drawn in CleWin.

After the mask has been imported into the Elionix software the next step is to assign write fields. The size of the write field determines the beam step size and has to be taken into account when evaluating the smallest features of the design. Because there are multiple write fields these have to be aligned when the stage moves, this process can cause stitching errors as seen in figure 51.

**Table 11:** Beam step size and field size, units are in nm

| Dots | $100\mu m$ | $250\mu m$ | $500\mu m$ | $1000\mu m$ |
|---|---|---|---|---|
| 50,000 | 2 | 5 | 10 | 20 |
| 200,000 | 0.5 | 1.25 | 2.5 | 5 |
| 500,000 | 0.2 | 0.5 | 1 | 2 |
| 1,000,000 | 0.1 | 0.25 | 0.5 | 1 |

The next step is to calculate the dose. If the dose is too low, it can cause under-exposure and in the developing phase some resist may still be present on the sample. A too high dose is called over exposure, this is harder to discover but can lead to pattern deformations

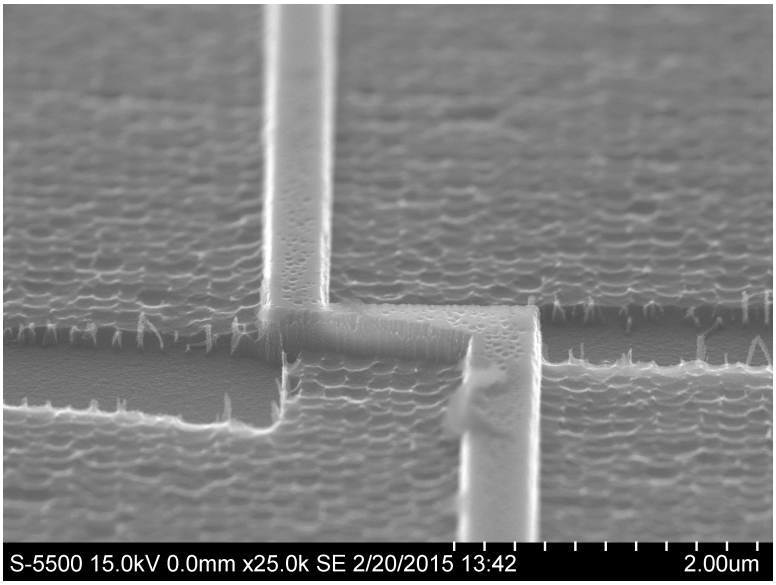


**Figure 51:** Stitching error due to write field alignment, courtesy of Jens Høvik.

in later processes.

After the dosage has been calculated and assigned to the pattern, the mask needs to be aligned according to where the sample is placed in the sample holder. After the alignment the sample inclination is measured using a laser which is fitted to the stage. It is recommended by the manufacturer to remove and clean the bottom of the sample if the inclination is larger than 1 mrad. If the sample is not level the focus will be off, resulting in worse resolution. When all these parameters are within optimal range, the rest of the process is automated. First of the software adjusts to avoid stitching errors using a function called field correction, after this is within acceptable values the exposure sequence can begin.

After exposure the sample is removed and brought to the development bench. Here the sample is developed using ARP 600-546 for 1 min, then put in IPA to stop the development process. In the development phase there are some of the same issues as when exposing, called over- or underdevelopment. The developer used, ARP 600-546, is a relatively mild, and the reaction rate with unexposed resist is so slow that the sample can lay in the solution for far longer than 1 min before the unexposed resist is attacked. Finally the sample is rinsed in DI water. No post exposure bakes were done, this can lead to resist re-flow, but according to the data sheet the resist can be post baked. The sample is then ready for the etching step.

## 6.6 ICP - RIE

Inductively coupled plasma reactive ion etch (ICP-RIE) is a dry etching technique which produces highly anisotropic etches. The process is part chemical and part physical. In figure 52 an illustration of both physical and chemical etching can be seen.

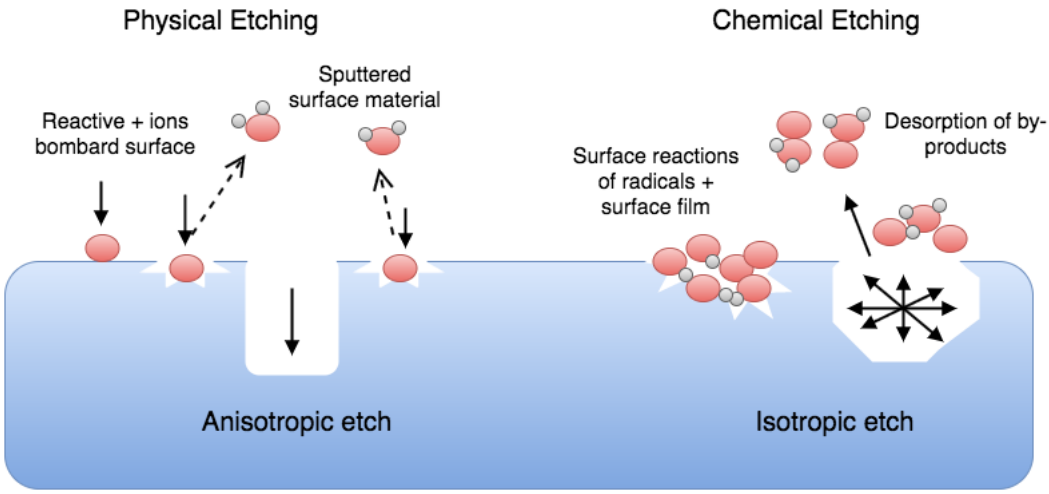


**Figure 52:** Illustration of chemical and physical dry etch mechanisms [3].

The reaction is dependent on process gases, temperature and sample material. The reactor itself is very similar to the PECVD and also produced by Oxford Instruments, name of the model is PlasmaLab System 100 ICP-RIE 180. The ICP-RIE uses a combination of inductively coupled plasma (ICP) and capacitive coupled plasma (CCP), see figure 53. The CCP power is often referred to the forward power, and responsible for driving the ions towards the substrate, while the ICP power controls the ion density [4].

This combination gives good control over the ion density without altering the energy of the ions that reach the substrate. The reaction gases used to etch Si is $SF_6$ and $CHF_3$, the ratio of these gases have a great influence on rate, anisotropy etc. The organic compound $CHF_3$ deposits a polymer layer on the sidewalls and surfaces. As the fluorine molecules are directional, i.e. hits close to perpendicular to the surface, they will not interact as strong with sidewalls. This results in sputtering of the polymer in the bottom of trenches and on flat surfaces, while leaving the sidewall polymer intact [36, 37]. The F radicals then react with the exposed Si and form $SiF_4$ which is removed. The selectivity of the etch is often an important parameter when the underlying layer has to be protected. In this thesis the resist layer is sufficient as a protective mask. The etch rate in a$-$Si is high, but the etch time is so short that there is no need for an additional protective layer. The etch recipe can be seen in table 12.

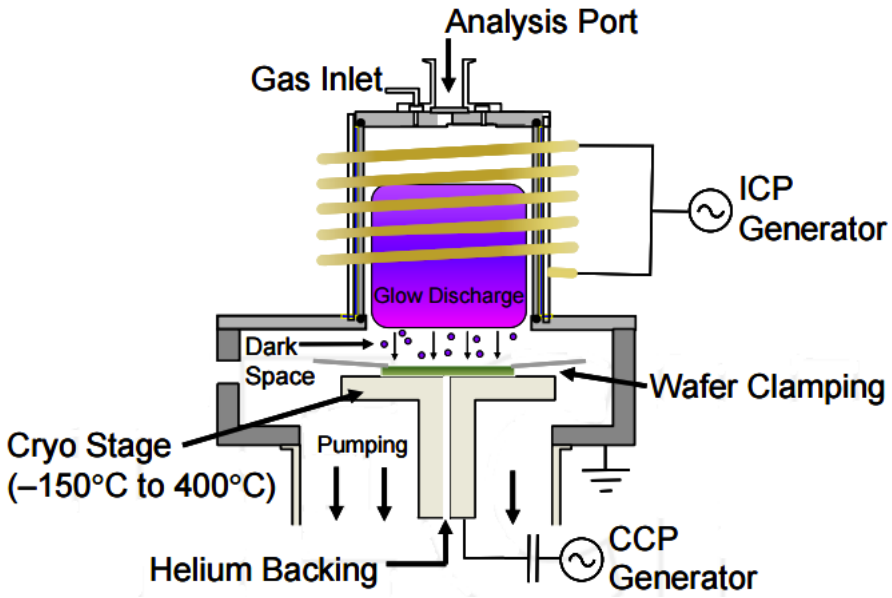


**Figure 53:** Illustration of ICP-RIE reactor [4].

**Table 12:** PECVD amorphous Si recipe

| | |
|---|---|
| CCP Power | 40 W |
| ICP Power | 600 W |
| Pressure | 15 mTorr |
| Temperature | 20°C |
| $SF_6$ | 7.5 sccm |
| $CHF_3$ | 50.0 sccm |
| Helium Backing | 10 mTorr |

## 6.7 S(T)EM

Scanning tunneling electron microscopy (S(T)EM) is one of the characterisation techniques available in Nanolab. The microscope is a Hitachi S-5500, a in-lens cold field emission electron microscope. As mentioned in section (EBL) the use of electrons in microscopy makes it possible to examine nano-sized structures, which is not be possible using conventional optical microscopes. With the S-5500 it is possible to achieve resolutions down to 0.4 nm. This is the best possible resolution and dependent on several factors e.g. the sample material. The S-5500 in Nanolab is a S(T)EM microscope, and it is possible to operate it as a transmission electron microscope (TEM), this feature has not been used in this thesis, so the focus of this section is SEM. When the electrons from the primary beam hit the surface, they react with the sample in a variety of ways in what is called the interaction volume. In the figure 54 a selection of reactions between the incident electron beam and sample can be seen [38].

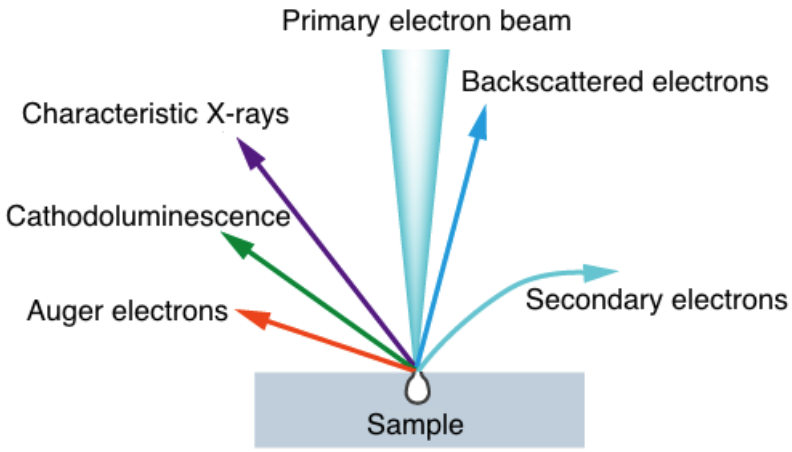


**Figure 54:** Illustration of the interaction volume and electron beam - sample interactions [5]

The secondary electrons (SE), backscattered electrons (BSE) and X-rays (EDX) are all possible to detect in the S-5500. The different electrons and photons carry information of the samples composition and surface topology. SE are generated when the incident electron excites an electron from the sample, the excited electron can usually escape very close to the sample surface if it has sufficient energy [38]. This is why the SE mainly carry information of the surface topology. BSE are the scattered electrons from the incoming beam, the scattering from an area is dependent on the atomic number. As the BSE signal from heavier elements will have a higher intensity they give information of sample composition. Both the BSE and SE can be detected simultaneously to create composite images which contain information on both topology and the materials. EDX is a more accurate way to determine the composition and is based on the X-ray emission.

# 7 Optical test setup

An illustration of the setup in the optics lab can be seen in figure 55. The schematic is courtesy of Idunn Knainn who has been working on the setup with Jens Høvik.

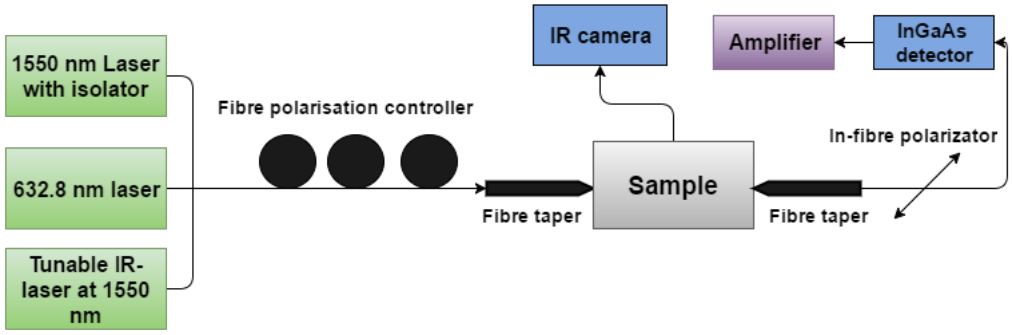


**Figure 55:** Optical test setup, courtesy of Idunn Knain.

To couple the light into a input waveguide, the sample and fibers needs to be perfectly aligned. There is a microscope mounted over the area where the fiber meets the sample. By using micrometer screws on the translational stage together with the microscope, it is possible to align the fiber tips with the waveguide input. During the alignment it is relatively easy to crash the tip into the sample. This could degrade the tip, which will cause the light to scatter and not be coupled into the waveguide. So extra care should be taken in this step. To align the height of the tip, another screw on the stage is adjusted until both tip and sample are in focus. If there is no sign of a signal on the detector, the height is slightly adjusted and the the output of the detector is checked again. If a signal is detected the IR camera can be used for confirmation, since light exiting the waveguide will be clearly visible.

# 8 Fabrication and Results

This section describes the processing of the different samples, an overview of the process flow used on the 550$\mu$m thick Si samples can be seen in figure 56. The samples were named A1-A4, B1-B4, C1-C4 and D1-D4. This corresponds to the placing in the sample holder used in Nanolab.

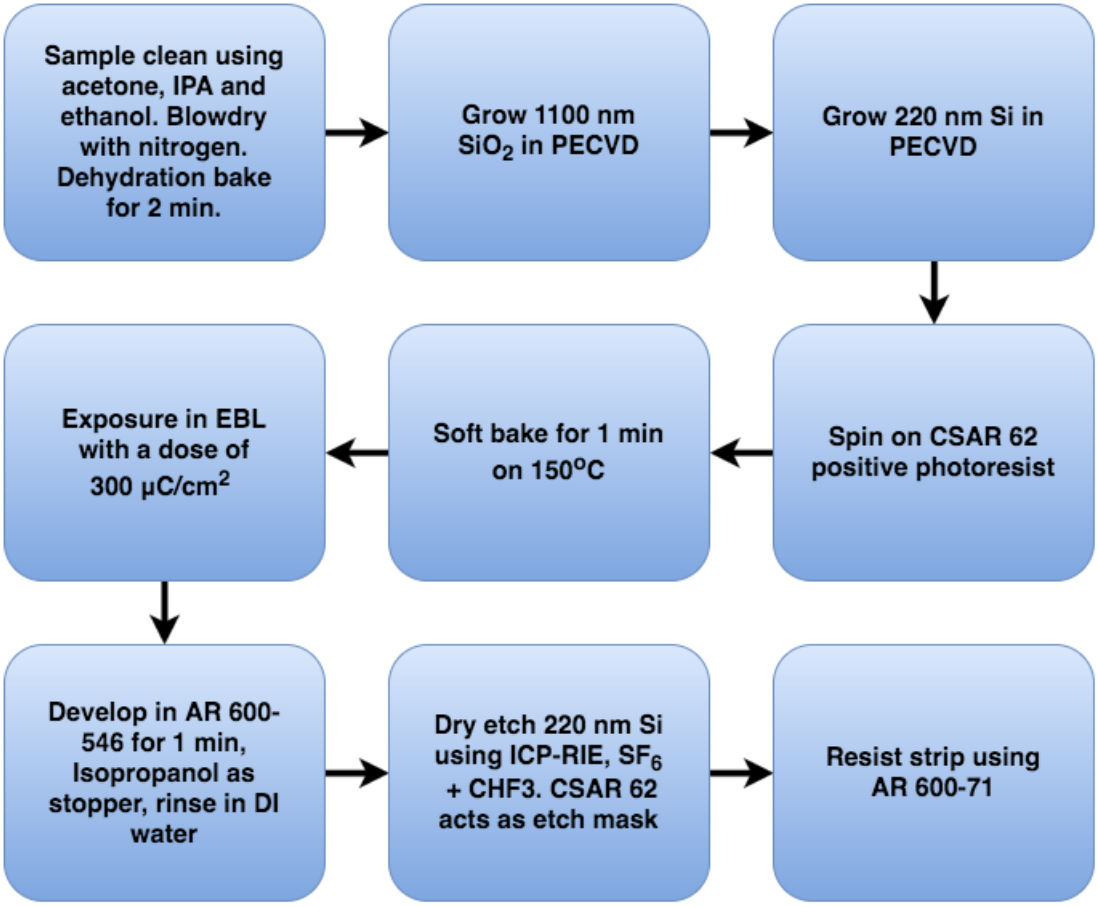


**Figure 56:** Process flow for fabricating photonic components on an SOI platform.

Half of the wafer was first cut into 15x15mm dies using an automated scribe and break program, the samples where then cleaned and ready for further processing. The next step to fabricate the SOI platform is to use PECVD to deposit both the $SiO_2$ and Si layers. There are factors which affect the PECVD grown film besides temperature, pressure ect. One of the important quality parameters is the roughness of the deposited oxide layer. As this influences the roughness of the next Si layer, which could increase the propagation losses in the waveguide. In the worst case prevent the coupling of light entirely. The surface roughness of the oxide layer was measured using AFM, and performed by Ane Tefre Eide on the behalf of Lars G. Holmen. The measurements showed a RMS value of approximately 5 nm with peaks as high as 30nm for the PECVD grown oxide. This is high compared to thermally grown oxide which has a surface roughness close to 0.1 nm. AFM images from the scans can be seen in figure 57 and 58.

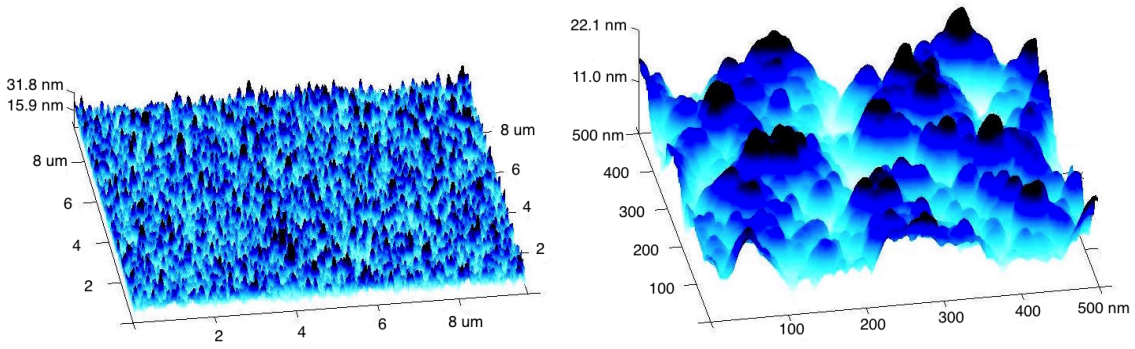


**Figure 57:** AFM image showing the surface roughness of a $SiO_2$ film grown using PECVD. Images courtesy of Ane Tefre Eide and Lars G. Holmen.

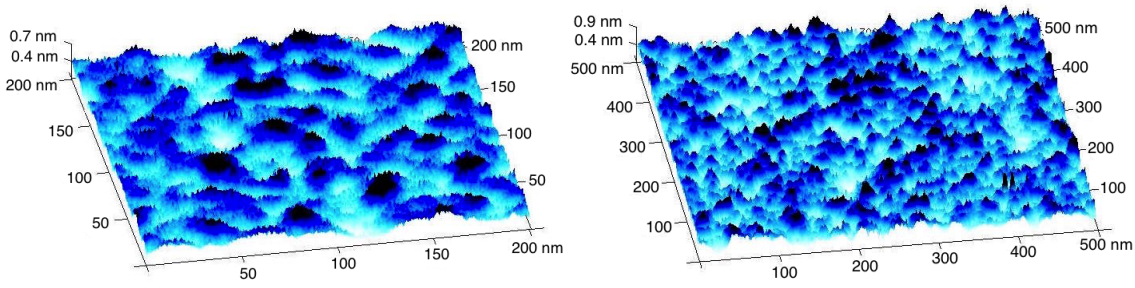


**Figure 58:** AFM image showing the surface roughness of $SiO_2$ film made by thermal oxidation. Images courtesy of Ane Tefre Eide and Lars G. Holmen.

To determine the deposition rate of the PECVD oxide a blank Si sample was used for 4 consecutive runs. The results from these runs can be seen in table 13.

**Table 13:** PECVD runs to determine growth rate of $SiO_2$

| | Time | Thickness |
|---|---|---|
| Run 1 | 3 min | 320 nm |
| Run 2 | 5 min | 531 nm |
| Run 3 | 10 min | 751 nm |
| Run 4 | 15 min | 1117 nm |

To grow a film thicker than $1\mu m$, 15 min run time was chosen. This gave films with a consistent thickness around 1110 nm. A film thicker than $1\mu m$ is considered to be of sufficient thickness so the light does not couple into the underlying substrate when exciting TE modes [39].

There are other considerations to be made when growing the amorphous Si in the PECVD. The carrier wafer should be a clean Si wafer, this is due to the low frequency plasma used in the process. If the carrier is e.g. $SiO_2$ which is an insulator, the contact between cathode and anode will be degraded when operating so close to the DC-point. In figure 59 the result of using wrong carrier can be seen, the Si is adhering to the surface, but the coalescence is random and the oxide layer is not usable.

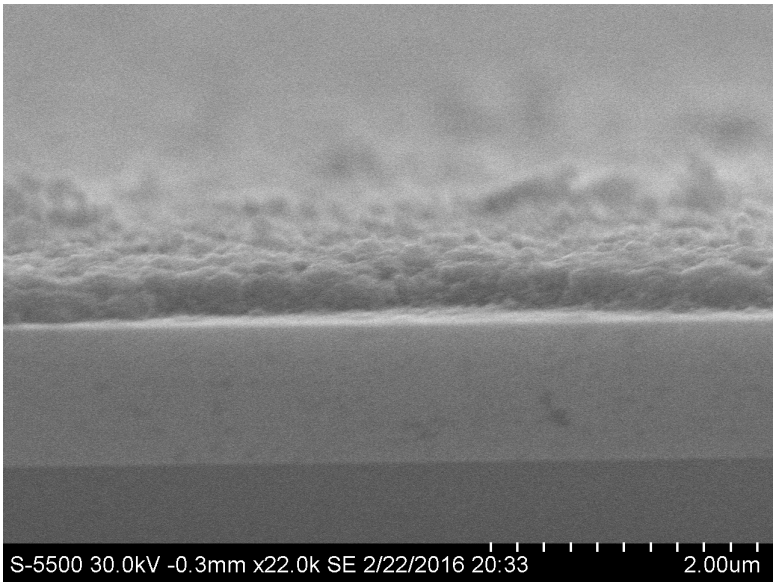


**Figure 59:** S(T)EM image of a PECVD grown Si film using a $SiO_2$ carrier wafer, the Si has randomly coalesced and is unusable. Image courtesy of Jens Høvik.

After both the oxide and silicon layers have been deposited, the next step is to spin on the EBL resist. After the resist has spread uniformly on the sample, it is soft baked for 1 min on $150°$C to harden the resist. This ensures the resist cant flow and spread unevenly during handling. The resist film thickness was measured by spinning the resist on a blank crystalline Si sample with no previous processing. The reflectometer was then used to approximate the thickness. The resist layer was measured to be 457nm with a goodness of fit of 0.99, the spinner recipe used can be seen in table 14.

**Table 14:** CSAR62 spinner recipe

| | |
|---|---|
| Spin speed | 4000 RPM |
| Acceleration | 500 |
| Time | 60s |

The etching rate of the resist had not been measured. However if the resist layer is deemed too thin it would be picked up on in the first test sample. Jens Høvik who have used the CSAR62 and etching recipe in table 12 reported no problems with the thickness either.

## 8.1 Sample A1

The structures on the first sample were an array of ring resonators with no coupling waveguides. This sample was partly processed to be familiarized with the equipment in Nanolab. The process steps and other parameters used on sample A1 can be seen in table 15. The cleaning step has been omitted from the table, but sample cleaning is performed between PECVD processes and before spinning on the resist. If the sample is cleaned with solvents after the resist is depositet, there is a chance this can affect the resist negatively and degrade patterns.

**Table 15:** Process overview sample A1

| | |
|---|---|
| **PECVD $SiO_2$** | Recipe from table 9, 15 min |
| **PECVD Si** | Recipe from table 10, 30 s |
| **Spin on CSAR 62** | Recipe from table 14 |
| **EBL** | Exposure-dose: $300\mu C/cm^2$ |
| **Development** | AR 600-546, 1 min |
| **ICP-RIE** | Recipe from table 12, 30 s |
| **Resist Strip** | Acetone, 5 min in sonic bath |

After the resist development phase, the structures were inspected using an optical microscope before the ICP-RIE step. Four of the ring resonators can be seen in figure 60.

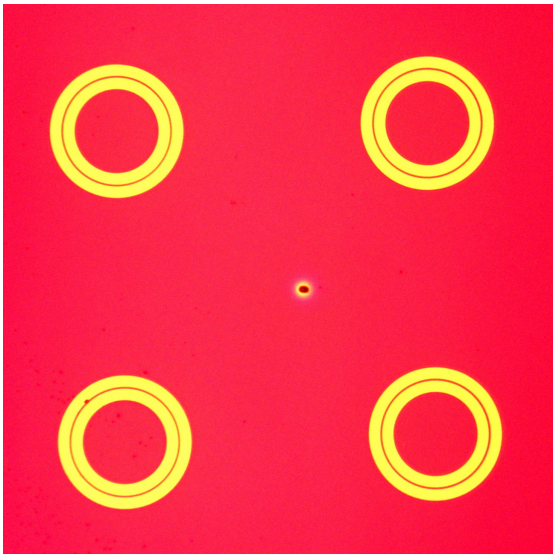

**Figure 60:** Four of the ring resonators in the ring array. Exposed Si is yellow and the CSAR 62 is seen as pink.

The yellow area is the exposed Si which will be etched in the RIE step, the pink is the resist which acts as an etch mask. One can clearly see some residue on the waveguide in the bottom-left ring, this is either from the exposure phase, or the solution has not been sufficiently agitated during development. As these rings and waveguides primarily were made for S(T)EM inspection this is not critical. It was still taken into consideration when processing the rest of the samples.

After the dry etch the resist was removed before the scribing process. This led to excess Si dust on the sample which is undesirable. The stripper from the manufacturer (AR 600-71) was not available at the time, so the sample was put in acetone and the beaker was placed in a sonic bath for five minutes. After the first round in acetone there was clearly resist left on the sample, so the sample was put back for two more runs of five minutes. After the last run, one could not see traces of resist residue in the optical microscope, so the sample was made ready for S(T)EM. Here it is clear some process parameters are not optimal. The etch was most likely too short, and it is likely that there are some resist and dust left on the surface.

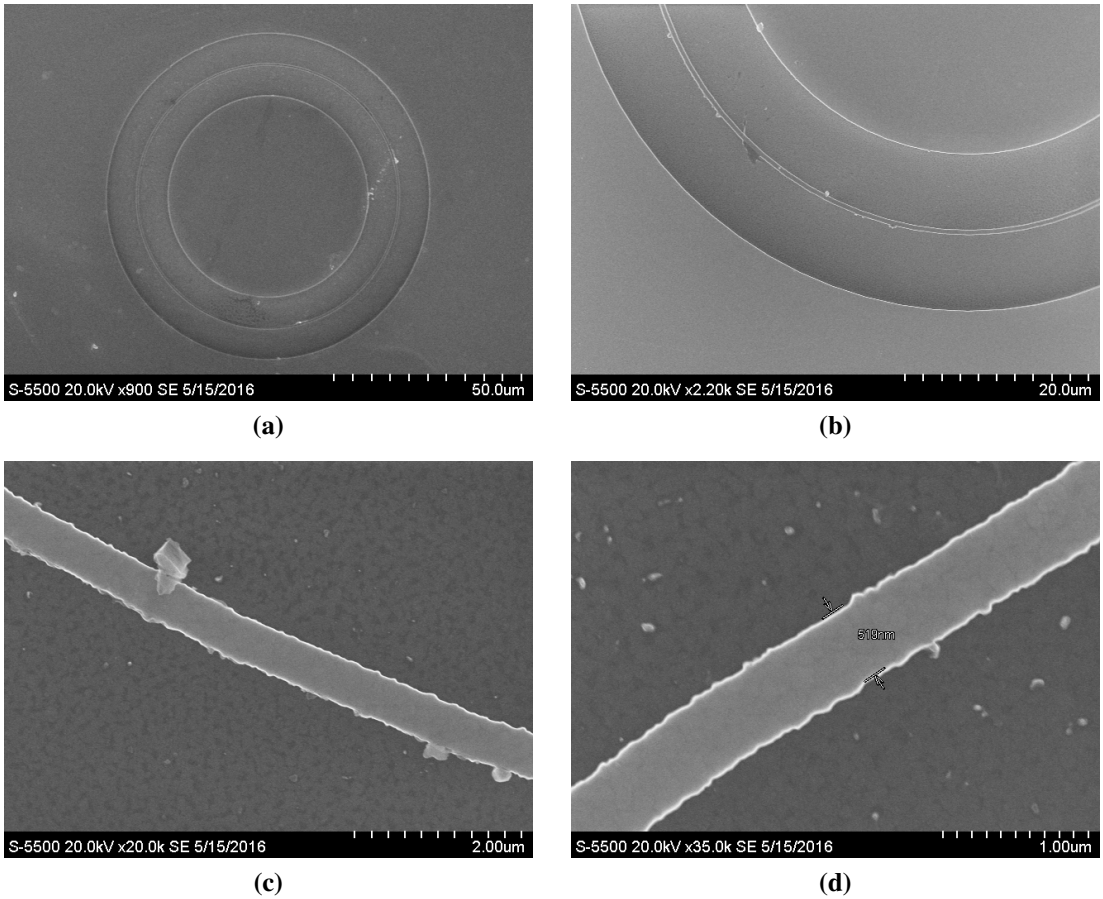


**(a)** **(b)** **(c)** **(d)**

**Figure 61:** Ring resonator structure which is part of an array of rings. The structure is made in amorphous Si on $SiO_2$ deposited using PECVD. Particles and excess photoresist can clearly be seen on parts of the ring.

The Roughness along the edges of the waveguide seen in figure 61 is partly due to using a $Al_2O_3$ carrier wafer in the ICP-RIE process. The organic polymer does not react the same way with the inert $Al_2O_3$, but react strongly with the small Si sample. Leading to the wrong ratio of polymer deposition to fluorine radicals, and the result is an irregular etch. Some of the particles seen are either dust or excess photoresist. The width of the waveguides was measured to be 519 nm, but as the sidewalls are so uneven there is some uncertainty to this measurement.

## 8.2 Sample B1

The second sample consisted of 20 closely spaced waveguides and five MZI's, this sample was meant for testing in the optics lab. The process overview can be seen in table 16.

**Table 16:** Process overview sample B1

| | |
|---|---|
| **PECVD $SiO_2$** | Recipe from table 9, 15 min |
| **PECVD Si** | Recipe from table 10, 35 s |
| **Spin on CSAR 62** | Recipe from table 17 |
| **EBL** | Exposure-dose: $300\mu C/cm^2$ |
| **Development** | AR 600-546, 1 min |
| **ICP-RIE** | Recipe from table 12, 30 s |
| **Resist Strip** | AR 600-71, 5 min in sonic bath |

On this run the spinner speed was set to 3000 rpm instead of 4000 rpm. This resulted in a more uniform layer, at least by visual inspection. From the figure 48 this should also result in a slightly thicker resist. The spinner recipe can be seen in table 17.

**Table 17:** CSAR62 spinner recipe, 2nd version.

| | |
|---|---|
| Spin speed | 3000 RPM |
| Acceleration | 500 |
| Time | 60s |

The input on both the straight waveguides and MZI has a taper. The width goes from $5\mu m$ at the input and down to $500nm$ over a distance of $30\mu m$, see figure 62. This makes the alignment process easier when attempting to couple light in the optics lab. The wide waveguide section is also made longer than necessary in case something went wrong in the scribe process.

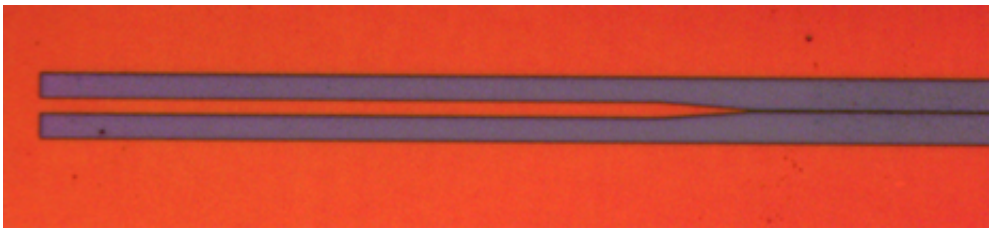

**Figure 62:** Optical microscope image of the tapered section after ICP-RIE. $SiO_2$ is seen as blue and a−Si is seen as red/orange.

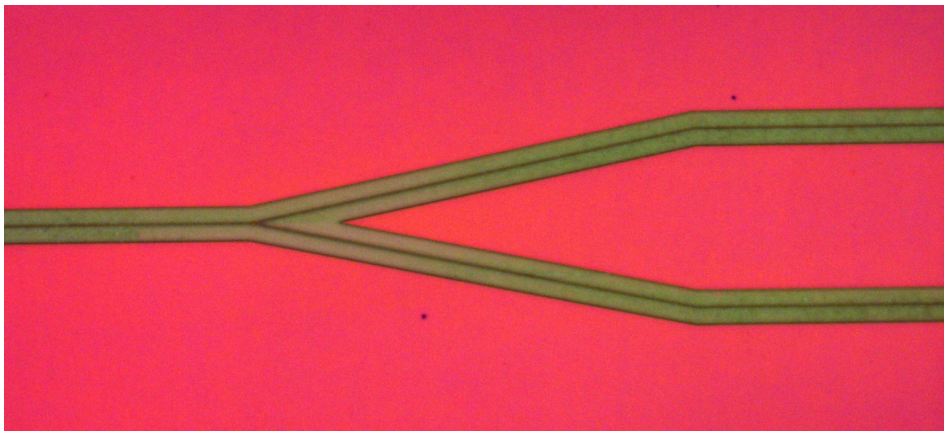

**Figure 63:** Optical microscope image of a MZI split after ICP-RIE. $SiO_2$ is seen as blue and the a−Si is seen as pink.

The sample was first cut in half to separate the straight waveguides and MZI's. After the samples were cut along the input and output waveguides they where placed in a sonic bath with the AR 600-71 stripper for five minutes. Both samples were then put in smaller sample holders and brought to the optics lab for testing.

In the optics lab carbon tape is used to adhere the sample to the holder. The holder is placed in the setup described in section 7, an illustration on how to secure samples can be seen in figure 64.

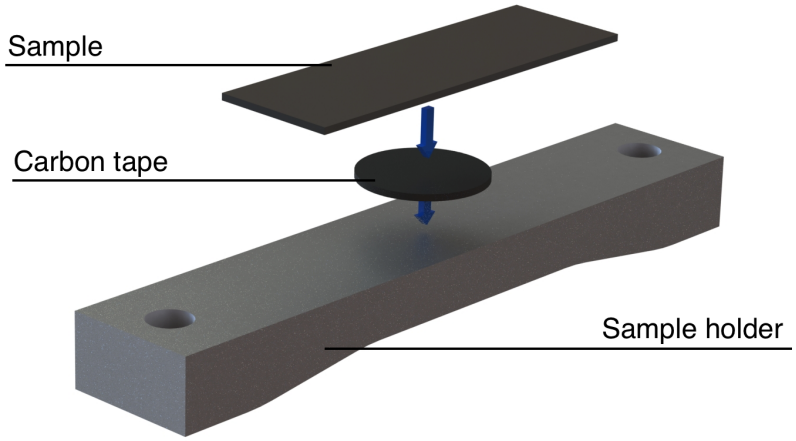


**Figure 64:** Illustration of securing sample to the sample holder.

First the straight waveguides were tested. After several failed attempts to couple light into 5 different waveguides, the sample was changed to one manufactured by Jens Høvik. This sample had been verified to work previously. After some alignment of the fiber ends, light was successfully coupled into one of the waveguides. This was confirmed by a pulsed signal on the oscilloscope along with visual inspection using the IR camera at the output. The MZIs was not tested, as the straight waveguides failed. The edges from the scribe process with waveguide ends were put in the cross sectional holder and analysed in the S(T)EM, see figure 65.

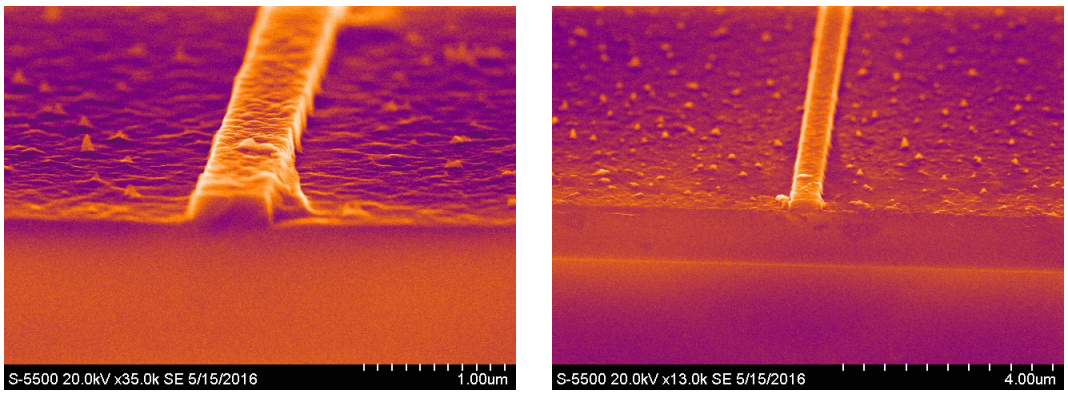


**(a)** **(b)**

**Figure 65:** False color SEM images of waveguide ends from sample B1, roughness of both Si and $SiO_2$ is clearly visible.

The reason the coupling failed can be due to the roughness of the both the Si layer and oxide. The etching process seems to have been too short, as seen from the peaks in the oxide layer and trapezoidal shape of the waveguides. The peaks could potentially be Si which was not etched, or it could be part of the underlying oxide layer.

In figure 66 a close up image of a MZI split can be seen. In these images the structure of the surface and sidewalls are clearer.

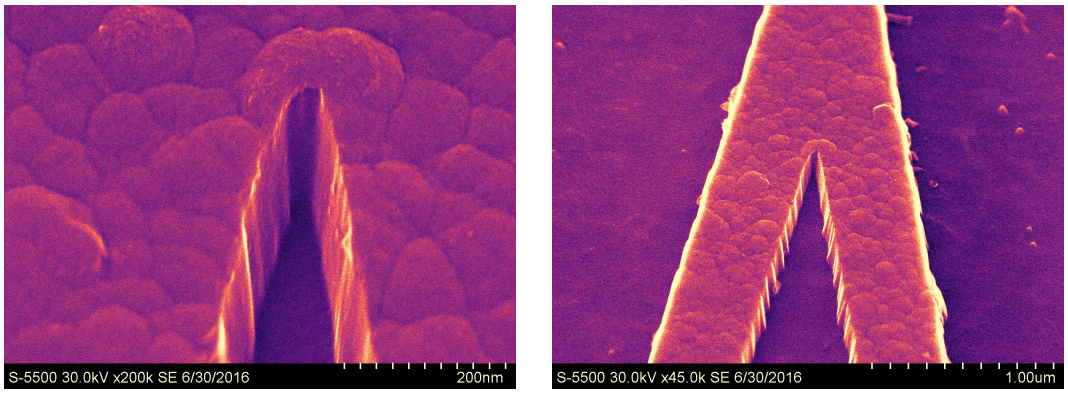


**(a)** **(b)**

**Figure 66:** False color SEM images of MZI Y-split on sample B1, roughness of both Si and $SiO_2$ is clearly visible.

The surfaces are clearly not planar. The roughness is irregular and seems random, and resembles the underlying oxide layer. On the closeup in 66 (a) the sidewall roughness is not to severe, but in (b) it seems that on a larger scale the sidewalls are uneven and not straight, but trapezoidal. There are several spots where chunks of what seems like excess Si are present, this could be both due to poor cleaning after the resist strip or the short etch. Note that the surface roughness on top of the waveguides would also be present on the bottom, this combined with the poor sidewalls would lead to tremendous losses. Even if one where able to couple light into the structure it would decay extremely fast and never propagate through the length of the guide. According to [40] the surface roughness should have a RMS value close to 1 nm to achieve losses in the order of a few decibels. In one example with a 400 nm x 200 nm strip waveguide with roughness around 5 nm, the losses are in the order of 60 dB/cm. So even though the roughness of the structures in figure 66 has not be measured exactly, based on the images, the losses here would be large and only seem like scattering from the fiber-tip at the input.

In figure 67 one overview image of the split, and a close up of the bend which goes from the split to the straight section of a MZI arm can be seen.

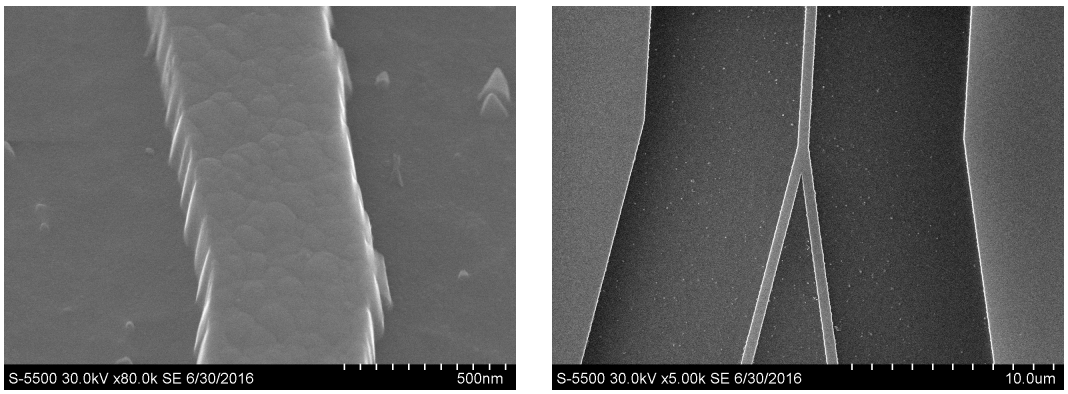


**(a)** **(b)**

**Figure 67:** False color SEM images of waveguide ends from sample B1, roughness of both Si and $SiO_2$ is clearly visible.

The etched features match the mask closely regarding shape from a visual inspection. Also the measurements made using the utilities in the S(T)EM software match besides some irregularities in the width of the waveguide. This gives a good indication that the EBL process gives good consistent results, and the main issue is the deposition and etching process. The cleaning steps on this sample was done more rigorously than on sample A1 to have the best possible surface preparation before the PECVD process. After examining this sample and a consultation with Jens Høvik, it was decided to increase the etch time to 35 s for the next samples.

## 8.3 Sample B2

Sample B2 consisted of 30 straight waveguides for testing in the optics lab. The PECVD grown SOI platform was used in this run as well, and an overview of the process flow can be seen in table 18.

**Table 18:** Process overview sample B2

| | |
|---|---|
| **PECVD $SiO_2$** | Recipe from table 9, 15 min |
| **PECVD Si** | Recipe from table 10, 35 s |
| **Spin on CSAR 62** | Recipe from table 17 |
| **EBL** | Exposure-dose: $300\mu C/cm^2$ |
| **Development** | AR 600-546, 1 min |
| **ICP-RIE** | Recipe from table 12, 35 s |
| **Resist Strip** | AR 600-71, 5 min in sonic bath |

The cleaning process done before the PECVD process was now also used after the oxide deposition in preparation for the a$-$Si deposition. The cleaning is performed by first placing the sample in a 5 min ultrasonic bath with Acetone following 5 min in IPA, a dehydration bake and then straight to the spinner bench for spinning on the resist.

This sample was also brought to the optics lab for testing after the resist strip and an optical inspection. Several attempts where made to couple light in to different waveguides, but with no success. The sample was then brought back to Nanolab where it was scribed and inspected using S(T)EM. In figure 68 an overview image of the straight waveguide can be seen along side an image of the cut.

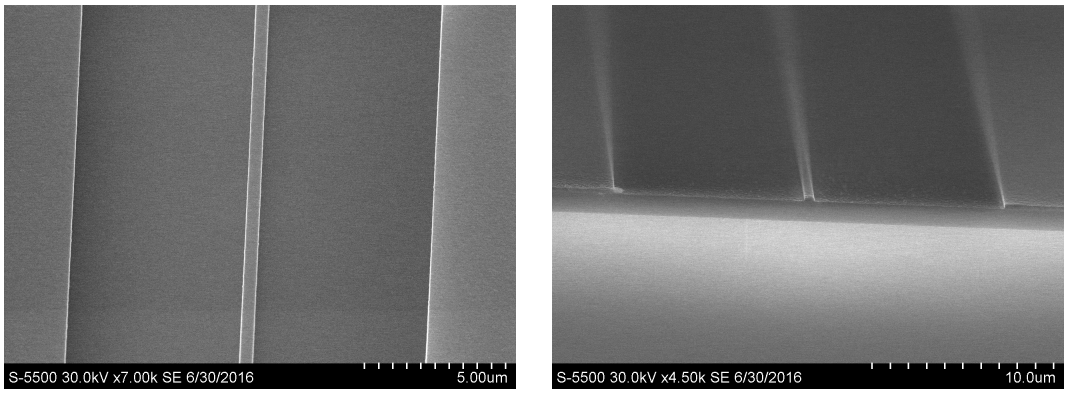


**(a)** **(b)**

**Figure 68:** SEM images of sample B2, (a) Overview image of the straight waveguide, (b) Image of the cut section.

The roughness of the oxide is clearly visible, but there seems to be less contamination on the surface in general. This indicates that the particles seen on the previous samples most likely are due to insufficient cleaning. Both in between processes and before inspection, thus it could have been avoided.

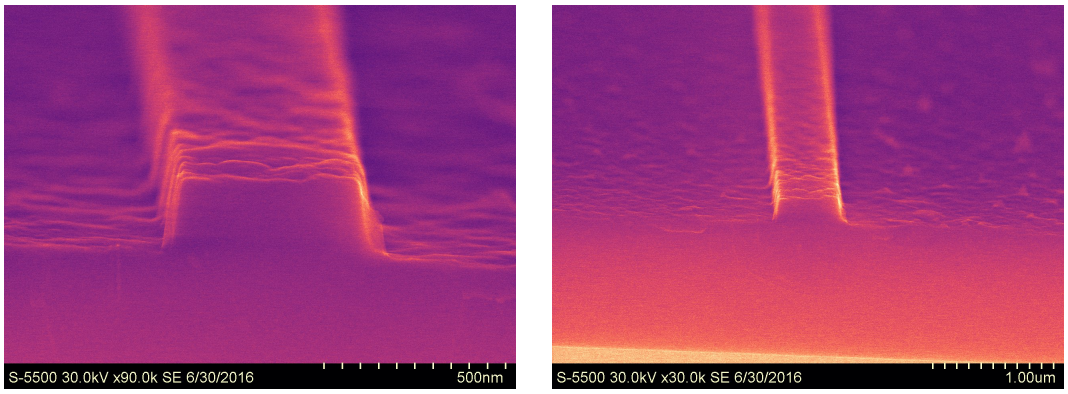


**(a)** **(b)**

**Figure 69:** False color SEM images of waveguide ends from sample B1, roughness of both Si and $SiO_2$ is clearly visible.

In figure 69 a close up of the waveguide can be seen. The longer etch time seems to have improved the profile a bit, but the sidewalls does not seem to be perfectly straight. Also the roughness of both sidewalls and surface is still severe.

It was decided that the next step is to run two samples in parallel, one with thermal oxide, and one with PECVD grown oxide. If light is successfully coupled into the samples with thermally grown oxide, and the samples with PECVD grown oxide fails. This would be a strong indication that the roughness of the PECVD oxide is to severe to function as the insulating layer in photonic structures on SOI.

## 8.4 Sample C3

The initial dose used in the EBL was $300\mu C/cm^2$, this was the dose Jens Høvik had used on several exposures. Lars G. Holmen works with photonic crystals and have much finer structures and details than a bulk 220 x 500 nm strip waveguide, and in some samples he saw signs of underexposure. After he did several tests with a wide selection of currents and doses, the dose was increased to $350\mu C/cm^2$ to avoid underexposure.

Two samples were now run in parallel and consist of one sample (C3), with PECVD grown oxide covered in this section. The other sample (D3) consists of a $1\mu m$ thermally grown oxide layer on Si and covered in detail in section 8.5. The process overview can be seen in table 19. The PECVD had been down for maintenance for 4 weeks, so a conditioning run was performed to get the best possible results. The conditioning run was for 3 min on a blank Si carrier using the recipe seen in table 10.

**Table 19:** Process overview sample C3

| | |
|---|---|
| **PECVD $SiO_2$** | Recipe from table 9, 15 min |
| **PECVD Si** | Recipe from table 10, 35 s |
| **Spin on CSAR 62** | Recipe from table 17 |
| **EBL** | Exposure-dose: $350\mu\mathrm{C/cm}^2$ |
| **Development** | AR 600-546, 1 min |
| **ICP-RIE** | Recipe from table 12, 35 s |
| **Resist Strip** | AR 600-71, 5 min in sonic bath |

After the exposure and development the sample was inspected in the optical microscope. It was clear something had gone wrong in the exposure sequence, most likely when converting from the GDSII file made in CleWin.

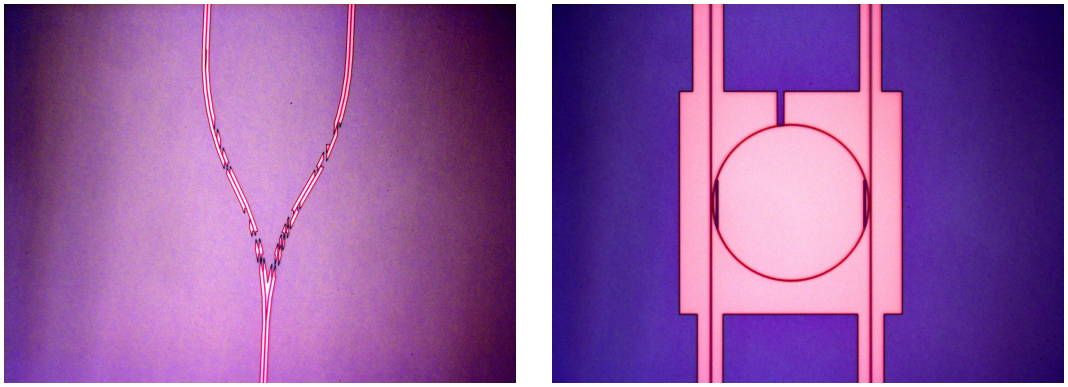

**(a)** **(b)**

**Figure 70:** Optical microscope image of developed resist showing errors in exposure sequence, most likely a software error when converting from CleWin to the Elionix software.

In figure 70 there are several places that are not exposed. The mask was converted and examined again in the EBL software, and the same pattern seen in figure 70 was found by using a function called Paint On/Off which highlights the exposure areas. The samples were then stripped off resist and cleaned. A new mask was made in CLeWin and all parameters was thoroughly checked before exposing. This mask omitted the MZI's as these seemed to be the structures most affected. After development, the exposed area still had repeating defects, see figure 71.

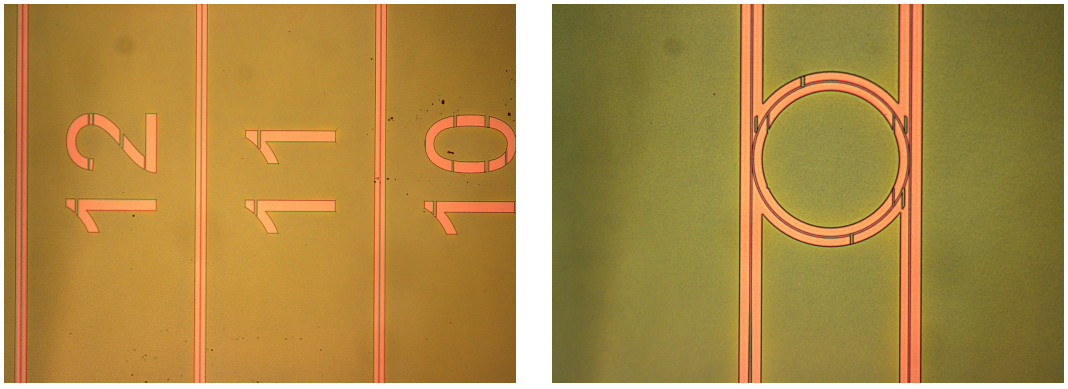


**(a)** **(b)**

**Figure 71:** Optical microscope image of developed resist showing errors in exposure sequence, most likely a software error when converting from CleWin to the Elionix software.

The part which was troubling was the defects on the numbers seen in fiure 71 (a). These numbers are made using a built in function in CleWin, and have been made on all previ-

ous samples, both by the author and other users. To fix the issue with the mask, it was loaded into a software called Beamer which is an additional software to improve EBL efficiency and give better control over the exposure in general. Using a heal-function solved the problem, and an additional sample in crystalline Si was run in parallel with C3 and D3. The crystalline sample is called A2, and the details on the sample is covered in section 8.6. The purpose of this crystalline sample was to examine it using S(T)EM, while C3 and D3 was prepared for testing in the optics lab. Unfortunately there was an issue with the scriber when the samples where to be cut. One of the rings holding the adhesive tape in place had cracked. The ring was eventually fixed by Tore Landsem at the tele engineering workshop at NTNU. When the sriber was functioning again, it was decided to only inspect the samples in S(T)EM. This would produce comparable results, and there was a possibility that both testing and characterization could not be done in time.

In figure 72 a false color SEM image of the left side corner of the ring structure and a close up of the waveguide structure can be seen.

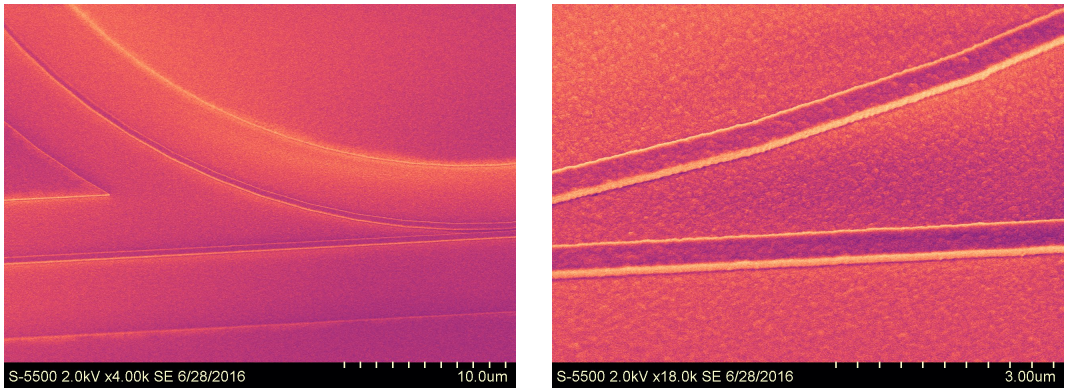


**(a)** **(b)**

**Figure 72:** False color SEM images of (a) Left side corner of a ring resonator, (b) Right side of the ring, close to the coupling region.

The roughness of the oxide surface is still visible, but the general shape of the structures are improved compared to the previous samples. There also seem to be less contamination and residual Si clumped up on waveguides and sidewalls.

The cross section of one of the waveguides and a close up tilted image of a waveguide can be seen in figure 73.

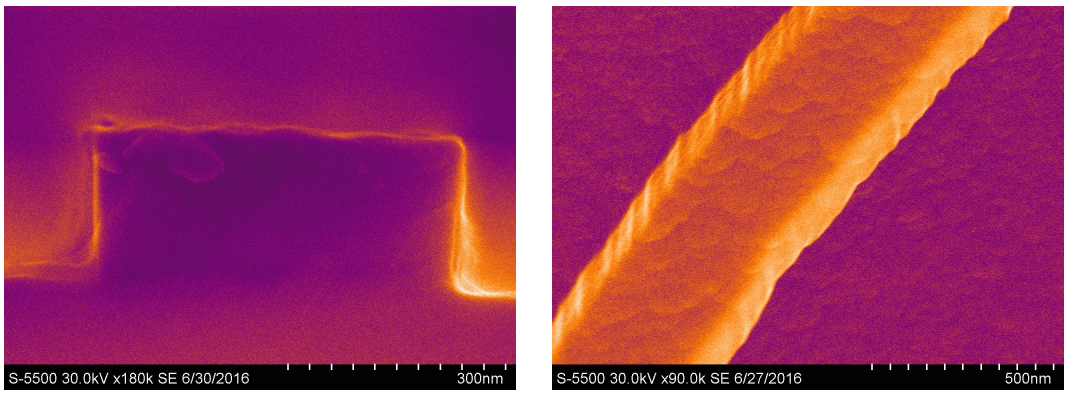


**(a)** **(b)**

**Figure 73:** False color SEM images of (a) Left side corner of the ring resonator, (b) Right side of the ring, close to the coupling region.

From these images the cross section profile has straighter sidewalls than what seen in the previous samples. The sidewall roughness also looks to be less severe by visual inspection. The increased etch time and extensive cleaning seems to have the desired effect. The underlying oxide layers effect on the deposited a−Si layer seems to be unavoidable. Improving this surface by the means of e.g chemical mechanical planarization (CMP) is undesirable, it would require the use of unique chemicals, properly designed pad and processing steps [3, 41]. This is where the thermally grown oxide comes in.

## 8.5 Sample D3

Sample D3 with a $1\mu m$ thick thermal oxide layer was run in parallel with the previous sample, and the process parameters are the same as shown in table 19, only the $SiO_2$ deposition is not applicable. In figure 74 both the ring structure on sample C3 and D3 can be seen for a comparison.

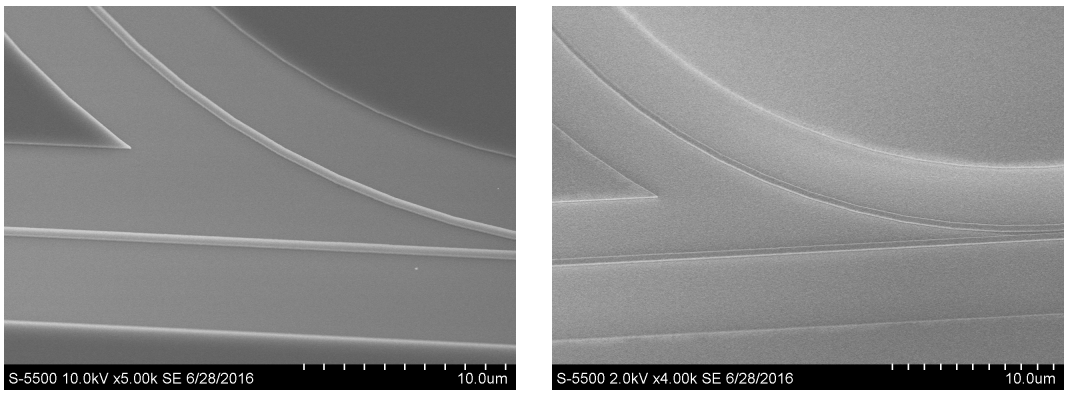


**(a)** **(b)**

**Figure 74:** SEM images of (a) Ring resonator fabricated using thermally grown oxide (b) Ring resonator fabricated using PECVD deposited oxide.

It is used different acceleration voltages to produce the two images, each setting producing the best possible image of the two different samples. In these images the difference in surface roughness is clear, but besides that, both structures match the mask dimensions. On a closer inspection there is a significant difference, in figure 75 the cross section of the two samples (C3, D3) can be seen.

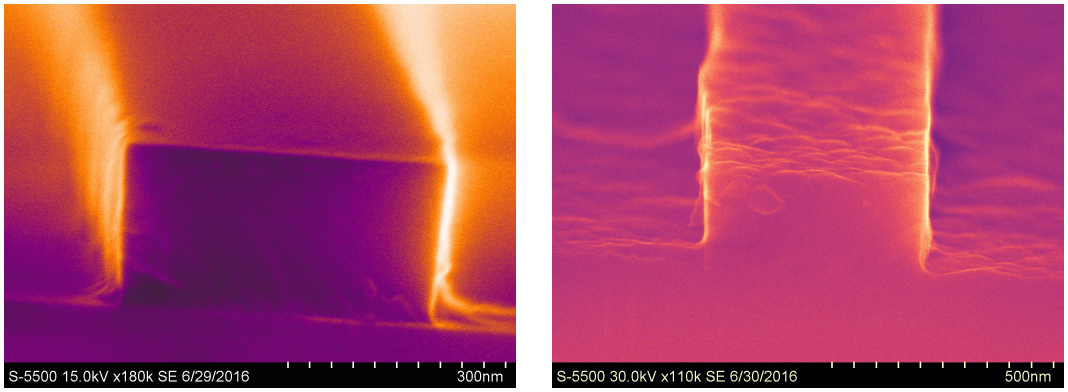


**(a)** **(b)**

**Figure 75:** False color cross section SEM images of (a) Waveguide fabricated using thermally grown oxide (b) Waveguide fabricated using PECVD deposited oxide.

The image in (b) was the best image possible due to the breaking process severely degraded some of the waveguide edges. Still there is a clear difference between the two waveguides. The one grown on thermal oxide, (a), has straight sidewalls, a planar surface both on the underlying oxide and the top of the waveguide. The waveguide in (b) is rough and uneven, it also suggests the etch recipe produces an even sidewall. This was harder to determine by examining the samples with PECVD oxide, as there are other factors that degrade the overall shape. The waveguide thickness was measured to be approximately 226 nm high and 479 nm wide.

The recurring issue of excess material along the sides is still not resolved, see figure 76.

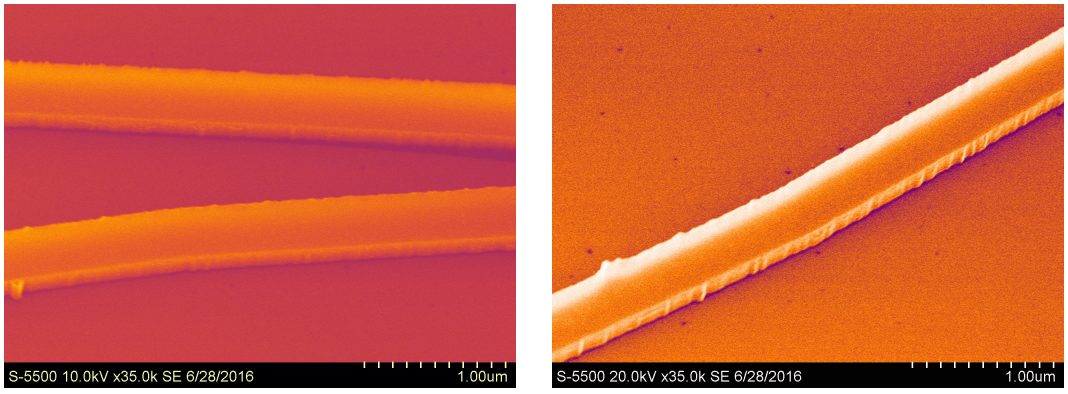


**(a)** **(b)**

**Figure 76:** False color SEM images of waveguides fabricated using thermally grown oxide (a) Waveguides close to the coupling region in a ring resonator (b) Waveguide that is part of the ring

In both images there are areas where small bulges of material are sticking out. If the material is Si or undeveloped resist is not clear from these images. After discussing the result with Jens Høvik, it was concluded the material was most likely excess resist left over from the developing stage. A possible solution is to either extend the developing time, or use a mild sonic bath during development. The developer is relatively mild to unexposed resist, so it should not degrade the rest of the pattern.

## 8.6 Sample A2

Sample A2 is a crystalline Si sample without additional deposited material. The sample is processed to compare with the SOI samples, and how the structures in crystalline Si are affected by the different process steps. An overview of the process can be seen in table 20. This was processed simultaneously as C3 and D3, so the changes decided on in the development phase was not determined yet.

**Table 20:** Process overview sample A2

| | |
|---|---|
| **Spin on CSAR 62** | Recipe from table 17 |
| **EBL** | Exposure-dose: $350\mu\mathrm{C}/\mathrm{cm}^2$ |
| **Development** | AR 600-546, 1 min |
| **ICP-RIE** | Recipe from table 12, 35 s |
| **Resist Strip** | AR 600-71, 5 min in sonic bath |

The CSAR 62 was spun on the sample after cleaning, and developed after exposure as the previous samples. When the sample was brought out of the beaker with developer, some of the resist was clearly not adhering to the Si layer, and most of the structures where unusable. After consulting with fellow student Lars G. Holmen which had encountered a similar problem, without finding a solution, the sample was still put through the etch. Some of the structures where intact and could be examined further using S(T)EM. There is an adhesive coating that can be applied before the resist, but this is not available in Nanolab. After the etch, the sample was cut in the scriber, before both ring resonators and a cross section of the waveguides where examined. The same mask that was used on sample C3, D3 was used here, where beamer solved the mask issues seen in figure 70 and 71.

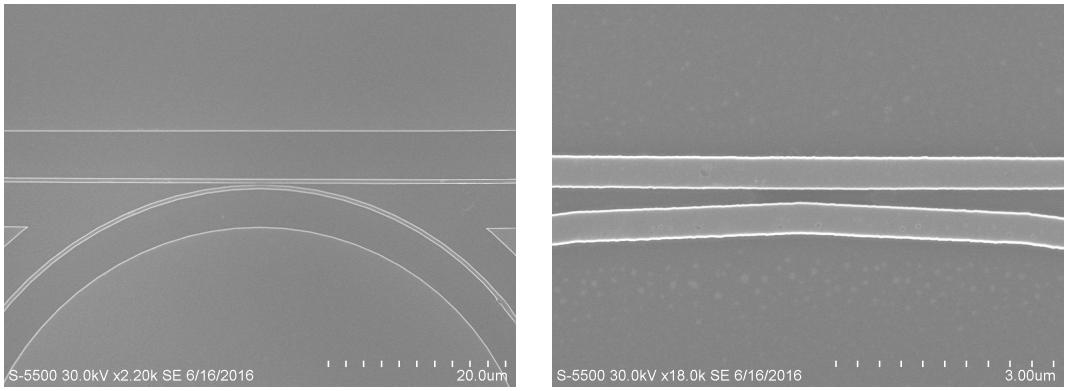


**(a)** **(b)**

**Figure 77:** SEM images of a ring resonator fabricated in crystalline Si. (a) Overview of the input and output waveguide (b) Close up of the coupling region.

The ring structures match the mask dimensions, and there is no apparent differences from sample C3 and D3, at least by a visual inspection. As mentioned in the EBL chapter, there are some issues when drawing circular shapes in CleWin. In figure 77 (b) the ring shape is not perfectly circular, but consists of clearly distinguishable polygons. This was also seen in sample C3 and D3. According to Mark Chiappa (senior engineer responsible for the new EBL system), this was easily fixed in Beamer. So it should not pose a problem in any future work with ring resonators on this system.

In figure 78 a cross sectional image of one of the waveguides can be seen.

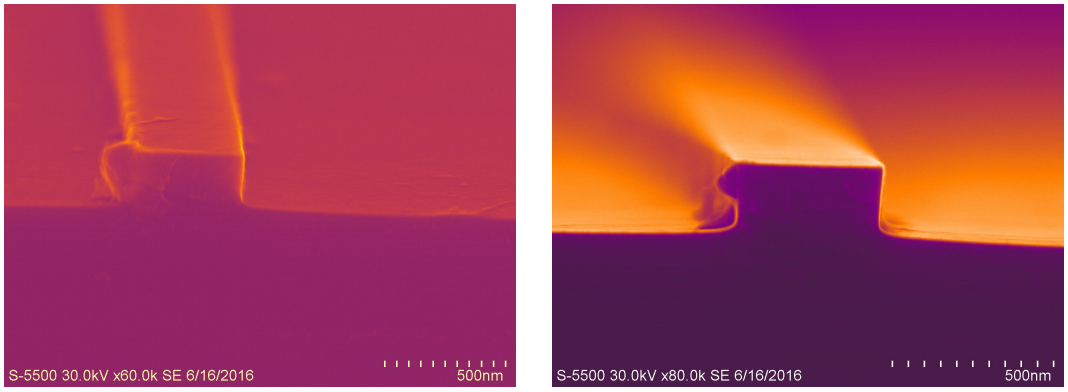


**Figure 78:** False color cross section SEM images of a waveguide fabricated on crystalline Si.

The particles seen on the left edge in the images are most likely Si dust caught in the breaking process. Apart from that, the shape of the waveguide is very similar to the inspected waveguide on sample C3. The material beads where not observed on this sample, but the as the developer step almost ruined all the structures the conclusion made in the previous section still stands. Sample A2, C3 and D3 where the last to be processed and characterized.

# 9 Discussion

When considering the resulting spectrum from the COMSOL simulations of the complete model, the intensity of the peaks close to the center peak only differs by 1-3 percent. This could pose a problem when trying to accurately determine the wavelength shift. If one of the peaks next to center was determined to be the highest peak, this would add additional 3 nm to the wavelength shift. As a result the wrong concentration of methane would be determined. The period of the signal could potentially be shortened to make it easier to separate the center peak wavelength, but if this would result in the desired effect has not been investigated. From equation 52 a shorter period would also require a larger $\Delta$FSR, thus decreasing the LOD. It seems there is a give and take when considering all factors. There is also discussed possibilities for improving the read-out by using signal processing algorithms on the output signal [18].

It is clear that the small intrinsic difference in refractive index between the SiO2 cladding and the PDMS polymer imposes a restriction on the length of the MZI, estimated to be around 17 cm. When considering that the losses in high quality Si waveguides are around 1 dB/cm [33, 42], the losses will be tremendous. Either a different polymer that can act as a host to Cryptophane should be considered, or using an alternate cladding material could be a second option. SAN has shown to be a suitable host for cryptophane, SAN has a refractive index of around 1.56 [27]. This would give a slightly larger contrast compared to PDMS which is close to 1.42 [28]. There are also current research that work towards developing new low refractive index materials. These could potentially be used instead of the $SiO_2$ layer which is set as cladding material in this thesis. One of the methods to produce such materials is discussed in literature, and suggests arrays of $SiO_2$ nanorods to achieve a low refractive index. In this paper indexes close to 1 have been reported [43, 44].

The waveguide design could also be optimized for higher sensitivity [16]. This off course needs to be balanced with losses. The main reason the 500 nm x 220 nm strip waveguide was chosen is relatively easy fabrication compared to e.g. rib waveguides. Previous work has also been done using this design, which made comparing results with literature easier.

The main source of loss in the waveguides are due to sidewall roughness [40], and should be reduced as much as possible. As the arms in the MZI are relatively long there will be some loss, and a maximum acceptable loss should be included as a design parameter in the future. The roughness of the PECVD deposited $SiO_2$ layer seems to be too severe to function as the insulating layer. All the samples tested in the optics lab using the PECVD oxide failed, but this could partly be due non optimized processing. The final samples run in parallel were not tested, but based on inspection in S(T)EM there is a qualitatively difference in the structures.

As light was successfully coupled into waveguides fabricated by Jens Høvik on thermal oxide, this would be the best choice for an SOI platform, which to fabricate a prototype sensor on. As for the methane sensitive layer, both the use of polymers and synthesis of Cryptophane-A has been shown to be reproducible by the work of several separate sources [24, 25, 27, 26].

Out of all the samples, D3 gave the most promising results. The fabricated features matched the mask drawn in CleWin, and the top Si layer was measured to be 226 nm thick. The only issue with the EBL process was the shape of the ring, but as mentioned this should not be problematic if the right software is used. The 100 nm separation between ring and waveguide could not be measured exactly due to mentioned problem with the ring shape. From the closest point on the ring to the waveguide it was approximately 130 nm. The etch step seemed to produce straight sidewalls and low degree of roughness on the final samples. These parameters along with losses should be more accurately quantified in the future. The development step after exposure also needs to be refined to produce consistent results. The beads of material on the waveguides was concluded to most likely be undeveloped resist. This could have been picked up earlier by using the EDX functionality of the S(T)EM.

# 10 Conclusion

In this thesis the theory describing a vernier enhanced Mach Zehnder interferometer has been discussed. A method for effectively simulating optical components with features ranging from centimeter to nanometer scale using COMSOL has been demonstrated. By using this method, the shift in resonance for a vernier enhanced sensor has been shown to match theory. In table 8 a methane sensitive sensor using the concept is presented. The sensor has a limit of detection as low as $9.34 \cdot 10^{-6}$ RIU and overall sensitivity of $326$ $\mu m$/RIU. From [28] a 50 nM concentration of $CH_4$ results in a refractive index change of $1.6 \cdot 10^{-4}$ in the PDMS cladding. The theoretically shift in resonance of this sensor is 32.66 nm due to a change in cladding index of $10^{-4}$. The proposed sensor should detect concentrations of dissolved methane less than 50 nM .

The feasibility of producing a prototype in NTNU Nanolab has also been investigated. Both straight waveguides, ring resonators and five MZI's with Y-bends have been fabricated on an silicon-on-insulator (SOI) platform. The processes used includes plasma enhanced chemical vapor deposition (PECVD), electron beam lithography (EBL), inductively coupled plasma reactive ion etch (ICP-RIE) and a scanning tunneling electron microscope (S(T)EM) for characterization. The SOI platform is realized both by using PECVD deposited $SiO_2$, and a thermally grown oxide layer. The roughness of the PECVD deposited $SiO_2$ layer seems to be too severe to function as the insulating layer. Also the samples tested in the optics lab using the PECVD oxide all failed. This could partly be due to non-optimized processing. The final and most promising samples were not tested, but based on inspection in S(T)EM there is a qualitative difference in the waveguide structures. The SOI platform using thermally grown oxide is concluded to be the favourable choice for fabricating a prototype sensor in the future. Light was successfully coupled into waveguides fabricated by Jens Høvik using this thermal oxide as a base. The same fabrication equipment had been used on this sample, which further substantiates the possibility for a prototype fabricated in NTNU Nanolab.

# 11 Future Work

- Researching substitute host polymers for cryptophane-A and low refractive index materials for the cladding.
- Optimizing the sensor design and investigate the sensitivity of different waveguide designs.
- Further optimize processing parameters for producing consistent optical components in Nanolab.
- Fabricate ring resonators and Mach Zehnder interferometers for characterisation in the optics lab.

# References

[1] https://www.comsol.no/multiphysics/finite-element-method. *The Finite Element Method (FEM).*

[2] FILMETRICS. *Taking the mystery out of thin-film measurement*. FILMETRICS, INC, 2016.

[3] Michael Quirk, Julian Sedra. *Semiconductor Manufacturing Technology*. Pearson, 2001.

[4] Michael Shearn, Xiankai Sun, M. David Henry, Ammon Yariv, and Axel Scherer. *Semiconductor Technologies*. Intech, 2010.

[5] http://ammrf.org.au/. *SEM interaction volume illustration*.

[6] Xiao, Gaozhi, Bock, Wojtek J., Xiao, Gaozhi. *Photonic Sensing, Principles and Applications for Safety and Security Monitoring*. Wiley, 2012.

[7] Bahaa E. A. Saleh, Malvin Carl Teich. *Fundamentals of Photonics, 2nd Edition*. Wiley, 2007.

[8] Robert G. Hunsperger. *Integrated Optics, Theory and Technology*. Springer, 2009.

[9] Graham T. Reed, Andrew P. Knights. *Silicon Photonics: An Introduction*. Wiley, 2004.

[10] William S. Reeburgh. *Oceanic Methane Biogeochemistry*. Chem. Rev., 2007.

[11] David K. Cheng. *Field and Wave Electromagnetics, 2nd Edition*. Pearson, 2014.

[12] Ginés Lifante. *Integrated Photonics Fundamentals*. Wiley, 2003.

[13] David Voss. *Silicon Lasers, Faster chips require built-in optics.* MIT technology review, 2001.

[14] D. G. Rabus. *Integrated Ring Resonators, The Compendium*. Springer, 2007.

[15] Mario La Notte, Vittorio M.N. Passaro. *Ultra High Sensitivity Chemical Photonic Sensing by Mach-Zehnder Interferometer Enhanced Vernier-Effect*. Sensors and Actuators B: Chemical, 2010.

[16] Mario La Notte, Benedetto Troia, Tommaso Muciaccia, Carlo Edoardo Campanella, Francesco De Leonardis and Vittorio M. N. Passaro. *Recent Advances in Gas and Chemical Detection by Vernier Effect-Based Photonic Sensors*. Open access, 2014.

[17] Stefania Dante, Daphne Duval, Borja Sepulveda, Ana Belen Gonzalez-Guerrero, Jose Ramon Sendra, and Laura M. Lechuga. *All-optical phase modulation for integrated interferometric biosensors*. Optical Society of America, 2012.

[18] Tom Claes, Wim Bogaerts, and Peter Bienstman. *Experimental characterization of a silicon photonic biosensor consisting of two cascaded ring resonators based on the Vernier-effect and introduction of a curve fitting method for an improved detection limit*. Optical Society of America, 2010.

[19] Neil Bourne. *Materials in Mechanical Extremes*. Cambridge University Press, 2013.

[20] André Colas. *Silicones: Preparation, Properties and Performance*. Dow Corning, 2005.

[21] https://en.wikipedia.org/wiki/Polydimethylsiloxane. *PDMS structure*.

[22] J. C. Lotters, W. Olthuis,P. H. Veltink and P. Bergveld. *The mechanical properties of the rubber elastic polymer polydimethylsiloxane for sensor applications*. Journal of Micromechanics and Microengineering, 1997.

[23] Srinath Satyanarayana, Rohit N. Karnik, and Arunava Majumdar. *Stamp-and-Stick Room-Temperature Bonding Technique for Microdevices*. Journal of Microelectromechanical Systems, 2005.

[24] Kathleen E. Chaffee, Heather A. Fogarty, Thierry Brotin, Boyd M. Goodson, and Jean-Pierre Dutasta. *Encapsulation of Small Gas Molecules by Cryptophane-111 in Organic Solution. 1. Size- and Shape-Selective Complexation of Simple Hydrocarbons*. J. Phys. Chem. A, 2009.

[25] M. Benounis, N. Jaffrezic-Renault, J.-P. Dutasta, K. Cherif, A. Abdelghani. *Study of a new evanescent wave optical fibre sensor for methane detection based on cryptophane molecules*. Elsevier B.V, 2005.

[26] Olena Taratula, P. Aru Hill, Yubin Bai, Najat S. Khan, and Ivan J. Dmochowski. *Shorter Synthesis of Trifunctionalized Cryptophane-A Derivatives*. Organic Letters, 2011.

[27] Firehun Tsige Dullo, Susan Lindecrantz, Jana Jágerská, Jørn H. Hansen, Magnus Engqvist, Stian Andre Solbø, and Olav Gaute Hellesø. *Sensitive on-chip methane detection with a cryptophane-A cladded Mach-Zehnder interferometer*. Optics Express, 2015.

[28] Cédric Boulart, Matthew C. Mowlem, Douglas P . Connelly, Jean-Pierre Dutasta, Christopher R. German. *A novel, low-cost, high performance dissolved methane sensor for aqueous environments*. Optical Society of America, 2008.

[29] C. Boulart, D.P. Connelly, M.C. Mowlem. *Sensors and technologies for in situ dissolved methane measurements and their evaluation using Technology Readiness Levels*. Elsevier B.V., 2009.

[30] COMSOL. *Wave Optics Module, User Guide*. 2013.

[31] https://www.comsol.no/blogs/. *Using Perfectly Matched Layers and Scattering Boundary Conditions for Wave Electromagnetics Problems*.

[32] B. Troia, V. M. N. Passato, F. De Leonardis. *Design of Efficient Photonic Sensors Based on Vernier Effect in near-IR, Conference Paper*. 2012.

[33] Jaime Cardenas, Carl B. Poitras, Jacob T. Robinson, Kyle Preston, Long Chen, and Michal Lipson. *Low loss etchless silicon photonic waveguides*. Optical Society of America, 2009.

[34] Wilfried G.J.H.M. van Sark. *Methods of Deposition of Hydrogenated Amorphous Silicon for Device Applications*. Debye Institute, Utrecht University, 2002.

[35] J.C. Knights, G. Lucovsky and R.J. Nemanich. *Defects in Plasma-Deposited a-Si : H*. North-Holland Publishing, 1978.

[36] Daniel L. Flamm. *Mechanisms of silicon etching in fluorine- and chlorine- containing plasmas*. Pure and Applied Chemistry, 1990.

[37] Evangelos Gogolides, A. Tserepi, Androula Galiouna Nassiopoulou. *Highly anisotropic silicon reactive ion etching for nano fabrication using mixtures of SF6/CHF3 gases*. Journal of vacuum science and technology, 1997.

[38] Bettina Voutou, Eleni-Chrysanthi Stefanaki. *Electron Microscopy: The Basics*. 2008.

[39] O. Kononchuk, B.-Y. Nguyen. *Silicon-On-Insulator (SOI) Technology: Manufacture and Applications*. Elsevier, 2014.

[40] D. J. Lockwood. *Silicon Photonics, Components and Integration*. Springer, 2011.

[41] "Gautam Banerjee and Robert L. Rhoades". *"Chemical Mechanical Planarization, Historical Review and Future Direction"*. The Electrochemical Society, 2008.

[42] Shiyang Zhu, G. Q. Lo, and D. L. Kwong. *Low-loss amorphous silicon wire waveguide for integrated photonics: effect of fabrication process and the thermal stability*. Optical Society of America, 2010.

[43] J.-Q. Xi, Martin F. Schubert, Jong Kyu Kim, E. Fred Schubert, Minfeng Chen, Shawn-Yu Lin, W. Liu and J. A. Smart. *Optical thin-film materials with low refractive index for broadband elimination of Fresnel reflection*. Nature Publishing Group, 2007.

[44] J.-Q. Xi, Jong Kyu Kim, and E. F. Schubert. *Low-Refractive-Index Films: A New Class of Optical Materials*. IEEE Newsletter, 2005.

[45] James E. Brady. *Generell kjemi*. Wiley, 2004.

[46] Hannah M. Roberts, Alan M. Shiller. *Determination of dissolved methane in natural waters using headspace analysis with cavity ring-down spectroscopy*. Elsevier B.V., 2014.

[47] J Hannigan, F Greig, S S Freeborn and H A MacKenzie. *A pulsed photoacoustic system for the spectroscopy and monitoring of hydrocarbon liquids using stimulated Raman scattering in a silica fibre as a near-infrared source*. IOPscience, 1998.

[48] K. Misiakos, I. Raptis, A. Salapatas, E. Makarona, A. Botsialas, M. Hoekman, R. Stoffer, and G. Jobst. *Broad-band Mach-Zehnder interferometers as high performance refractive index sensors: Theory and monolithic implementation*. Optical Society of America, 2014.

[49] A. Messica, A. Greenstein, and A. Katzir. *Theory of fiber-optic evanescent-wave spectroscopy and sensors*. Optical Society of America, 1996.

[50] L. van der Sneppen, F. Ariese, C. Gooijer and W. Ubachs. *Liquid-Phase and Evanescent-Wave Cavity Ring-Down Spectroscopy in Analytical Chemistry*. Annual Review of Analytical Chemistry, 2009.

[51] F. Udrea, S.Z. Ali, M. Brezeanu, V. Dumitru, O. Buiu, I. Poenaru1, M.F. Chowdhury, A. De Luca and J.W. Gardner. *SOI Sensing Technologies for Harsh Enviroment*. IEEE, 2012.

[52] http://www.comsol.com/models. *COMSOL models, by COMSOL Inc.*

[53] Muhammad Rizwan Amirzada, Andreas Tatzen, Volker Viereck, Hartmut Hillmer. *Surface roughness analysis of SiO2 for PECVD, PVD and IBD on different substrates*. Springer, 2014.